DEVELOPING PROXIES TO RECONSTRUCT THE INTENSITY AND MAGNITUDE OF PREHISTORIC TROPICAL CYCLONES AND EARTHQUAKES

By

ISABEL J HONG

A dissertation submitted to the

School of Graduate Studies

Rutgers, The State University of New Jersey

In partial fulfillment of the requirements

For the degree of

Doctor of Philosophy

Graduate Program in Oceanography

Written under the direction of

Benjamin P Horton

And approved by

_____

_____

_____

_____

New Brunswick, New Jersey

October, 2019

ABSTRACT OF THE DISSERTATION

Developing proxies to reconstruct the intensity and magnitude of prehistoric tropical cyclones and earthquakes

By ISABEL J HONG

Dissertation Director:

Benjamin P Horton

Coastal risk assessments using observational records and instrumental measurements are insufficient in identifying the potential magnitude and recurrence of tropical cyclones (TC), earthquakes, and tsunamis. Coastal sediments from low-energy depositional environments preserve evidence of prehistoric events as changes in litho- and biostratigraphy.

Chapter 1 investigated the sediments deposited by TC Pam at two sites (Manuro and Port Resolution Bay) to provide a modern analogue for reconstructing the long-term variability in tropical cyclone frequency and intensity. TC Pam was a Category 5 intensity tropical cyclone with 10-minute sustained wind speeds as high as 270 km/h that made landfall on Vanuatu. Manuro is a mixed-carbonate embayment with a measured TC Pam flow depth of 4.2 m above mean sea level (MSL) and a minimum inland extent of 400 m. The overwash sediment from TC Pam at Manuro is a coarse- to medium-grained sand that displays a coarsening upward sequence. Port Resolution Bay, a volcaniclastic beach had a measured TC Pam flow depth of 3.3 m above MSL and an inundation distance of 320 m. The overwash sediment at Port Resolution Bay is a coarse- to medium-grained sand that displayed a fining upward sequence in Trench

PRB2. The application of laboratory derived settling velocities from the TC Pam overwash sediments were promising. I applied a sediment transport model to reconstruct a field-measured estimate of flow depth at Port Resolution Bay within 11% of the measured value. But future applications of the sediment transport model in mixed-sediment environments will continue to require site-specific calibrations of settling velocities.

Chapter 2 examined how the distribution of modern diatoms across tidal wetlands can be used to reconstruct RSL rise caused by Cascadia subduction zone earthquakes of the coast of Washington state. I described and quantified inter- and intra-site variability in diatom distributions and related environmental variables (elevation, grain-size, total organic carbon, porewater salinity, and nutrients) across four shore-perpendicular transects from three tidal marshes of Willapa Bay, Washington. The modern training set from the three marshes consisted of 367 diatoms species across 94 genera that captured the range of diatoms found in marine, brackish, and freshwater environments. Multivariate statistical techniques identified floral zones at each tidal marsh with differing controls by the environmental variables. Two transects (Bone River Transect 1 and the Niawiakum River Transect) showed vertical zonation of diatoms with elevation as the major environmental control (35% and 28% of variance explained, respectively). Vertical zonation was absent at the Naselle River Transect with salinity identified as the major environmental control (21% of variance explained). The combined regional training set and an intra-site comparison of two transects at Bone River also did not display vertical zonation despite overlapping elevations. In the absence of a well-defined relationship with elevation at all marshes due to the localized

nature of assemblages, my results suggest that alternative methods must be sought to address limitations in diatom-based RSL reconstructions.

Chapter 3 compared the reconstruction of coastal subsidence along the Cascadia subduction zone using an established and new Bayesian diatom-based transfer function. The application of an established transfer function approach (weighted-averaging partial least squares) to six, intertidal subsidence stratigraphic sequences (mud-over-peat contacts) of coseismic subsidence at the Redtail locality in Willapa Bay produced a poor modern analogue for all 77 fossil samples. Using a novel dimension reduction approach, I grouped diatoms based on similarities in abundance and distribution with elevation. A hierarchical clustering method created 12 species groups, which increased the good analogues from 0 to 21%. The groups displayed broad, unimodal, and bimodal response distributions of occurrence across elevation with three groups displaying a high probability of occurrence within a narrow elevation range, which suggested that the grouped approach is more suitable for reconstructing coseismic subsidence. My new Bayesian diatom transfer function integrated the grouped species and stratigraphic prior information (i.e., sediment lithology) to produce reliable subsidence estimates of 0.46 m ± 0.33 m (1700 CE earthquake) and 0.51 m ± 0.34 m (1130 to 1350 yrs CE earthquake) for the two uppermost mud-over-peat contacts. No matching analogues were found for four earlier mud-over-peat contacts, which suggests the modern intertidal environment from the training set does not capture the range of paleoenvironmental conditions that existed in Willapa Bay from ~1400 to 3500 yrs CE.

Acknowledgements

I would like to thank my committee for their guidance and support. Ben, thank you for the opportunity to challenge myself and grow as a scientist as I traveled the world in search of new proxies. Alan, thank you for your guidance and mentorship as we navigated the marshes of Chile and Cascadia together. Vadim, thank you for your support and geophysical perspective throughout this process. Kay, thank you for your thoughtful encouragement in the pursuit of knowledge.

Chapter 1: Thank you to landowners on Efate and Tanna islands for granting access to their property. Thank you to collaborators in fieldwork and research: Jessica Pilarczyk, Hermann M. Fritz,, Thomas Kosciuch, Davin J. Wallace, Clayton Dike, Allan Rarai, Marris J. Harrison, and Fred R. Jockley.

Chapter 2: Thank you to collaborators in fieldwork and research: J. Scott Padgett, Robert O'Donnell, Andrea Hawkes, Simon Engelhart, Alan Nelson, Robert C. Witter, Tina Dura, Rachel Stearns, and SeanPaul LaSelle. Thank you to Nina Desianti and Marina Potapova for their willingness to chat diatoms and provide encouragement.

Chapter 3: Thank you to Niamh Cahill. Without you, this chapter would not exist. Thank you collaborators in fieldwork and research: J. Scott Padgett, Robert O'Donnell, Andrea Hawkes, Simon Engelhart, Alan Nelson, Robert C. Witter, and Tina Dura. A very special thank you to Tiffany Otai for her assistance in the lab.

Thank you to the Rutgers community who provided endless support and words of encouragement. A special thank you to my fellow graduate students who were always willing to lend an ear and commiserate over good food and drinks.

This research has been funding by an NSF EAR-1545619 grant, NSF EAR-1402017 grant, and DMCS Graduate Assistantships. Additional funding for research, travel and scholarship expenditures were provided by Rutgers University, EOAS, SSA, IGCP, and IDS. Chapter 1 exists as a current publication in the journal *Marine Geology* (Hong et al., 2016).

To my family, thank you for your continual love and support as I moved to different counties, states, and countries to pursue my passions.

Table of Contents

List of Tables

Chapter 1

Chapter 2

List of Figures

Chapter 1

Chapter 2

Introduction

Coastal communities are at risk of flooding from relative sea-level (RSL) rise from tropical cyclones, earthquakes, and tsunamis. For example, the 2011 Tohoku-oki earthquake (M_w 9.0) generated a tsunami that inundated over 400 km^2 of land with a maximum inundation height of 19.5 m in Japan (Mori et al., 2011). Similarly, the 2013 Category 5 Typhoon Haiyan caused maximum storm surge heights of 5 to 7 m and 1-minute sustained wind speeds of 241 km/hr, which destroyed over 1.1 million homes in the Philippines (JTWC, 2014; Mori et al., 2014; Soria et al., 2016). Although instrumental measurements and observational accounts are too short to identify the potential magnitude and recurrence of tropical cyclones, earthquakes, and tsunamis, coastal sediments can archive geologic evidence of these events on centennial and millennial scales.

Coastal sediments commonly preserve evidence of coastal flooding as changes in litho- and biostratigraphy (Hemphill-Haley, 1995a; Nelson et al., 1996; Yeats et al., 1997). For example, RSL change caused by subduction zone earthquakes can be preserved in sediments as a sequence of organic-rich soil abruptly overlain by tidal mud (Nelson et al., 1996; Sawai et al., 2009; Dura et al., 2014). Moreover, sediments deposited by tropical cyclones and tsunamis may be recognized as layers of coarse sediments preserved in low-energy coastal environments such as coastal lakes, wetlands, and ponds (Atwater, 1987; Liu and Fearn, 1993; Donnelly et al., 2004). Many of the best reconstructions of tropical cyclones intensity and earthquake magnitude are derived from changes in microfossil (diatoms, foraminifera, and pollen) assemblages, because they provide a more precise estimate of environmental change (Zong et al., 2003; Sawai et al., 2004; Pilarczyk et al., 2016). Microfossils, in combination with statistical techniques, can provide a quantitative estimate of RSL change that can be used to

reconstruct tropical cyclone intensity or earthquake magnitude (e.g., Wang et al., 2013; Pilarczyk et al., 2016; Horton et al., 2017).

In this dissertation, I explored how the geologic record can be utilized to address unknowns in hazards research by establishing proxies to reconstruct prehistoric records of tropical cyclones, earthquakes, and tsunamis. To better understand the long-term variability of these events, we rely on present day processes to act as a modern analogue to guide our understanding of the past (Lyell, 1830). This work is focused on developing and testing modern analogues that provide more accurate and precise estimates of prehistoric tropical cyclone intensity and earthquake magnitude by addressing two over-arching research goals:

1) Tropical cyclone intensity: can a tropical cyclone of known intensity provide links to the intensity of prehistoric tropical cyclones?
2) Earthquake magnitude: using modern day observations, can a proxy be used to quantify land-level subsidence from prehistoric earthquakes?

Chapter 1 characterized the sediments deposited by a tropical cyclone of known intensity to provide a modern analogue for reconstructing the flooding intensity of prehistoric tropical cyclones. This study provided a rare opportunity to characterize overwash sediments from a Category 5 tropical cyclone (10-minute sustained wind speeds as high as 270 km/hr) that made landfall in the South Pacific Islands of Vanuatu on March 13, 2015. Three months after landfall, I surveyed estimates of flow heights and inland extents of inundation and documented the sedimentological characteristics of Tropical Cyclone Pam deposits in two contrasting environments: (1) Manuro, a mixed-carbonate embayment, and (2) Port Resolution Bay, a volcaniclastic beach. Maximum flow heights associated with Tropical Cyclone Pam's coastal inundation

ranged from 3.30 m (at Port Resolution Bay) to 5.29 m (at Manuro) mean sea level. Tropical Cyclone Pam sediments displayed coarsening (at Manuro) and fining (at Port Resolution Bay) upward sequences. A limitation of studying long-term geologic records of prehistoric tropical cyclones is deciphering their flooding intensity (Brandon et al., 2013; Donnelly et al., 2015; Woodruff et al., 2015). Using Tropical Cyclone Pam overwash sediments from Port Resolution Bay, we apply an inverse sediment transport model (W08; Woodruff et al., 2008) using the largest average measured settling velocities. Results of the W08 model resulted in estimates of maximum flow depths within 5 to 11% of the measured value of 1.51 m. The successful application of a sediment transport model on volcanic sediments suggests that the assessment of the long-term variability in tropical cyclone intensity is possible with overwash sediments preserved in the geologic record.

Chapter 2 described and quantified how the inter- and intra-site variability in the distribution of modern diatoms (modern training set) across tidal wetlands can be used to reconstruct relative sea-level (RSL) rise caused by Cascadia subduction zone earthquakes. I collected samples for diatom and environmental analysis (elevation, grain-size, total organic carbon (TOC), porewater salinity, and nutrient concentrations) from three tidal marshes located in Willapa Bay: (1) the Bone River; (2) the Niawiakum River; (3) and the Naselle River. The modern training set consisted of 367 diatom species across 94 genera that captures the range of diatoms found in marine, brackish, and freshwater environments in Willapa Bay, WA. Hierarchical clustering and ordination of the training set identified floral zones at each tidal marsh with differing environmental controls. Two transects (Bone River Transect 1 and the Niawiakum River Transect) display a vertical zonation of diatom assemblages where diatoms can be used to distinguish the tidal flat, low marsh, and high marsh environment. The

Naselle River does not show vertical zonation as marine, brackish, and freshwater species are found in relatively high abundance across the transect with salinity as the major driver. Results of the regional training set shows that in spite of overlapping tidal environments and elevation, site-specific variability among dominant diatom assemblages exist. The findings show that the precision of diatom-based, relative sea-level reconstructions can be limited due to the high spatial variability of coastal diatoms in Willapa Bay that lead to a no matching analogue problem.

Chapter 3 created a novel approach for reconstructing relative sea-level (RSL) change caused by Cascadia subduction zone earthquakes at Willapa Bay, WA. Without instrumental or historical observations of Cascadia subduction zone earthquakes, microfossils (e.g., diatoms) preserved within intertidal stratigraphic sequences are the only means to reconstruct site-specific coastal subsidence estimates (e.g., Wang et al., 2013). Quantitative estimates of RSL rise from Cascadia subduction zone earthquakes have been hampered by site-specific diversity of diatom assemblages that lead to a no matching analogue problem from which fossil diatom comparisons are limited by a lack of present-day analogues from which to reconstruct past sea level (e.g., Nelson and Kashima, 1993). Using an established transfer function (weighted-averaging partial least squares) approach, all fossil samples (n = 77) had a poor modern analog. Using a novel dimension reduction approach, diatoms were grouped based on similarities in abundance and distribution with elevation. Results showed the grouping of species increased the proportion of good analogues in the fossil samples from 0 to 21%. I subsequently developed a new Bayesian diatom transfer function (BDTF) to integrate the grouped species while allowing for the addition of a stratigraphic prior (i.e., sediment lithology) that reduced uncertainty. The BDTF was applied to an intertidal stratigraphic sequence taken from the Redtail locality at Willapa Bay where six, mud-

over-peat contacts have been correlated to great ($M_w \geq 8.0$) Cascadia earthquakes (Atwater and Hemphill-Haley, 1997). I apply the Bayesian diatom transfer function in Cascadia to produce estimates of RSL rise from multiple Cascadia subduction zone earthquakes with reliable estimates from the 1700 CE earthquake (0.46 m ± 0.33 m) and the mud-over-peat contact of Soil U (0.51 m ± 0.34 m). Poor matching analogues were found for the mud-over-peat contacts of Soils S, N, L., and J, which suggests the modern intertidal environment from the training set does not capture the range of paleoenvironmental conditions that existed in Willapa Bay from ~1400 to 3500 yrs CE.

References

Atwater, B.F., 1987. Evidence for great Holocene earthquakes along the outer coast of Washington state. Science 22, 942-944.

Atwater, B.F., and Hemphill-Haley, E., 1997, Recurrence intervals for great earthquakes of the past 3,500 years at northeastern Willapa Bay, Washington: U.S. Geological Survey U.S. Geological Survey Professional Paper 1576.

Brandon, C.M., Woodruff, J.D., Lane, D., Donnelly, J.P., 2013. Tropical cyclone wind speed constraints from resultant storm surge deposition: A 2500 year reconstruction of hurricane activity from St. Marks, FL. Geochemistry, Geophysics, Geosystems 14, 2993–3008.

Donnelly, J.P., Butler, J., Roll, S., Wengren, M., Thompson, W., 2004. A backbarrier overwash record of intense storms from Brigantine, New Jersey. Marine Geology 210, 107-121.

Donnelly, J.P., Hawkes, A.D., Lane, P., MacDonald, D., Shuman, B.N., Toomey, M.R., van Hengstum, P.J., Woodruff, J.D., 2015. Climate forcing of unprecedented intense-hurricane activity in the last 2000 years. Earth's Future 3, 49–65. doi:10.1002/2014EF000274

Dura, T., Cisternas, M., Horton, B.P., Ely, L.L., Nelson, A.R., Wesson, R.L., Pilarczyk, J.E., 2014. Coastal evidence for Holocene subduction-zone earthquakes and tsunamis in central Chile. Quaternary Science Reviews 113, 93-111.

Hemphill-Haley, E., 1995a. Diatom evidence for earthquake-induced subsidence and tsunami 300 years ago in southern coastal Washing. Geol. Soc. Am. Bull. 107, 367-378.

Horton, B.P., Milker, Y., Dura, T., Wang, K., Bridgeland, W.T., Brophy, L., Ewald, M., Khan, N.S., Engelhart, S.E., Nelson, A.R., Witter R.C., 2017. Microfossil measures of rapid sea-level rise: Timing of response of two microfossil groups to a sudden tidal-flooding experiment in Cascadia. Geology 45, 4.

Joint Typhoon Warning Center (JTWC), 2015. JTWC Southern Hemisphere best track data 2014-2015. Online: http://www.usno.navy.mil/NOOC/nmfc-ph/RSS/jtwc/best_tracks/wpindex.php.

Liu, K., Fearn, M.L., 1993. Lake-sediment record of late Holocene hurricane activities from coastal Alabama. Geology 21, 793–796.

Lyell, C., 1830. Principles of geology, being an attempt to explain the former changes of the Earth's surface, by reference to causes now in operation. London: John Murray. Volume 1.

Mori, K., Kato, M., Kim, S., Mase, H., Shibutani, Y., Takemi, T., Tsuboki, K.,

Yasuda, T., 2014. Local amplification of storm surge by super typhoon Haiyan in Leyte Gulf. Geophysical Research Letters 41, 5106-5113.

Nelson, A.R., Kashima, K., 1993. Diatom zonation in southern Oregon tidal marshes relative to vascular plants, foraminifera, and sea level: Journal of Coastal Research, p. 673-697.

Nelson, A.R., Shennan, E., Long, A.J., 1996. Identifying coseismic subsidence in tidal-wetland stratigraphic sequences at the Cascadia subduction zone of western North America. J. Geophys. Res. 101, 6115-6135.

Pilarczyk, J.E., Horton, B.P., Soria, J.L.A., Switzer, A.D., Siringan, F., Fritz, H.M., Khan, N.S., Ildefonso, S., Doctor, A.A., Garcia, M.L., 2016. Micropaleontology of the 2013 Typhoon Haiyan overwash sediments from the Leyte Gulf, Philippines. Sedimentary Geology 339, 104-114.

Sawai, Y., Horton, B.P., Nagumo, T., 2004. The development of a diatom-based transfer function along the Pacific coast of eastern Hokkaido, northern Japan – an aid in paleoseismic studies of the Kuril subduction zone. Quaternary Science Reviews 23, 2467-2483.

Sawai, Y., Kamataki, T., Shishikura, M., Nasu, H., Okamura, Y., Satake, K., Thomson, K.H., Matsumoto, D., Fujii, Y., Komatsubara, J. Aug, T.T., 2009. Aperiodic recurrence of geologically recorded tsunamis during the past 5500 years in eastern Hokkaido, Japan. J. Geophys. Res. 114, 20.

Soria, J.L.A., Switzer, A.D., Villanoy, C.L., Fritz, H.M., Bilgera, P.H.T., Cabrera, O.C., Siringan, F.P., Maria, Y-S.Y., Ramos, R.D., Fernandez, I.Q., 2016. Repeat storm surge disasters of Typhoon Haiyan and its 1897 predecessor in the Philippines. Bulletin of the American Meterological Society 97, 31-48.

Wang, P.L., Engelhart, S.E., Wang, K., Hawkes, A.D., Horton, B.P., Nelson, A.R., Witter, R.C., 2013. Hetergeneous rupture in the great Cascadia earthquake of 1700 inferred from coastal subsidence estimates. Journal of Geophysical Research 118, 2460-2473.

Woodruff, J.D., Donnelly, J.P., Mohrig, D., Geyer, W.R., 2008. Reconstructing relative flooding intensities responsible for hurricane-induced deposits from Laguna Playa Grande, Vieques, Puerto Rico. Geology 36, 391–394.

Woodruff, J.D., Kanamaru, K., Kundu, S., Cook, T.L., 2015. Depositional evidence for the Kamikaze typhoons and links to changes in typhoon climatology. Geology 43, 91–94.

Yeats, R.S., Sieh, K.E., Allen, C.R., 1997. The Geology of Earthquakes. Oxford University Press, Oxford (568 pp.).

Zong, Y., Shennan, I., Combellick, R.A., Hamilton, S.L., Rutherford, M.M., 2003. Microfossil evidence for land move ments associated with the AD 1964 Alaska earthquake. Holocene 13, 7-20.

Chapter 1: Sedimentological characteristics of the 2015 Tropical Cyclone Pam overwash sediments from Vanuatu, South Pacific

Abstract

Although sediments deposited by prehistoric tropical cyclones (TC's) improve our understanding of landfalling storms, they are limited by a lack of modern analogues, particularly in the South Pacific. On 13 March 2015, Tropical Cyclone Pam made landfall on Vanuatu, reaching Category 5 intensity with 10-minute sustained wind speeds as high as 270 km/h. Three months after landfall, we measured estimates of flow depth and inland extent of TC Pam's storm surge, and described the sedimentological characteristics of the TC Pam overwash sediments from trenches and transects of two sites. At Manuro (a mixed-carbonate embayment) the TC Pam sediments transition from a coarse- to medium-grained (mean: 1.07 Φ) carbonate sand (≤ 10 cm thick) to pumice (≤ 18 cm thick) that extends 400 m inland into Lake Otas. At Manuro, the TC Pam overwash sediments are characterized by a coarsening upward sequence (1.45 to 0.23 Φ) followed by a fine-grained eolian cap. At Port Resolution Bay (a volcaniclastic beach, PRB), the TC Pam overwash sediments transition from a medium-grained (mean: 1.76 Φ) volcanic sand (≤ 44 cm thick) to pumice (≤ 5 cm thick) that extends 320 m from the shoreline. A subtle fining upward sequence was present in trench PRB2, whereas PRB1, PRB3, and PRB4 contained TC Pam sediments that were laminated and showed little to no vertical gradation in grain size. Flow depths associated with TC Pam's storm surge ranged from 3.3 m to 5.5 m above mean sea level (MSL). Using laboratory derived settling velocities and the distance from the berm, we applied an inverse sediment transport model to reconstruct a field-measured estimate of flow depth at PRB (3.3 m total, 1.51 m over the berm). By using the largest average settling

velocity, we reconstruct Pam's estimated maximum flow depth over the berm (1.51 m) to 1.43 m (PRB2), 1.36 m (PRB3), and 1.34 m (PRB4) above MSL.

1. Introduction

Observational records are insufficient in capturing the timescales necessary to assess the long-term variability in tropical cyclone (TC) frequency and intensity (e.g., Woodruff et al., 2009; Brandon et al., 2013; Donnelly et al., 2015). However, regions vulnerable to landfalling TC's archive robust long-term geologic records of prehistoric events in the form of overwash sediments (e.g., Liu and Fearn, 1993, 2000; Donnelly and Woodruff, 2007). Overwash sediments in tropical environments are recognized as layers of coarse sediments that are preserved in low-energy coastal environments such as agricultural fields (e.g., rice fields), back-barrier vegetated areas, and ponds where they normally would not occur (Brill et al., 2016; Pilarczyk et al., 2016; Soria et al., 2018).

Without modern analogues, it is difficult to identify prehistoric TC overwash sediments. Overwash sediments of modern landfalling TC's have been analyzed from North America (e.g., Fritz et al., 2007; Horton et al., 2009; Hawkes and Horton, 2012), the Philippines (e.g., Soria et al., 2016; Brill et al., 2016), and elsewhere (e.g., Nott et al., 2009). However, no modern analogues exist from the South Pacific. A further problem of studies of prehistoric land falling TC's is deciphering their flooding intensity (Brandon et al., 2013; Donnelly et al., 2015; Woodruff et al., 2015). Woodruff et al. (2008) developed an inverse sediment transport model (W08) to estimate the paleosurge depth required to deposit overwash sediments into a siliciclastic, semi-tropical lagoon located in Vieques, Puerto Rico. The W08 model calculations of flow depth over the berm matched storm surge estimates based on offshore bathymetry and meteorological observations. The W08 model has also been successfully applied to reconstructing TC's in Laguna Madre, Texas (Wallace and Anderson, 2010), Shikoku,

Japan (Baranes et al., 2016), Staten Island, New York (Brandon et al., 2014), and Hancock County, Mississippi (Bregy et al., 2018), but remains untested with volcanic sediments in the South Pacific.

Here, we survey estimates of flow depths and inland extents, and document the sedimentological characteristics of the Category 5 TC Pam, which made landfall on Vanuatu on 13 March 2015 (Fig. 1). We investigated two contrasting environments: Manuro, a mixed-carbonate embayment on Efate Island; and Port Resolution Bay (PRB), a volcaniclastic beach on Tanna Island (Fig. 1). Flow depths associated with TC Pam's storm surge ranged from 3.3 m to 5.5 m above mean sea level (MSL). Trenches Manuro and PRB contained coarsening (e.g., M1) and fining (e.g., PRB2) upward sequences. Using TC Pam overwash sediments at PRB, we apply the W08 model using the largest average measured settling velocities from trenches 50 to 63 m from the berm. The W08 calculations of TC Pam's flow depths over the berm are within 5% to 11% of the measured 1.51 m. Our successful application of the W08 inverse sediment transport model has implications for reconstructing the intensity of prehistoric landfalling TC's in locations dominated by volcanic sediments such as those found in many Pacific Rim environments.

1.1 Tropical Cyclone Pam

TC Pam began as Tropical Disturbance 11F and was upgraded to TC status at 5:01 UTC on 9 March 2015, 1000 km northeast of the Solomon Islands (Bosserelle, 2015). At 15:00 UTC, the system began a southward path toward Vanuatu (Jenner, 2015; Bosserelle, 2015). By 13 March, TC Pam reached Category 5 intensity with 10-minute sustained wind speeds as high as 270 km/h (Bosserelle, 2015). At approximately 12:00 UTC on 13 March, TC Pam made landfall on Efate Island (Bosserelle, 2015; Jenner,

2015) and began weakening in intensity as it continued to move southwest along the western coasts of Erromango and Tanna islands (Fig. 1). On 14 March, TC Pam downgraded to Category 4 intensity as it passed west of Aneityum, the southernmost inhabited island in Vanuatu (World Bank, 2015; New Zealand MetService, 2015). TC Pam continued to weaken over the South Pacific until it dissipated on 22 March 2015 (Jenner, 2015).

A combination of high wind speeds, riverine runoff, and coastal flooding caused severe damage to coastal villages on Efate and Tanna islands. Initial relief efforts (Red Cross, 2016) began in east Efate, one of the areas most heavily damaged by TC Pam. In Eton, a village located 6 km southwest from the Manuro site, a maximum run-up height of 5.1 m above MSL was measured (Fig. 1c; Nishijima et al., 2015).

2. Setting

2.1 Vanuatu

Vanuatu is an island nation in the southwestern Pacific located east of Australia and north of New Zealand (Fig. 1). Formation of the island arc began during the Oligocene to mid-Miocene and was followed by periods of volcanism and reef development (Greene, 1984; Meffre and Crawford, 2001; Buys et al., 2014). Vanuatu is separated into three geologic provinces: the Western Belt; the Eastern Belt; and the Central Chain (Coleman, 1970; Carney and MacFarlane, 1979). Our study is focused on Efate and Tanna islands located in the Central Chain (Carney and MacFarlane, 1979). Efate Island is comprised of Pleistocene trachydacite and basalt surrounded by uplifted Quaternary reef formations (Ash et al., 1978; Taylor et al., 1987; Stewart et al., 2010). Tanna Island

is comprised of Pliocene to Quaternary andesite and uplifted reef limestone (Firth et al., 2014; Brothelande et al., 2015).

The climate of Vanuatu is tropical and largely influenced by its location within the South Pacific Convergence Zone (SPCZ) that generates at least 6 mm of rainfall per day when the SPCZ is at its maximum extension during the austral summer (November-March; Vincent, 1994; Griffiths et al., 2003; Wirrmann et al., 2011). Interannual variability of the SPCZ and high sea surface temperatures make Vanuatu vulnerable to TC's (e.g., TC's Uma in 1987; Fran in 1992; Prema in 1993; Paula in 2001; and Ivy in 2004). Despite the history of recent landfalling TC's in Vanuatu, little is known prior to TC Uma in 1987 (JTWC, 2015).

2.2 Manuro, Efate Island

TC Pam made direct landfall on the southeast corner of Efate Island, the most populated island of Vanuatu. Our study site, Manuro, is a low-lying coastal embayment on the easternmost point of Efate Island (Fig. 1). Local residents confirmed that TC Pam inundated the coastline. Manuro is a shallow, narrow inlet with a wide (70 m) beach that transitions to a vegetated area and is bounded on its western side by Lake Otas. Wave energy along this section of the coast can be high; however, Manuro's narrow, microtidal embayment (tide range <1 m) reduces the wave energy that impacts the beach (IOC, 2016). A fringing reef extends parallel to the shoreline and generates biogenic sediment that accumulates on the beach (Ash and Carney, 1987). Intertidal and supratidal sediments are composed of biogenic carbonate with trace amounts of mafic volcanics (Ash and Carney, 1987). A seaward sloping beach extends 115 m inland and is bordered by raised Pleistocene reefs and *Pandanus sp*. trees (Fig. 2). At a distance of 115 m from the shoreline, the beach transitions to a vegetated area that is

characterized by sparsely covered low-lying shrubs and grasses (Fig. 2; Ash and Carney, 1987). Lake Otas is a freshwater coastal lake and is located at a distance of 400 m from the shoreline and is connected to the embayment by a seaward sloping ephemeral river (Fig. 1 and 2).

2.3 Port Resolution Bay, Tanna Island

According to resident interviews, PRB experienced marine inundation by storm surge and backwash from Lake Eweya. TC Pam traveled 15 km west of Tanna Island before downgrading to Category 4 intensity. Our study site, PRB, is a narrow beach (40 m wide) located on the southwestern side of a cliffed and rocky northward-facing bay on the easternmost point of Tanna Island (Fig. 1). Lake Eweya is connected to the bay by a narrow tidal channel and is located behind the vegetated area at a distance of 190 m from the coast (Fig. 1h). Wave energy is low at this microtidal beach due to the shallow bathymetry and narrow opening that characterize the bay (IOC, 2016). The beach is composed predominantly of mafic to intermediate volcanic sediments (i.e., andesite to basaltic andesite) that are sourced from the Siwi caldera, with minor amounts of carbonate material (e.g., nearshore foraminifera) present (Kosicuch et al., 2018). PRB is situated on the southern flank of the Siwi caldera (e.g., Brothelande et al., 2015) and is bounded on its southern side by a river that runs west to east. At our site, a narrow beach with a continuous, shore-parallel berm (elevation is 1.79 m above MSL; Fig. 2) transitions to a vegetated area of coconut trees and grassy plain that is bounded by the brackish Lake Eweya (Fig. 1h).

3. Methods

3.1 Field survey and sample collection

In June 2015, three months after TC Pam made landfall, we surveyed estimates of flow depths, and described and collected overwash sediments deposited by the storm surge. Interviews with local residents guided our survey of the inundation. At both Manuro and PRB, we surveyed the inundation distance and elevation of rafted debris to estimate flow depth using a Trimble GPS rover connected to a Lasercraft laser range finder (Fig. 1; Fritz et al., 2009; Soria et al., 2016). At PRB, discrete survey points of the wrack line were marked in lieu of continuous surveying because dense vegetation and a river inhibited the deposition of a clear and continuous wrack line (Fig. 1). We mapped major changes in the lithology of the overwash sediments (e.g., sand to pumice transitions; Fig. 2) and dug trenches. At each trench site from Manuro (M1) and PRB (PRB1-4), we measured the surface elevation and described the depth, color, sedimentary structure, and lithology of every stratigraphic unit. At M1, we collected samples at 3 cm intervals within the TC Pam overwash sediments and the underlying layer up to a depth of 24 cm below the surface. At PRB, we dug four trenches (PRB1, PRB2, PRB3, and PRB4) and collected samples at intervals ranging from 0.5 to 1 cm near lithologic contacts, and 1 to 2 cm within continuous and homogeneous sediment. Sediment samples collected from trenches were stored in plastic wrap and refrigerated until they were analyzed for grain-size distributions and settling velocity.

3.2 Grain size analysis

We measured the grain-size distributions of the sampled trenches at Manuro (M1) and PRB (PRB1-4). We used 30% H_2O_2 to digest the organic fraction of the sampled

trenches to prepare the samples for grain-size measurements (Donato et al., 2009). Grain-size distributions (-1.81 to 11.1 Φ) were obtained using a Malvern Mastersizer 3000 laser particle-size analyzer. We gridded the grain size data using a triangular irregular network (TIN) algorithm (Sambridge et al., 1995; Donato et al., 2009) and plotted the volume of grains in each size class using the Geosoft Oasis TM software (Donato et al., 2009). GRADISTAT software (Blott and Pye, 2001) was used to calculate the following grain size statistics according to Folk and Ward (1957): mean (average grain size), sorting (grain size variation), skewness (symmetry of the grain size distribution), and kurtosis (peakedness of the grain size distribution). We also report the 10th (d10), 50th (d50), and 90th (d90) percentiles of grain size diameters to identify subtle fining or coarsening trends (Tables S2-S6).

We applied detrended correspondence analysis (DCA) on the grain-size distribution (-1.81 to 11.1 Φ) per sampled depth of sediments to note any variation within and between the TC Pam overwash sediments and the underlying units at each trench (Hill and Gauch, 1980).

3.3 Modeling storm inundation at Port Resolution Bay

3.3.1 Measuring settling velocity

The inverse sediment transport model developed by Woodruff et al. (2008) used the theoretical settling value for siliciclastic sediment (Ferguson and Church, 2004), which has been found to be appropriate in several backbarrier settings (Wallace and Anderson, 2010; Brandon et al., 2014; Baranes et al., 2016; Bregy et al., 2018). However, the andesitic volcaniclastics of Vanuatu have highly variable sediment densities (Whitham and Sparks, 1986; Carney and MacFarlane, 1979; Firth et al., 2014), resulting in a range

of settling velocities. We calibrated the W08 model from measured settling velocities of overwash sediments at PRB and compared them to theoretical values for andesitic material (Ferguson and Church, 2004; Woodruff et al., 2008). We did not apply the model to Manuro because the coastline is flat, slopes seaward, and lacks a berm, making it difficult to input a source and distance of the coarsest grains in the modern environment and also likely means that resuspension dominates settling.

We conducted settling velocity (w_s) measurements on the coarsest grain sizes available in trenches PRB1-4 using a settling tube (Syvitski et al., 1991; Woodruff et al., 2008). We selected 20 intervals within the four trenches and dry sieved each sample at -1 Φ, 0 Φ, and 1 Φ intervals to isolate the coarsest fraction (Table 1, S1). The 15 coarsest grains, andesitic in composition, were dropped individually into the water-filled settling tube. The settling tube was a 2.45 m tall, 10 cm wide transparent polycarbonate cylinder filled with 10 L of 20°C water. Instant Ocean crystals were mixed with the water to obtain a salinity of 35 ppt, the average surface salinity of the Pacific Ocean. The 2.45 m height of the settling tube was appropriate to allow the coarsest grains to reach terminal velocity (Bryant et al., 1987). To observe distance traveled and time passed, we placed a scale (cm) behind, and a timer adjacent to, the base of the transparent cylinder. We filmed each grain as it settled to the base of the cylinder using a Canon EOS Rebel T6-S digital camera.

We calculated the w_s of each grain using Adobe Photoshop (v. CS6) by importing the captured footage as discrete video frames and measuring the diameter of each sediment grain as well as the distance it traveled between frames (Smith and Friedrichs, 2011). We calibrated the measured distances from pixels to cm to calculate settling velocity (cm/s). To avoid bottom boundary effects, we ceased measurement at a distance of 10

cm from the bottom of the settling tube. We determined the elapsed time interval using the time stamped on the footage between frames. The settling velocities of the 15 grains were used to calculate the average settling velocity of the coarsest subsampled interval of sediment (Woodruff et al., 2008).

3.3.2 Sediment transport modeling

We applied the W08 model to TC Pam sediments at Port Resolution Bay, a volcaniclastic-dominated environment:

$$h_b = \left(\frac{x_L^2 w_s^2}{g}\right)^{1/3} \quad (1)$$

Where h_b is the maximum estimated flow depth (m) above the berm at PRB, x_L is the distance of grains advected landward from the berm (m), w_s is the settling velocity (m/s) as measured in a laboratory settling tube, and g is gravity (9.81 m/s^2). For h_b, we selected the estimated maximum flow depth that was measured during our survey (3.30 m above MSL) at PRB (Fig. 2) and subtracted the terrain elevation of the berm (1.79 m above MSL) to obtain a maximum flow depth over the berm (h_b) of 1.51 m. PRB is well suited to the application of the W08 model because (1) PRB shares similarities with the initial W08 study area in that flooding caused by TC Pam was likely dominated by wave run-up due to deep water offshore; (2) it is located in an enclosed bay with a berm that acts as a barrier, which also serves as a coarse sediment source during periods of marine inundation; and (3) there is evidence of settling during horizontal transport. By using the coarsest available grains, it is possible to assume that the settling of sediment exceeds resuspension rates (Woodruff et al., 2008). We assume that transport distances are from the berm to the trenches (Woodruff et al., 2008).

4. Results

4.1 TC Pam sediments at Manuro, Efate Island

Surveying of the wrack line indicates an inundation path that narrows from the coast until it reaches Lake Otas (Fig. 1g). The wrack line consists of branches, coconuts, and pumice. We measured an estimate of maximum flow depth of 4.2 m above MSL and an inundation distance of 400 m from the shoreline. Our measured inundation distance is a minimum estimate, because we were unable to access the densely vegetated area behind Lake Otas (Fig. 1e). A shore-perpendicular elevation transect revealed that TC Pam deposited an overwash sand (≤ 10 cm thick) up to 130 m inland, that abruptly changed to a pumice layer (≤ 18 cm thick) that extended a minimum of 400 m inland into Lake Otas, as we were unable to determine how far the submerged sediment extended (Fig. 2). The overwash sand is coarse- to medium-grained and is capped by a finer-grained, eolian sand (Fig. 3b).

Trench M1 has the maximum thickness of TC Pam overwash sediments at Manuro and is at the landward extent of the TC Pam sand. The underlying soil (18 to 24 cm depth) is a brown, medium-grained (mean: 1.37 Φ; SD: 0.03), moderately well-sorted (0.57 to 0.59 Φ) organic-rich sand with a dense concentration of roots (Fig. 3a; Table S2). The grain-size distribution of the underlying organic-rich sand is homogeneous, lacking any fining or coarsening upward trends (Fig. 3a; Table S2). A sharp contact separates the underlying soil from the overlying overwash sand. The overlying TC Pam sediment (3 to 13 cm depth) is a similar coarse- to medium-grained (mean: 1.07 Φ; SD: 0.56), moderately well-sorted (0.51 to 0.59 Φ) foraminifera-bearing carbonate sand with trace amounts of volcanic sediments and fragments of corals and mollusks (Fig. 3a; Table S2). Detailed descriptions of foraminifera within TC Pam sediments are presented in

Kosciuch et al. (2018). Grain-size analysis indicates a coarsening upward trend from 12 cm (mean: 1.45 Φ) to 3 cm (mean: 0.23 Φ) depth. From 0 to 3 cm is a finer-grained (mean: 1.29 Φ), eolian sediment cap (Fig. 3a; Table S2).

DCA confirms the grain size descriptions. There is no distinction between overwash sediments and the underlying organic sand. DCA axis scores, however, do show the coarsening upwards sequences between 3 and 12 cm, and the distinction with the eolian sediment cap (Fig. 3a).

4.2 TC Pam sediments at Port Resolution Bay, Tanna Island

Surveying of the wrack line traced a continuous boundary on the western side of PRB but was limited to a single measurement on the eastern side of the bay due to dense vegetation and irregular topography caused by the presence of a river (Fig 1h). The wrack line consists of palm fronds, coconuts, pumice, and rounded, bleached coral boulders (< 50 cm diameter). We measured an estimate of maximum flow depth of 3.3 m above MSL at the highest surveying point with a corresponding inundation distance of 320 m from the shoreline at PRB. TC Pam deposited sand (≤ 44 cm thick) over a grassy plain, up to 100 m inland (Fig. 2). We traced pebble-sized (< 3.3 Φ) pumice (≤ 5 cm thick) from the bottom of the seaward shore of Lake Eweya (175 m inland) to the opposite shore of the lake, 320 m inland (Fig. 2). The overwash sediment is composed of a medium- to fine-grained sand which is capped by very fine-grained, eolian sand.

We described and collected samples from four trenches (PRB1-4) ranging in depth from 20 to 60 cm (Fig. 1h). Trench PRB1 is closest to the shore and contains a 12 cm-thick gray sand layer with three separate laminations within the TC Pam sediments from 5 to 6 cm, 9 to 10 cm, and 13 to 14 cm depth (Fig. 4a). A gradational contact separates the

base of the sand and the underlying layer. The underlying layer (14 to 20 cm) is a dark brown, medium-grained (mean: 1.70 Φ; SD: 0.20), moderately well-sorted (0.61 to 0.64 Φ) rooted sandy soil (Table S3). The grain-size distribution of the underlying organic-rich sand is homogeneous, lacking any clear fining or coarsening upward trends (Fig. 4a). The overlying TC Pam overwash sediment (2 to 14 cm) is a medium-grained sand (mean: 1.70 Φ; SD: 0.19) that is moderately well-sorted (0.57 to 0.69 Φ) and composed of volcanic sand with trace amounts of foraminifera and shell fragments (Table S3). Detailed descriptions of foraminifera within TC Pam sediments are presented in Kosciuch et al. (2018). The laminae are composed of medium-grained (mean: 1.87 Φ; SD: 0.21), moderately well-sorted (0.56 to 0.65 Φ) sand. Grain-size analysis shows no significant fining or coarsening trend in the vertical distribution of the sediment.
DCA confirms the grain size descriptions. There is no distinction between the overwash sediments and the underlying sandy soil. DCA axis scores, however, do show a subtle distinction with the laminae and eolian sediment cap (Fig 4a).

Moving inland, trench PRB2 preserved a 44 cm-thick gray sand layer with multiple thin (1 cm) laminations interbedded with TC Pam overwash sediments (Fig. 4b). A sharp contact separates the base of the overwash sediments and the underlying layer. The underlying layer (47 to 58.5 cm) is a dark brown, medium-grained (mean: 1.67 Φ; SD: 0.16), moderately to moderately well-sorted (0.62 to 0.74 Φ) rooted sandy soil (Table S4). The grain-size distribution of the underlying organic-rich sand is homogeneous with the exception of a single coarse peak in d10 values from 48 to 54.5 cm from the surface (Fig. 4b). The overlying TC Pam overwash sediments (0.5 to 44.5 cm) consist of a medium-grained (mean: 1.57 Φ; SD: 0.19), moderately to moderately well-sorted (0.59 to 0.76 Φ) volcanic sand with trace amounts of foraminifera and shell fragments (Table S4). Detailed descriptions of foraminifera within TC Pam sediments are

presented in Kosciuch et al. (2018). The laminae are composed of fine-grained (mean: 2.47 Φ; SD: 0.12), moderately-sorted (0.88 to 0.96 Φ) sand. A fining upward sequence of the TC Pam overwash sediments is observed from a mean grain size of 1.44 Φ at 16.5 cm depth to 2.53 Φ at 0.5 cm (Fig. 4b).

DCA confirms the grain size descriptions. There is no distinction between the overwash sediments and the underlying sandy soil. DCA axis scores, however, do show a subtle distinction with the laminae and eolian sediment cap (Fig. 4b).

Trench PRB3 contains a 24.5 cm-thick gray sand layer with laminations interbedded in the upper half of the TC Pam overwash sediments (Fig. 4c). A sharp contact separates the base of the overwash sediments and the underlying layer. The underlying layer (26.5 to 30.5 cm) is a dark brown, fine-grained (mean: 1.99 Φ; SD: 0.03), moderately-sorted (0.85 to 0.89 Φ) rooted sandy soil (Table S5). The grain-size distribution of the underlying organic-rich sand is homogeneous with no discernable vertical change in grain size (Fig. 4c). The TC Pam overwash sediments (2 to 26.5 cm) consist of a medium-grained (mean: 1.72 Φ; SD: 0.14), moderately to moderately well-sorted (0.59 to 0.77 Φ) volcanic sand with trace amounts of foraminifera and shell fragments (Table S5). Detailed descriptions of foraminifera within TC Pam sediments are presented in Kosciuch et al. (2018). The laminae at 2.5 to 4.5 cm, 6.5 to 7.5 cm, and 12.5 to 13.5 cm are finer grained (mean: 2.21 Φ; SD: 0.22) than both the TC Pam overwash sediments and the underlying rooted sandy soil. Grain-size analysis reveals no distinct vertical trend through the TC Pam overwash sediments (Fig. 4c; Table S5).

DCA confirms the grain size descriptions. There is no distinction between the overwash sediments and the underlying sandy soil. DCA axis scores, however, do show a distinction with the eolian sediment cap (Fig. 4c).

Trench PRB4, the farthest inland trench, preserved a 25 cm-thick gray sand layer with multiple thin (≤ 1 cm) laminations interbedded in the upper half of the TC Pam overwash sediment (Fig. 4d). A sharp contact separates the base of the sand and the underlying layer. The underlying layer (27 to 33 cm) is a dark brown, medium-grained (mean: 1.91 Φ; SD: 0.08), moderately to moderately well-sorted (0.69 to 0.95 Φ) rooted sandy soil (Table S6). The underlying organic-rich sand layer is homogeneous with no discernable vertical change in grain size (Fig. 4d). The TC Pam overwash sediment (2 to 27 cm) is a medium-grained (mean: 1.84 Φ; SD: 0.13), moderately to moderately well-sorted (0.59 to 0.73 Φ) volcanic sand with trace amounts of foraminifera and shell fragments (Table S6). Detailed descriptions of foraminifera within TC Pam sediments are presented in Kosciuch et al. (2018). The laminae are finer grained (mean: 2.28 Φ; SD: 0.27) than both the TC Pam overwash sand and the underlying rooted sandy soil (Fig. 4d; Table S6).

DCA confirms the grain size descriptions. There is no distinction between the overwash sediments and the underlying sandy soil. DCA axis scores, however, do show a subtle distinction with the eolian sediment cap (Fig. 4d).

4.3 Inverse sediment transport model

We calculated a maximum flow depth (h_b) of 1.51 m over the berm by subtracting the elevation of the berm (1.79 m) from the maximum measured estimate of flow depth of TC Pam at PRB (3.30 m). To test the applicability of the Woodruff et al. (2008) model to our volcaniclastic site at PRB, we used the distance from the trench to the berm (14.9 to 63.0 m) as our transport distance (x_L) and the average settling velocities (w_s) derived from our laboratory observations to the equation.

We calculated 15 settling velocities per 1-cm interval of the coarsest (-1.18 to 0.05 Φ) TC Pam overwash sand at trenches PRB1-4, avoiding the laminae, from a total of 45 settling velocity measurements at PRB1, 105 at PRB2, 60 at PRB3, and 90 at PRB4. We report the average settling velocities across discrete depths based on multiple runs (Table 1). We do not observe a linear trend in increasing settling velocity with increasing grain size (Fig. 5), highlighting the variability of volcanic lithology at our site. There is a general trend of decreasing settling velocities with distance from the berm. The average settling velocities range from 7.46 to 10.8 cm/s (mean: 9.57; SD: 1.84) at PRB1; 6.96 to 10.7 cm/s (mean: 9.13 cm/s; SD: 1.38) at PRB2; 6.04 to 8.44 cm/s (mean: 7.10 cm/s; SD: 1.12) at PRB3; and 6.72 to 7.67 cm/s (mean: 7.25 cm/s; SD: 0.33) at PRB4 (Table 1).

We applied the average settling velocities of PRB1-4 to Equation 1 to reconstruct h_b values using the associated distance from the berm x_L (Table 1). Flow depths are all systematically underestimated compared to the measured value of 1.51 m due to average settling velocities being slower than predicted values at all trench distances from the berm (Woodruff et al., 2008). However, with the exception of trench PRB1, we were able to calculate flow depth (h_b) values within 5% to 11% of the field-measured estimated value by using the highest single average settling velocities per trench. For example, we calculated h_b values for trenches PRB2, PRB3, and PRB4 as 1.43 m, 1.36 m, and 1.34 m, respectively (Table 1). PRB1, which is nearest to the berm, has a h_b value of 0.64 m.

5. Discussion

5.1 Sediments deposited by TC Pam

The TC Pam pumice layers extended farther than the sand layer by 270 m at Manuro and 220 m at PRB, suggesting they are a closer approximation of inundation distance by a storm surge. Sandy overwash sediments generally extend only a fraction of the actual inland extent of a storm surge (e.g., Pilarczyk et al., 2016). Although much larger in size than the sand, the vesicles in the pumice prevent it from quickly settling out of the water column, allowing it to raft inland much farther than the sand (Whitham and Sparks, 1986). The combination of its composition and durability makes pumice uniquely suited for identifying and interpreting paleostorms in the geologic record. This overwash indicator is applicable to locations where active volcanism produces accumulations of pumice that become concentrated in the nearshore environment (Cita and Aloisi, 2000; Fruendt et al., 2005; Nott, 2006).

The TC Pam overwash sediments provide a modern analogue for future studies of TC's in tropical environments. The grain-size, sorting, and sedimentary structures of the overwash sediments are characteristic of TC sediments. With the exception of PRB1, the trenches at Manuro and PRB have a sharp contact that separates the base of the TC Pam sand with the underlying rooted, organic-rich sandy soil (Fig. 3 and 4). Previous prehistoric TC studies from the U.S. Atlantic and Gulf coasts describe a sharp, basal contact between an overwash deposit and the underlying organic-rich layer (Donnelly and Woodruff, 2007; Horton et al., 2009; Hawkes and Horton, 2012). The grain-size distributions of Manuro and PRB, however, did not differentiate the TC Pam sediments from the underlying unit, because of the sandy environments. Similarly, a study of Typhoon Haiyan overwash sediments in the Philippines by Brill et al. (2016) showed

grain-size distributions similar to the underlying unit. Rather, sedimentary structures such as coarsening and fining upward sequences and lamination distinguished TC Pam sediments from the homogeneous underlying layers. At M1, TC Pam sediments show a distinct coarsening upward sequence (Fig. 3). A subtle fining upward sequence was present in trench PRB2 (Fig. 4). Although there was no vertical gradation in grain size in trenches PRB1, PRB3, and PRB4, all four trenches (PRB1-4) contained finer-grained laminae. Multiple, thin laminated beds and sedimentary structures are common characteristics of TC sediments (Kortekaas and Dawson, 2007; Switzer and Jones, 2008). These laminations are more organic rich than the TC Pam overwash sediments, suggesting they are sourced from the brackish Lake Eweya or the underlying soil. However, the laminae are finer grained than the underlying soil, providing compelling evidence that the laminae were deposited by backwash from Lake Eweya, the only source of fine-grained particles at PRB. Trenches PRB2-4 are particularly ideal locations for capturing a backwash signal because they are located in a depression seaward of Lake Eweya (Hawkes et al., 2007).

The TC Pam overwash sediments at Manuro and PRB differed in lithology. Manuro overwash sediment contained foraminifera-bearing carbonate sand, coral and mollusk fragments, and trace amounts of volcanic sediments whereas PRB overwash sediment contained volcanic sand with trace amounts of carbonate material. The difference in lithology of TC Pam sediments is due to the geology of the sites and the types of sediment available for transport by the storm surge. Manuro is largely composed of biogenic carbonate sourced from the fringing reef (Ash and Carney, 1987). In contrast, PRB is largely composed of andesitic sediment sourced from the Siwi caldera (Carney and MacFarlane, 1979; Firth et al., 2014; Brothelande et al., 2015).

5.2 Inverse modeling of the TC Pam overwash sediments

Inverse sediment transport modeling (Woodruff et al., 2008) was applied at PRB using measured settling velocities of the coarsest material. The W08 model assumptions appear valid, namely that settling of coarse material dominates resuspension from a known transport distance (Woodruff et al., 2008).

By applying the inverse settling transport model by Woodruff et al. (2008) to our site at PRB, we were able to reconstruct the calculated h_b value of 1.51 m (3.30 m measured high water level minus the elevation of the 1.79 m berm) within ~11%. The only exception is trench PRB1 (calculated h_b value of 0.64 m) due to sampling too close to the berm, which was also not effective in Woodruff et al. (2008). The results of the model show that the largest average settling velocities effectively estimate flow depths over the berm similar to previous studies (Woodruff et al., 2008; Wallace and Anderson, 2010; Brandon et al., 2014; Baranes et al., 2016; Bregy et al., 2018). Our study is the first to do so based solely on empirically derived settling velocities for the South Pacific.

To test the importance of measuring site-specific settling velocities, we compared our laboratory settling velocities with theoretical determinations (Woodruff et al., 2008). The theoretical settling velocity for naturally shaped andesitic volcanic sediments (Fig. 5; Ferguson and Church, 2004) consistently overestimated the settling velocity from PRB by 4.38 to 11.3 cm/s (Fig. 5, Table S1). This suggests that the volcanic sediments were sourced from multiple volcanic eruptions, each of which formed at different rates, resulting in a wide range of densities (Whitham and Sparks, 1986; Carney and MacFarlane, 1979; Firth et al., 2014). Furthermore, theoretical settling velocity predictions for spherical, angular, and intermediate shaped grains overestimated the

settling velocities of our samples (Table S1; Ferguson and Church, 2004). Deviations from the theoretical settling velocity are likely due to the mixed grain shape and density of our study areas (Whitham and Sparks, 1986; Carney and MacFarlane; Firth et al., 2014). Whereas the models assume a uniform grain shape and density of the sediments, the reality of our samples suggest these characteristics are highly variable at our sites. Theoretical settling values underestimate our measured h_b values from PRB1 between 38% to 55%, and consistently overestimate our measured h_b values from PRB2 between 3% to 47%, PRB3 between 37% to 51%, and PRB4 between 46% to 54%. For example, the theoretical settling velocity for PRB2 sediments from 36.5 to 37.5 cm depth is 20.0 cm/s, producing an h_b value of 2.17 m. In comparison, we measured a settling velocity of 10.7 cm/s, producing an h_b value of 1.43 m. Future studies in mixed-sediment environments will continue to require site-specific calibrations of settling velocities (Woodruff et al., 2008). Applying the sediment transport model to overwash sediments preserved in the geologic record will lead to a better understanding of the long-term patterns of TC frequency and intensity for the South Pacific region.

6. Conclusion

TC Pam provides a modern analogue to characterize sediments deposited by a TC of known intensity. We (1) measured the estimated flow depth and inland extent of TC Pam's storm surge; and (2) described the sedimentological characteristics of the TC Pam sediments from Manuro and PRB on the islands of Efate and Tanna, respectively. We measured estimations of flow depths of 4.2 m above MSL at our study area Manuro on Efate and 3.3 m above MSL at our study area PRB on Tanna. A lateral transition from sand to pumice at both Manuro and PRB suggests the applicability of pumice as

an indicator of maximum storm surge inundation. We found coarsening upward in the trench at Manuro (M1) and fining upward in trench PRB2.

We validated an inverse sediment transport model on TC Pam sediments deposited in PRB, a volcaniclastic environment. By applying the model by Woodruff et al. (2008) to our site at PRB, we calculated the measured h_b value of 1.51 m (3.3 m measured estimation of high water level minus the elevation of the 1.79 m berm) within 5% to 11% by applying the distance from the berm to the trench locations and the average measured w_s values from trenches PRB2-4 (Table 1). Theoretical settling velocities were higher than measured values, and if used would have over greatly overestimated flow depths.

Acknowledgements

We thank landowners on Efate and Tanna islands for granting access to their property. This work was supported by the National Science Foundation (EAR-1545619). This work is a contribution to IGCP Project 639, "Sea-level change from minutes to millennia." Reviews by two anonymous reviewers led to improvements in the manuscript.

References

Ash, R.P., Carney, J.N., MacFarlane, A., 1978. Geology of Efate and Offshore Islands. New Hebrides Condominium Geological Survey Regional Report Series, Port Vila. Vanuatu.

Bagnold, R.A., 1954. Experiments on a gravity free dispersion of large solid spheres in a Newtonian fluid under shear. Proc. R. Soc. Lond. A 225, 49-63.

Baranes, H.E., Woodruff, J.D., Wallace, D.J., Kanamaru, K., Cook, T.L., 2016. Sedimentological records of the CE 1707 Hōei Nankai Trough tsunami in the Bungo Channel, southwestern Japan. Natural Hazards, 1-21.

Blott, S.J., Pye, K., 2001. GRADISTAT: a grain size distribution and statistics package for the analysis of unconsolidated sediments. Earth surface processes and Landforms 26, 1237–1248.

Bosserelle, C., 2015. VMGD Secretariat of the Pacific Community. Tropical Cylone Pam waves summary. Online: http://pcrafi.spc.int/static/pam/TropicalCyclonePamSwellSummary.pdf (accessed 8.9.16).

Boyer, T.P., Antonov, J.I., Baranova, O.K., Coleman, C., Garcia, H.E., Grodsky, A., Johnson, D.R., Locarnini, R.A., Mishonov, A.V., O'Brien, T.D., Paver, C.R., Reagan, J.R., Seidov, D., Smolyar, I.V., Zweng, M.M., 2013. World ocean database 2013. In: Levit, S., Mishonov, A. (Eds.), NOAA Atlas NESDIS 72: Silver Spring, NOAA, pp. 209.

Brandon, C.M., Woodruff, J.D., Lane, D., Donnelly, J.P., 2013. Tropical cyclone wind speed constraints from resultant storm surge deposition: A 2500 year reconstruction of hurricane activity from St. Marks, FL. Geochemistry, Geophysics, Geosystems 14, 2993–3008.

Brandon, C.M., Woodruff, J.D., Donnelly, J.P., Sullivan, R.M., 2014. How unique was Hurricane Sandy? Sedimentary reconstructions of extreme flooding from New York Harbor. Scientific reports 4, 7366.

Bregy, J.C., Wallace, D.J., Minzoni, R.T., Cruz, V.J., 2018. 2500-year paleotempestological record of intense storms for the Northern Gulf of Mexico, United States. Marine Geology, 396, 26-42.

Brill, D., May, S.M., Engel, M., Reyes, M., Pint, A., Opitz, S., Dierick, M., Gonzalo, L.A., Esser, S., Brückner, H., 2016. Typhoon Haiyan's sedimentary record in coastal environments of the Philippines and its palaeotempestological implications. Natural Hazards and Earth System Sciences Discussions 1–36. doi:10.5194/nhess-2016-224

Brothelande, E., Lénat, J.-F., Normier, A., Bacri, C., Peltier, A., Paris, R., Kelfoun, K., Merle, O., Finizola, A., Garaebiti, E., 2015. Insights into the evolution of the Yenkahe resurgent dome (Siwi caldera, Tanna Island, Vanuatu) inferred from

aerial high-resolution photogrammetry. Journal of Volcanology and Geothermal Research.

Bryant, E., Lee, E., Johnson, D., and Mockett, N., 1987, Calibration of settling tubes for collective particle settling, Journal of Sedimentary Research, v. 57, 784-785.

Buys, J., Spandler, C., Holm, R.J., Richards, S.W., 2014. Remnants of ancient Australia in Vanuatu: Implications for crustal evolution in island arcs and tectonic development of the southwest Pacific. Geology 42, 939–942.

Carney, J.N., MacFarlane, A., 1982. The Evolution of the India-Pacific Plate Boundaries Geological evidence bearing on the Miocene to Recent structural evolution of the New Hebrides arc. Tectonophysics 87, 147–175. doi:10.1016/0040-1951(82)90225-6.

Cita, M.B., Aloisi, G., 2000. Deep-sea tsunami deposits triggered by the explosion of Santorini (3500 y BP), eastern Mediterranean. Sedimentary Geology 135, 181-203.

Coleman, P.J., 1970. Geology of the Solomon and New Hebrides islands, as Part of the Melanesian Re-entrant, Southwest Pacific. Pacific Science 24, 289-314.

Donato, S.V., Reinhardt, E.G., Boyce, J.I., Pilarczyk, J.E., Jupp, B.P., 2009. Particle-size distribution of inferred tsunami deposits in Sur Lagoon, Sultanate of Oman. Marine Geology 257, 54–64.

Donnelly, J.P., Woodruff, J.D., 2007. Intense hurricane activity over the past 5,000 years controlled by El Niño and the West African monsoon. Nature 447, 465–468.

Donnelly, J.P., Hawkes, A.D., Lane, P., MacDonald, D., Shuman, B.N., Toomey, M.R., van Hengstum, P.J., Woodruff, J.D., 2015. Climate forcing of unprecedented intense-hurricane activity in the last 2000 years. Earth's Future 3, 49–65. doi:10.1002/2014EF000274

Dura, T., Engelhart, S.E., Vacchi, M., Horton, B.P., Kopp, R.E., Peltier, W.R., Bradley, S., 2016. The role of Holocene relative sea-level change in preserving records of subduction zone earthquakes. Curr. Clim. Chang. Rep. 2 (3), 86-100.

Ferguson, R.I., Church, M., 2004. A simple universal equation for grain settling velocity. Journal of sedimentary Research 74, 933–937.

Firth, C.W., Handley, H.K., Cronin, S.J., Turner, S.P., 2014. The eruptive history and chemical stratigraphy of a post-caldera, steady-state volcano: Yasur, Vanuatu. Bulletin of Volcanology 76, 1–23.

Folk, R.L., Ward, W.C., 1957. Brazos River bar: a study in the significance of grain size parameters. Journal of Sedimentary Research 27.

Freundt, A., Kuterolf, S., Wehrmann, H., Schmincke, H.U., Strauch, W., 2005. Eruption of the dacite to andesite zoned Meteare Tephra, and associated tsunamis

in Lake Mangua, Nicaragua. Journal of Volcanology and Geothermal Research 149, 103-123.

Fritz, H.M., Blount, C.D., Sokoloski, R., Singleton, J., Fuggle, A., McAdoo, B.G., Moore, A., Grass, C., Tate, B., 2007. Hurricane Katrina storm surge distribution and field observations on the Mississippi Barrier Islands. Estuarine, Coastal and Shelf Science 74, 12-20.

Fritz, H.M., Blount, C.D., Thwin, S., Thu, M.K., Chan, N., 2009. Cyclone Nargis storm surge in Myanmar. Nature Geoscience 2, 448-449. doi: 10.1038/ngeo558.

Gelfenbaum, G., Jaffe, B., 2003. Erosion and sedimentation from the 17 July, 1998 Papua New Guinea tsunami. Pure Appl. Geophys. 160, 1969-1999.

Goff, J. Chagué-Goff, C., Dominey-Howes, D., McAdoo, B., Cronin, S., Bronté-Grapetin, M., Nichol, S., Horrocks, M., Cisternas, M., Lamarche, G., Pelletier, B., Jaffe, B., Dudley, W., 2011. Paleotsunamis in the Pacific Islands. Earth Sci. Rev. 107 (1-2), 141-146.

Greene, H.G., 1984. Geology and Offshore Resources of Vanuatu--Introduction and Summary.

Griffiths, G.M., Salinger, M.J., Leleu, I., 2003. Trends in extreme daily rainfall across the south Pacific and relationship to the South Pacific Convergence Zone. International Journal of Climatology, 23: 847-869. doi: 10.1002/joc.923.

Hawkes, A.D., Bird, M., Cowie, S., Grundy-Warr, C., Grundy-Warr, C., Horton, B.P., Hwai, A.T.S., Law, L., Macgregor, C., Nott, J., Ong, J.E., Rigg, J., Robinson, R., Tan-Mullins, M., Sa, T.T., Yakin, Z., Aik, L.W., 2007. Sediments deposited by the 2004 Indian Ocean Tsunami along the Malaysia-Thailand Peninsula. Marine Geology 242, 169-190.

Hawkes, A.D., Horton, B.P., 2012. Sedimentary record of storm deposits from Hurricane Ike, Galveston and San Luis Islands, Texas. Geomorphology 171, 180–189.

Hill, M.O., Gauch Jr, H.G., 1980. Detrended correspondence analysis: an improved ordination technique. Vegetatio 42(1-3), 47-58.

Horton, B.P., Rossi, V., Hawkes, A.D., 2009. The sedimentary record of the 2005 hurricane season from the Mississippi and Alabama coastlines. Quaternary International 195, 15-30.

Intergovernmental Oceanographic Commission (IOC), 2016. Sea level station monitoring facility. Online: http://www.ioc-sealevelmonitoring.org/list.php (accessed 8.1.16).

Jenner, L., 2015. Pam (Southern Pacific Ocean). NASA. Online: http://www.nasa.gov/content/ goddard/pam-southern-pacific-ocean (accessed 8.9.16).

Joint Typhoon Warning Center (JTWC), 2015. JTWC Southern Hemisphere best track data 2014-2015. Online: http://www.usno.navy.mil/NOOC/nmfc-ph/RSS/jtwc/best_tracks/wpindex.php.

Kelsey, H.M., Engelhart, S.E., Pilarczyk, J.E., Horton, B.P., Rubin, C.M., Daryono, m.R>, Ismail, N., Hawkes, A.D., Bernhardt, C.E., Cahill, N., 2015. Accommodation space, relative sea level, and the archiving of paleo-earthquakes along subduction zones. Geology 43 (8), 675-678.

Kortekaas, S., Dawson, A.G., 2007. Distinguishing tsunami and storm deposits: an example from Martinhal, SW Portugal. Sedimentary Geology 200, 208–221.

Kosciuch, T.J., Pilarczyk, J.E., Hong, I., Fritz, H.M., Horton, B.P., Rarai, A., Harrison, M.J., Jockley, F.R., 2018. Foraminifera reveal a shallow nearshore origin for overwash sediments deposited by Tropical Cyclone Pam in Vanuatu (South Pacific). Marine Geology 396, 171-185.

Liu, K., Fearn, M.L., 1993. Lake-sediment record of late Holocene hurricane activities from coastal Alabama. Geology 21, 793–796.

Liu, K., Fearn, M.L., 2000. Reconstruction of prehistoric landfall frequencies of catastrophic hurricanes in northwestern Florida from lake sediment records. Quaternary Research 54, 238–245.

Meffre, S., Crawford, A.J., 2001. Collision tectonics in the New Hebrides arc (Vanuatu). Island Arc 10, 33–50. doi:10.1046/j.1440-1738.2001.00292.x

Middleton, G.V., 1970. Experimental studies related to the problem of flysch sedimentation. Geol. Assoc. Can. Spec. Pap. 7, 253-272.

New Zealand MetService. TC Pam Summary. Online: http://blogmetservice.com/TC-Pam-Summary (accessed 7.9.16).

Nishijima, K., Mori, N., Yasuda, T., Shimura, T., Gogo, J., Gibson, D., Jockley, F., 2015. DPRI-VMGD joint survey for Cyclone Pam damages, Port-Vila, Vanuatu. Online:http://www.taifu.dpri.kyoto-u.ac.jp/wp-content/uploads/2015/05/DPRI-VMGD-survey-first-report-Final.pdf (accessed 8.10.16).

Nott, J., 2006. Tropical Cyclones and the Evolution of the Sedimentary Coast of Northern Australia. Journal of Coastal Research 22, 49-62.

Nott, J., Smithers, S., Walsh, K., Rhodes, E., 2009. Sand beach ridges record 6000 year history of extreme tropical cyclone activity in northeastern Australia. Quaternary Science Reviews 28, 1511–1520.

Pilarczyk, J.E., Horton, B.P., Soria, J.L.A., Switzer, A.D., Siringan, F., Fritz, H.M., Khan, N.S., Ildefonso, S., Doctor, A.A., Garcia, M.L., 2016. Micropaleontology of the 2013 Typhoon Haiyan overwash sediments from the Leyte Gulf, Philippines. Sedimentary Geology 339, 104-114.

Sambridge, M., Braun, J., McQueen, H., 1995. Geophysical parametrization and interpolation of irregular data using natural neighbours. Geophysical Journal International 122, 837–857.

Shanmugam, G., 2012. Process-sedimentological challenges in distinguishing paleo-tsunami deposits. Nat. Hazards 63, 5-30.

Smith, S. J., Friedrichs, C. T., 2011. Size and settling velocities of cohesive flocs and suspended sediment aggregates in a trailing suction hopper dredge plume. Continental Shelf Research 31(10), S50-S63.

Soria, J.L.A., Switzer, A.D., Villanoy, C.L., Fritz, H.M., Bilgera, P.H.T., Cabrera, O.C., Siringan, F.P., Maria, Y-S.Y., Ramos, R.D., Fernandez, I.Q., 2016. Repeat storm surge disasters of Typhoon Haiyan and its 1897 predecessor in the Philippines. Bulletin of the American Meterological Society 97, 31-48.

Soria, J.L.A., Switzer, A.D., Pilarczyk, J.E., Siringan, F., Li, L., Manglicmot, M., Gallentes, A., Lau, A.A.Y., Cheong, A., Lin, Y., Ling, T.K.W., 2018. Typhoon Haiyan storm surge carried two distinct sediment assemblages on the carbonate coast of Hernani, Samar, central Philippines. Marine Geology, 396, 215-230.

Stewart, R.B., Németh, K., Cronin, S.J., 2010. Is Efate (Vanuatu, SW Pacific) a result of subaerial or submarine eruption? An alternative model for the 1 Ma Efate Pumice Formation. Cent. Eur. J. Geosci. 2, 306–320. doi:10.2478/v10085-010-0020-9

Switzer, A.D., Jones, B.G., 2008. Large-scale washover sedimentation in a freshwater lagoon from the southeast Australian coast: sea-level change, tsunami or exceptionally large storm? The Holocene 18, 787–803.

Syvitski, J.P.M., Asprey, K.W., Clattenburg, D.A., 1991. Principles, design, and calibration of settling tubes, in Syvitski, J.P.M., ed., Principles, methods, and application of particle size analysis: Cambridge, Cambridge University Press, p. 45-63.

Szczuciński, W., 2012. The post-depositional changes of the onshore 2004 tsunami deposits on the Andaman Sea coast of Thailand. Nat. Hazards 60, 115-133.

Taylor, F.W., Frohlich, C., Lecolle, J., Strecker, M., 1987. Analysis of partially emerged corals and reef terraces in the central Vanuatu arc: Comparison of contemporary coseismic and nonseismic with Quaternary vertical movements. Journal of Geophysical Research: Solid Earth 92, 4905–4933.

UNESCO, 2014. International Tsunami Survey Team (ITST) Post-Tsunami Survey Field Guide, UNESCO-IOC Manuals and Guides, 37, 2nd edition. Pp. 114 Paris, France.

Veron, J.E.N., 1990. Checklist of the Hermatypic Corals of Vanuatu. Pac. Sci. 44 (1), 51-70.

Vincent, D.G., 1994. The south Pacific convergence zone (SPCZ): a review. Monthly Weather Review 122, 1949-1970.

Wallace, D.J., Anderson, J.B., 2010. Evidence of similar probability of intense hurricane strikes for the Gulf of Mexico over the late Holocene. Geology 38(6), 511-514.

Wallace, D.J., Woodruff, J.D., Anderson, J.B., Donnelly, J.P., 2014. Palaeohurricane reconstructions from sedimentary archives along the Gulf of Mexico, Caribbean Sea, and western North Atlantic Ocean margins. In: Martini, I.P., Wanless, H.R. (Eds.), Sedimentary Coastal Zones From High to Low Latitudes: Similarities and Differences: Geological Society, London, Special Publications, 388, pp. 481-501.

Whitham, A.G., Sparks, R.S.J., 1986. Pumice. Bulletin of Volcanology 48(4), 209-223.

Williams, H.F.L., 2009. Stratigraphy, sedimentology, and microfossil content of Hurricane Rita storm surge deposits in southwest Louisiana. J. Coast. Res. 25 (4), 1041-1051.

Wirrmann, D., Eagar, S.H., Harper, M.A., Leroy, É., Sémah, A-E., 2011. First insights into mid-Holocene environmental change in central Vanuatu inferred from a terrestrial record from Emaotfer Swamp, Efaté Island. Quaternary Science Reviews 30, 3908-3924.

Woodruff, J.D., Donnelly, J.P., Mohrig, D., Geyer, W.R., 2008. Reconstructing relative flooding intensities responsible for hurricane-induced deposits from Laguna Playa Grande, Vieques, Puerto Rico. Geology 36, 391–394.

Woodruff, J.D., Donnelly, J.P., Okusu, A., 2009. Exploring typhoon variability over the mid-to-late Holocene: evidence of extreme coastal flooding from Kamikoshiki, Japan. Quaternary Science Reviews 28, 1774-1785.

Woodruff, J.D., Kanamaru, K., Kundu, S., Cook, T.L., 2015. Depositional evidence for the Kamikaze typhoons and links to changes in typhoon climatology. Geology 43, 91–94.

World Bank. PDNA Cyclone Pam Vanuatu Report. Online: https://www.gfdrr.org/sites/default/files/publication/PDNA_Cyclone_Pam_Vanuatu_Report.pdf (accessed 7.5.16).

Yates, S.J.K., Lal, A., 2014. EDM Height Traversing Levelling Survey Report, Port Vila, Vanuatu, October 202. Record 2014/31. Geoscience Australia, Canberra.

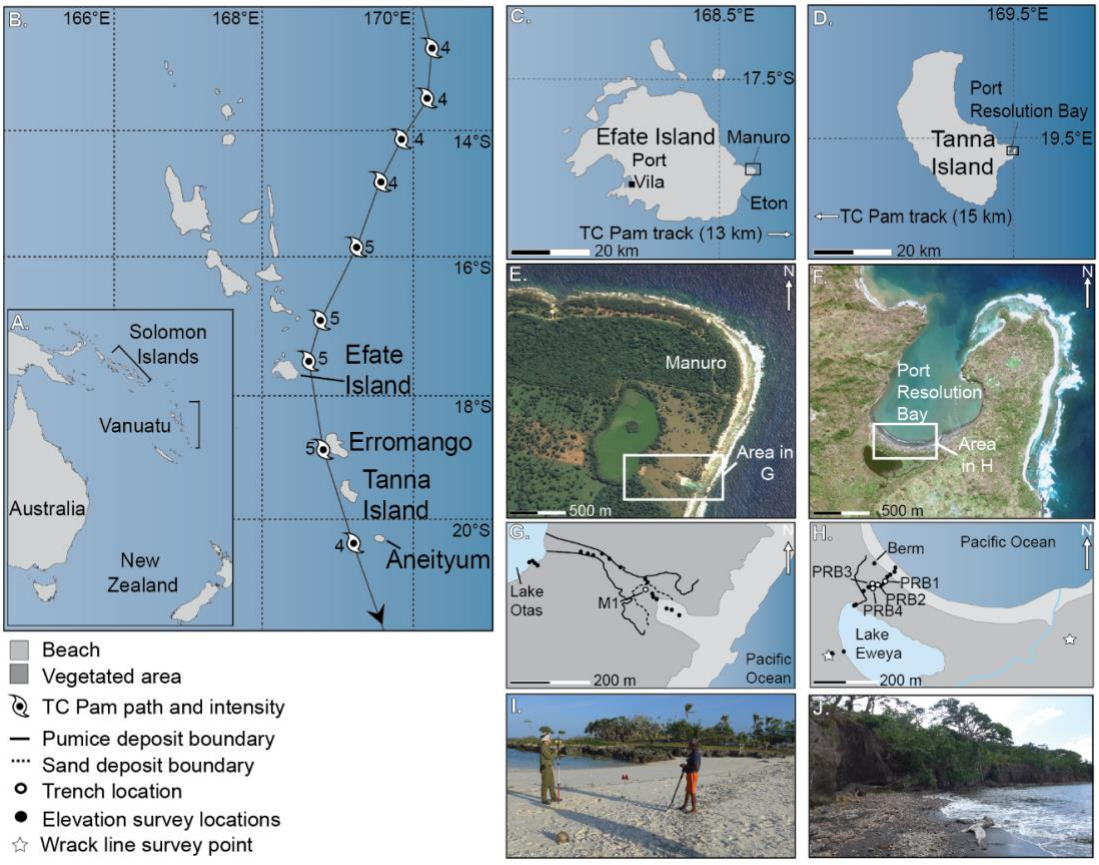

Figure 1. (A) Location map of Vanuatu. (B) TC Pam's track through Vanuatu with location and intensity marked next to tropical cyclone symbol. (C) The island of Efate. (D) The island of Tanna. E: Satellite imagery of Manuro (Map data: Google Earth, 2016). (F) Satellite imagery of Port Resolution Bay (Map data: Google Earth, 2016). (G) Site map of Manuro with major features and transect. (H) Site map of Port Resolution Bay with major features and transect. (I) Photo of the mixed-carbonate beach at Manuro. (J) Photo of the volcaniclastic beach at Port Resolution Bay.

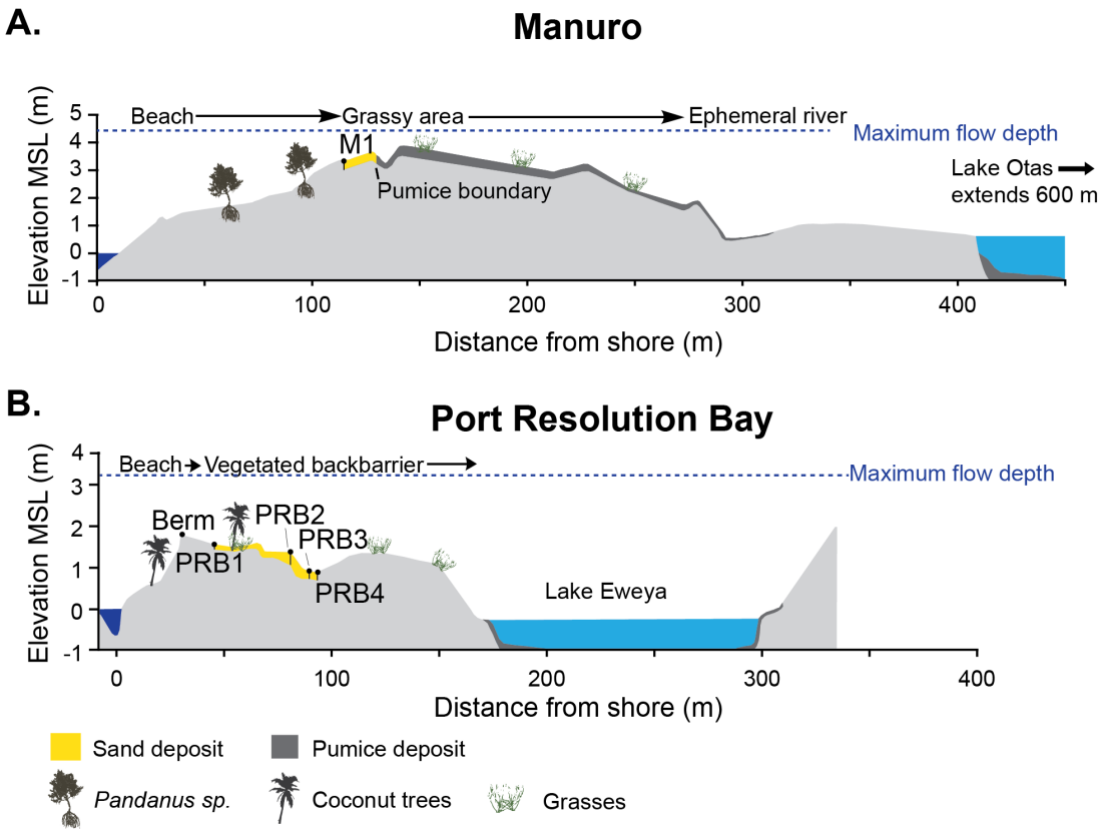

Figure 2. (A) Stratigraphic transect of Manuro and (B) Port Resolution Bay moving in increasing distance inland from shore (m).

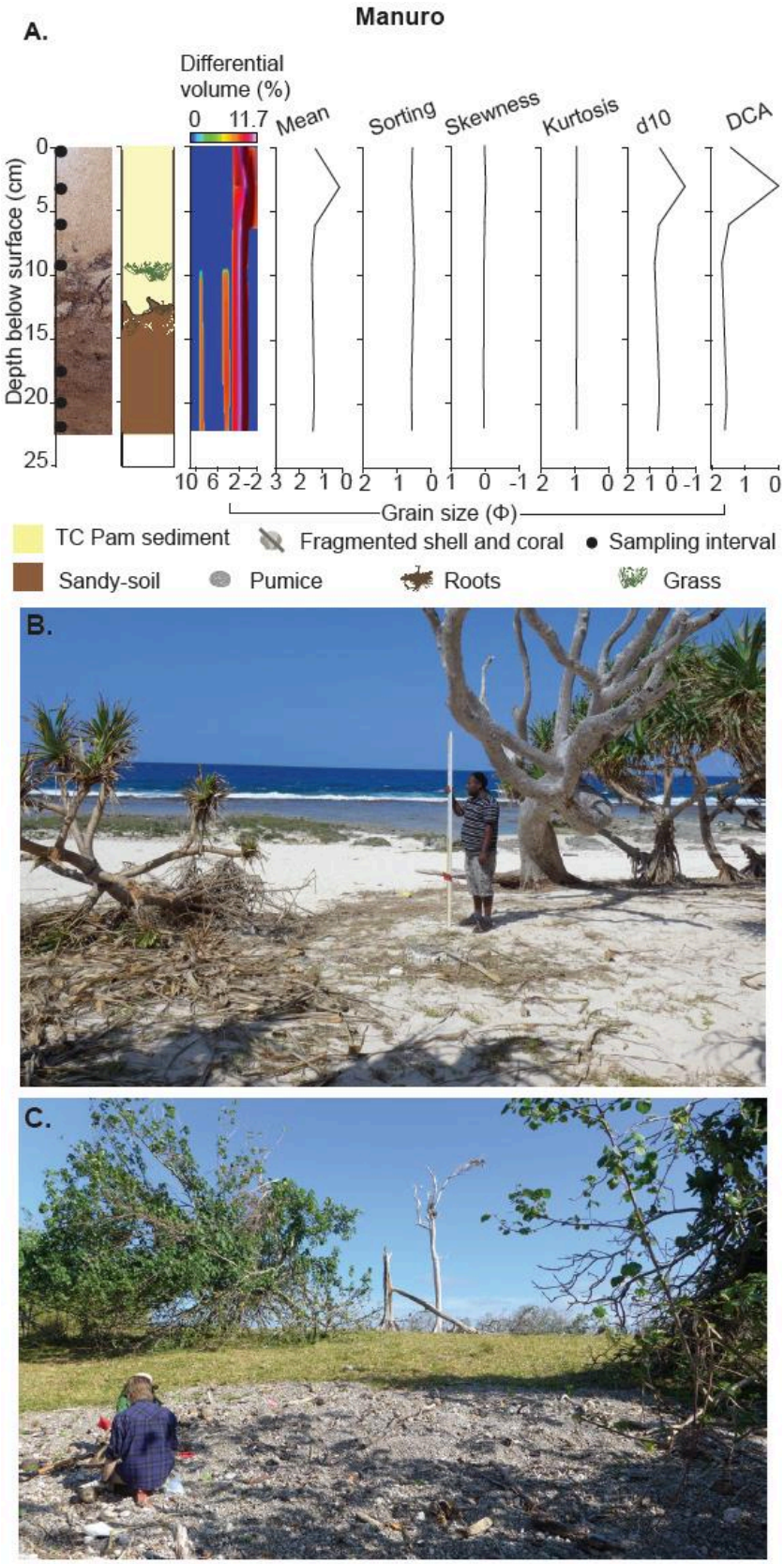

Figure 3. (A) Grain-size distribution for trenches at Manuro. To the right of the photographs of the trenches are a depiction of the stratigraphy, a colored plot displaying grain-size distribution by the total volume of grains of each grain size (ϕ), and grain-size statistics. (B) Photograph of Manuro showing the sand and (C) pumice.

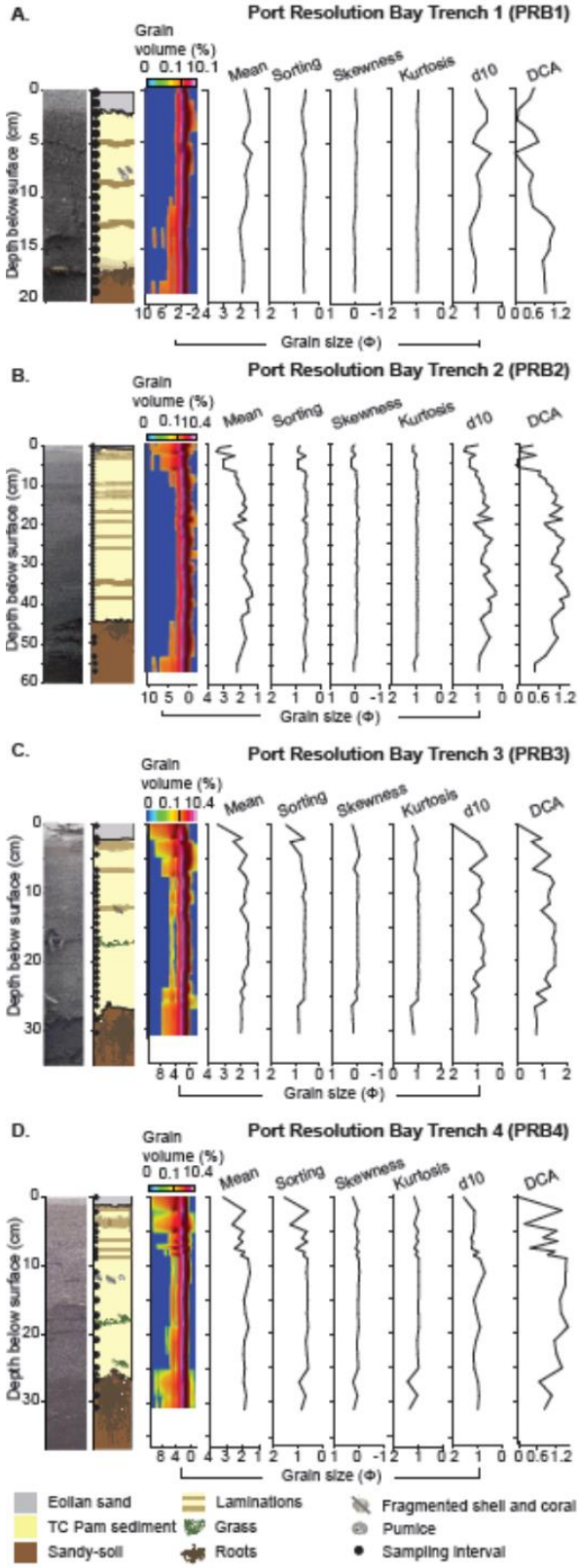

Figure 4. (A-D) Grain-size distribution for trenches at Port Resolution Bay. To the right of the photographs of the trenches are a depiction of the stratigraphy, a colored plot displaying grain-size distribution by the total volume of grains of each grain size (ϕ), and grain-size statistics.

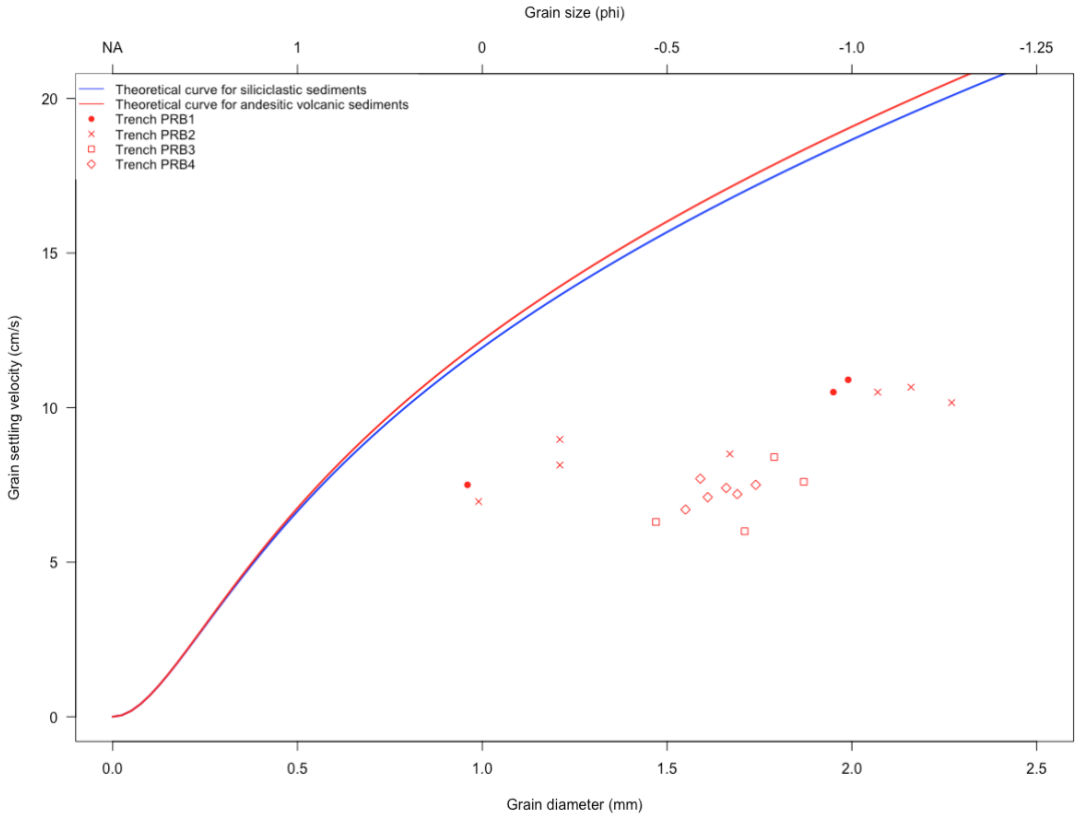

Figure 5. Grain size versus settling velocity. Mean settling velocities measured for andesitic volcaniclastic (red circles) sediments. The vertical error bars indicate 1 SD for settling velocity. The curves are predicted settling velocities for siliciclastic (blue) and andesitic (red) sediments using the equation by Ferguson and Church (2004) for naturally-shaped grains.

TABLE 1. Estimated flow depths (m) using averaged laboratory settling velocities and theoretical settling velocities (Woodruff, 2008)

Trench	Depth	xL (m)	Grain diameter x (cm)	Average Settling Tube w_s (cm/s)	Estimated flow depth (m; average w_s)	Theoretical Settling Velocity w_s (cm/s)	Theoretical flow depth (m; theoretical w_s)
PRB1	2-3 cm	14.9	0.195	10.5	0.63	18.8	0.93
	7-8 cm	14.9	0.199	10.8	0.64	19.0	0.94
	15-16 cm	14.9	0.096	7.46	0.50	11.8	0.68
PRB2	29.5-30.5 cm	50.3	0.167	8.50	1.23	17.1	1.96
	35.5-36.5 cm	50.3	0.227	10.2	1.39	20.5	2.22
	36.5-37.5 cm	50.3	0.216	10.7	1.43	20.0	2.17
	40.5-41.5 cm	50.3	0.121	8.14	1.20	14.0	1.71
	41.5-42.5 cm	50.3	0.207	10.5	1.42	19.4	2.14
	42.5-43.5 cm	50.3	0.121	8.97	1.28	13.9	1.71
	43.5-44.5 cm	50.3	0.099	6.96	1.08	12.1	1.56
PRB3	2-2.5 cm	59.0	0.147	6.31	1.12	15.8	2.07
	18.5-19.5 cm	59.0	0.179	8.44	1.36	17.8	2.24
	20-5-21.5 cm	59.0	0.187	7.59	1.27	18.3	2.28
	24.5-25.5 cm	59.0	0.171	6.04	1.09	17.3	2.20
PRB4	5-6 cm	63.0	0.169	7.20	1.28	17.3	2.29
	17-19 cm	63.0	0.159	7.67	1.34	16.6	2.23
	19-21 cm	63.0	0.166	7.39	1.30	17.1	2.28
	21-23 cm	63.0	0.155	6.72	1.22	16.3	2.21
	23-25 cm	63.0	0.174	7.47	1.31	17.6	2.32
	25-27 cm	63.0	0.161	7.07	1.27	16.7	2.24

TABLE S1. Comparison of laboratory settling velocities with theoretical grain settling velocities

Trench	Depth	Settling tube w_s (cm/s)	Stokes' Law w_s (cm/s)	Dietrich-natural grain w_s (cm/s)	Ferguson and Church-spherical grain w_s (cm/s)	Ferguson and Church-intermediate grain w_s (cm/s)	Ferguson and Church-angular grain w_s (cm/s)
PRB1	2-3 cm	10.45	339.93	18.77	30.24	19.76	17.81
	7-8 cm	10.80	354.05	19.00	30.63	19.99	18.03
	15-16 cm	7.46	83.18	11.84	18.23	12.53	11.08
Average		**9.57**	**259.05**	**16.54**	**26.36**	**17.43**	**15.64**
PRB2	5-6 cm	7.20	257.21	17.26	27.63	18.18	16.35
	17-19 cm	7.67	225.83	16.58	26.45	17.47	15.69
	19-21 cm	7.39	247.19	17.05	27.27	17.96	16.14
	21-23 cm	6.72	214.59	16.32	26.00	17.20	15.43
	23-25 cm	7.47	271.59	17.55	28.13	18.48	16.63
	25-27 cm	7.07	231.56	16.71	26.68	17.61	15.81
Average		**7.25**	**241.33**	**16.91**	**27.03**	**17.82**	**16.01**
PRB3	2-2.5 cm	6.31	192.96	15.78	25.07	16.64	14.91
	18.5-19.5 cm	8.44	286.35	17.84	28.62	18.78	16.90
	20-5-21.5 cm	7.59	312.57	18.31	29.44	19.28	17.36
	24.5-25.5 cm	6.04	261.28	17.35	27.77	18.27	16.43
Average		**7.10**	**263.29**	**17.32**	**27.72**	**18.24**	**16.40**
PRB4	29.5-30.5 cm	8.50	251.17	17.14	27.41	18.05	16.23
	35.5-36.5 cm	10.16	463.59	20.55	33.29	21.61	19.53
	36.5-37.5 cm	10.66	418.52	19.95	32.26	20.99	18.95
	40.5-41.5 cm	8.14	132.38	13.95	21.89	14.73	13.13
	41.5-42.5 cm	10.50	383.13	19.45	31.39	20.46	18.46
	42.5-43.5 cm	8.97	130.77	13.89	21.79	14.67	13.07
	43.5-44.5 cm	6.96	88.38	12.11	18.69	12.81	11.34
Average		**9.13**	**266.85**	**16.72**	**26.67**	**17.62**	**15.82**

TABLE S2. Summary grain size statistics for Manuro trench (TC Pam sediments in bold).

Depth (cm)	Mean (Φ)		Mode (Φ)	Sorting (Φ)		Skewness (Φ)		Kurtosis (Φ)		D10 (Φ)	D50 (Φ)	D90 (Φ)
0-3	**1.29**	**Medium Sand**	**1.23**	**0.56**	**Moderately Well Sorted**	**0.01**	**Symmetrical**	**0.93**	**Mesokurtic**	**0.57**	**1.29**	**2.02**
3-6	**0.23**	**Coarse Sand**	**0.31**	**0.59**	**Moderately Well Sorted**	**-0.03**	**Symmetrical**	**0.94**	**Mesokurtic**	**-0.54**	**0.24**	**0.98**
6-9	**1.32**	**Medium Sand**	**1.23**	**0.54**	**Moderately Well Sorted**	**0.01**	**Symmetrical**	**0.94**	**Mesokurtic**	**0.62**	**1.31**	**2.02**
9-12	**1.45**	**Medium Sand**	**1.42**	**0.51**	**Moderately Well Sorted**	**0.02**	**Symmetrical**	**0.93**	**Mesokurtic**	**0.80**	**1.44**	**2.11**
18-20	1.35	Medium Sand	1.23	0.59	Moderately Well Sorted	0.03	Symmetrical	0.94	Mesokurtic	0.61	1.34	2.13
20-22	1.35	Medium Sand	1.23	0.59	Moderately Well Sorted	0.03	Symmetrical	0.94	Mesokurtic	0.60	1.34	2.12
22-24	1.40	Medium Sand	1.42	0.57	Moderately Well Sorted	0.03	Symmetrical	0.94	Mesokurtic	0.66	1.39	2.15

TABLE S3. Summary grain size statistics for trench PRB1 (TC Pam sediments in bold).

Depth (cm)	Mean (Φ)		Mode (Φ)	Sorting (Φ)		Skewness (Φ)		Kurtosis (Φ)		D10 (Φ)	D50 (Φ)	D90 (Φ)
0-1	1.78	Medium Sand	1.78	0.55	Moderately Well Sorted	0.00	Symmetrical	0.95	Mesokurtic	1.07	1.78	2.50
1-2	1.65	Medium Sand	1.60	0.59	Moderately Well Sorted	-0.01	Symmetrical	0.95	Mesokurtic	0.88	1.65	2.41
2-3	**1.52**	**Medium Sand**	**1.60**	**0.69**	**Moderately Well Sorted**	**-0.06**	**Symmetrical**	**0.98**	**Mesokurtic**	**0.60**	**1.54**	**2.38**
3-4	**1.49**	**Medium Sand**	**1.60**	**0.67**	**Moderately Well Sorted**	**-0.06**	**Symmetrical**	**0.98**	**Mesokurtic**	**0.60**	**1.50**	**2.32**
4-5	**1.76**	**Medium Sand**	**1.78**	**0.59**	**Moderately Well Sorted**	**-0.01**	**Symmetrical**	**0.95**	**Mesokurtic**	**0.99**	**1.76**	**2.51**
5-6	**1.88**	**Medium Sand**	**1.78**	**0.56**	**Moderately Well Sorted**	**0.01**	**Symmetrical**	**0.94**	**Mesokurtic**	**1.16**	**1.88**	**2.60**
6-7	**1.39**	**Medium Sand**	**1.42**	**0.69**	**Moderately Well Sorted**	**-0.04**	**Symmetrical**	**0.96**	**Mesokurtic**	**0.47**	**1.41**	**2.26**
7-8	**1.60**	**Medium Sand**	**1.60**	**0.61**	**Moderately Well Sorted**	**-0.03**	**Symmetrical**	**0.96**	**Mesokurtic**	**0.79**	**1.61**	**2.38**
8-9	**1.76**	**Medium Sand**	**1.78**	**0.57**	**Moderately Well Sorted**	**0.00**	**Symmetrical**	**0.95**	**Mesokurtic**	**1.02**	**1.76**	**2.50**
9-10	**1.66**	**Medium Sand**	**1.60**	**0.58**	**Moderately Well Sorted**	**-0.01**	**Symmetrical**	**0.95**	**Mesokurtic**	**0.90**	**1.66**	**2.40**
10-11	**1.65**	**Medium Sand**	**1.60**	**0.59**	**Moderately Well Sorted**	**0.00**	**Symmetrical**	**0.94**	**Mesokurtic**	**0.88**	**1.66**	**2.42**
11-12	**1.72**	**Medium Sand**	**1.78**	**0.62**	**Moderately Well Sorted**	**-0.01**	**Symmetrical**	**0.96**	**Mesokurtic**	**0.92**	**1.73**	**2.52**
12-13	**1.93**	**Medium Sand**	**1.97**	**0.66**	**Moderately Well Sorted**	**0.04**	**Symmetrical**	**0.98**	**Mesokurtic**	**1.10**	**1.92**	**2.79**
13-14	**2.08**	**Fine Sand**	**1.97**	**0.65**	**Moderately Well Sorted**	**0.07**	**Symmetrical**	**1.00**	**Mesokurtic**	**1.28**	**2.06**	**2.95**
14-15	2.02	Fine Sand	1.97	0.61	Moderately Well Sorted	0.04	Symmetrical	0.97	Mesokurtic	1.25	2.02	2.82
15-16	1.98	Medium Sand	1.97	0.64	Moderately Well Sorted	0.04	Symmetrical	0.98	Mesokurtic	1.18	1.97	2.81
16-17	1.87	Medium Sand	1.78	0.64	Moderately Well Sorted	0.01	Symmetrical	0.96	Mesokurtic	1.06	1.87	2.70
17-18	1.86	Medium Sand	1.78	0.62	Moderately Well Sorted	0.03	Symmetrical	0.97	Mesokurtic	1.08	1.85	2.66
18-19	1.87	Medium Sand	1.78	0.63	Moderately Well Sorted	0.02	Symmetrical	0.96	Mesokurtic	1.07	1.86	2.69
19-20	1.93	Medium Sand	1.97	0.62	Moderately Well Sorted	0.04	Symmetrical	0.98	Mesokurtic	1.15	1.92	2.74

TABLE S4. Summary grain size statistics for trench PRB2 (TC Pam sediments in bold).

Depth (cm)	Mean (Φ)		Mode (Φ)	Sorting (Φ)		Skewness (Φ)		Kurtosis (Φ)		D10 (Φ)	D50 (Φ)	D90 (Φ)
0-0.5	2.06	Fine Sand	1.97	0.88	Moderately Sorted	0.06	Symmetrical	1.11	Mesokurtic	0.99	2.05	3.21
0.5-1.5	**2.53**	**Fine Sand**	**2.34**	**0.93**	**Moderately Sorted**	**0.14**	**Fine Skewed**	**1.12**	**Leptokurtic**	**1.45**	**2.48**	**3.80**
1.5-2.5	**2.64**	**Fine Sand**	**2.52**	**0.96**	**Moderately Sorted**	**0.16**	**Fine Skewed**	**1.14**	**Leptokurtic**	**1.54**	**2.58**	**3.96**
2.5-3.5	**1.92**	**Medium Sand**	**1.97**	**0.65**	**Moderately Well Sorted**	**0.02**	**Symmetrical**	**0.99**	**Mesokurtic**	**1.11**	**1.92**	**2.77**
3.5-4.5	**2.39**	**Fine Sand**	**2.15**	**0.93**	**Moderately Sorted**	**0.20**	**Fine Skewed**	**1.06**	**Mesokurtic**	**1.34**	**2.30**	**3.73**
4.5-5.5	**2.39**	**Fine Sand**	**2.15**	**0.93**	**Moderately Sorted**	**0.20**	**Fine Skewed**	**1.06**	**Mesokurtic**	**1.34**	**2.30**	**3.73**
5.5-6.5	**2.39**	**Fine Sand**	**2.15**	**0.93**	**Moderately Sorted**	**0.20**	**Fine Skewed**	**1.06**	**Mesokurtic**	**1.34**	**2.30**	**3.73**
6.5-7.5	**1.88**	**Medium Sand**	**1.97**	**0.65**	**Moderately Well Sorted**	**0.00**	**Symmetrical**	**0.97**	**Mesokurtic**	**1.03**	**1.88**	**2.72**
7.5-8.5	**1.89**	**Medium Sand**	**1.97**	**0.62**	**Moderately Well Sorted**	**0.00**	**Symmetrical**	**0.96**	**Mesokurtic**	**1.09**	**1.89**	**2.69**
8.5-9.5	**1.79**	**Medium Sand**	**1.78**	**0.65**	**Moderately Well Sorted**	**-0.03**	**Symmetrical**	**0.98**	**Mesokurtic**	**0.94**	**1.80**	**2.61**
9.5-10.5	**1.80**	**Medium Sand**	**1.78**	**0.68**	**Moderately Well Sorted**	**-0.04**	**Symmetrical**	**0.99**	**Mesokurtic**	**0.91**	**1.82**	**2.66**
10.5-11.5	**1.70**	**Medium Sand**	**1.78**	**0.68**	**Moderately Well Sorted**	**-0.06**	**Symmetrical**	**0.97**	**Mesokurtic**	**0.79**	**1.72**	**2.55**
11.5-12.5	**1.62**	**Medium Sand**	**1.60**	**0.61**	**Moderately Well Sorted**	**-0.01**	**Symmetrical**	**0.95**	**Mesokurtic**	**0.83**	**1.62**	**2.40**
12.5-13.5	**1.53**	**Medium Sand**	**1.60**	**0.62**	**Moderately Well Sorted**	**-0.02**	**Symmetrical**	**0.95**	**Mesokurtic**	**0.72**	**1.54**	**2.31**
13.5-14.5	**1.51**	**Medium Sand**	**1.60**	**0.59**	**Moderately Well Sorted**	**-0.01**	**Symmetrical**	**0.95**	**Mesokurtic**	**0.74**	**1.52**	**2.28**
14.5-15.5	**1.60**	**Medium Sand**	**1.60**	**0.62**	**Moderately Well Sorted**	**-0.01**	**Symmetrical**	**0.95**	**Mesokurtic**	**0.80**	**1.61**	**2.40**
15.5-16.5	**1.44**	**Medium Sand**	**1.60**	**0.66**	**Moderately Well Sorted**	**-0.06**	**Symmetrical**	**0.98**	**Mesokurtic**	**0.57**	**1.46**	**2.26**
16.5-17.5	**1.56**	**Medium Sand**	**1.60**	**0.64**	**Moderately Well Sorted**	**-0.04**	**Symmetrical**	**0.96**	**Mesokurtic**	**0.72**	**1.57**	**2.37**
17.5-18.5	**1.77**	**Medium Sand**	**1.78**	**0.61**	**Moderately Well Sorted**	**-0.03**	**Symmetrical**	**0.97**	**Mesokurtic**	**0.97**	**1.78**	**2.54**
18.5-19.5	**1.47**	**Medium Sand**	**1.60**	**0.76**	**Moderately Sorted**	**-0.12**	**Coarse Skewed**	**1.00**	**Mesokurtic**	**0.43**	**1.52**	**2.38**
19.5-20.5	**1.95**	**Medium Sand**	**1.97**	**0.61**	**Moderately Well Sorted**	**-0.05**	**Symmetrical**	**0.98**	**Mesokurtic**	**1.15**	**1.96**	**2.72**
20.5-21.5	**1.83**	**Medium Sand**	**1.97**	**0.62**	**Moderately Well Sorted**	**-0.05**	**Symmetrical**	**0.97**	**Mesokurtic**	**1.00**	**1.84**	**2.60**
21.5-22.5	**1.58**	**Medium Sand**	**1.60**	**0.61**	**Moderately Well Sorted**	**-0.02**	**Symmetrical**	**0.95**	**Mesokurtic**	**0.78**	**1.59**	**2.36**
22.5-23.5	**1.57**	**Medium Sand**	**1.60**	**0.63**	**Moderately Well Sorted**	**-0.04**	**Symmetrical**	**0.97**	**Mesokurtic**	**0.74**	**1.58**	**2.37**
23.5-24.5	**1.38**	**Medium Sand**	**1.42**	**0.71**	**Moderately Sorted**	**-0.05**	**Symmetrical**	**0.96**	**Mesokurtic**	**0.43**	**1.39**	**2.27**
24.5-25.5	**1.46**	**Medium Sand**	**1.60**	**0.68**	**Moderately Well Sorted**	**-0.06**	**Symmetrical**	**0.98**	**Mesokurtic**	**0.55**	**1.48**	**2.30**
25.5-26.5	**1.53**	**Medium Sand**	**1.60**	**0.62**	**Moderately Well Sorted**	**-0.03**	**Symmetrical**	**0.96**	**Mesokurtic**	**0.70**	**1.54**	**2.32**
26.5-27.5	**1.50**	**Medium Sand**	**1.60**	**0.63**	**Moderately Well Sorted**	**-0.03**	**Symmetrical**	**0.95**	**Mesokurtic**	**0.68**	**1.51**	**2.30**
27.5-28.5	**1.60**	**Medium Sand**	**1.60**	**0.61**	**Moderately Well Sorted**	**-0.04**	**Symmetrical**	**0.97**	**Mesokurtic**	**0.80**	**1.62**	**2.38**
28.5-29.5	**1.62**	**Medium Sand**	**1.60**	**0.59**	**Moderately Well Sorted**	**-0.02**	**Symmetrical**	**0.95**	**Mesokurtic**	**0.84**	**1.63**	**2.38**
29.5-30.5	**1.62**	**Medium Sand**	**1.60**	**0.58**	**Moderately Well Sorted**	**-0.01**	**Symmetrical**	**0.95**	**Mesokurtic**	**0.86**	**1.62**	**2.37**
30.5-31.5	**1.51**	**Medium Sand**	**1.60**	**0.67**	**Moderately Well Sorted**	**-0.06**	**Symmetrical**	**0.98**	**Mesokurtic**	**0.62**	**1.53**	**2.35**
31.5-32.5	**1.44**	**Medium Sand**	**1.60**	**0.70**	**Moderately Well Sorted**	**-0.05**	**Symmetrical**	**0.96**	**Mesokurtic**	**0.51**	**1.46**	**2.32**
32.5-33.5	**1.55**	**Medium Sand**	**1.60**	**0.61**	**Moderately Well Sorted**	**-0.02**	**Symmetrical**	**0.96**	**Mesokurtic**	**0.75**	**1.56**	**2.33**
33.5-34.5	**1.47**	**Medium Sand**	**1.60**	**0.63**	**Moderately Well Sorted**	**-0.03**	**Symmetrical**	**0.95**	**Mesokurtic**	**0.64**	**1.48**	**2.27**
34.5-35.5	**1.37**	**Medium Sand**	**1.42**	**0.63**	**Moderately Well Sorted**	**-0.02**	**Symmetrical**	**0.96**	**Mesokurtic**	**0.54**	**1.38**	**2.18**
35.5-36.5	**1.29**	**Medium Sand**	**1.42**	**0.68**	**Moderately Well Sorted**	**-0.03**	**Symmetrical**	**0.95**	**Mesokurtic**	**0.40**	**1.30**	**2.15**
36.5-37.5	**1.24**	**Medium Sand**	**1.23**	**0.72**	**Moderately Sorted**	**-0.04**	**Symmetrical**	**0.95**	**Mesokurtic**	**0.29**	**1.26**	**2.15**
37.5-38.5	**1.21**	**Medium Sand**	**1.23**	**0.70**	**Moderately Well Sorted**	**-0.03**	**Symmetrical**	**0.95**	**Mesokurtic**	**0.29**	**1.22**	**2.10**
38.5-39.5	**1.45**	**Medium Sand**	**1.42**	**0.64**	**Moderately Well Sorted**	**-0.02**	**Symmetrical**	**0.95**	**Mesokurtic**	**0.61**	**1.46**	**2.27**
39.5-40.5	**1.40**	**Medium Sand**	**1.42**	**0.69**	**Moderately Well Sorted**	**-0.06**	**Symmetrical**	**0.97**	**Mesokurtic**	**0.47**	**1.42**	**2.26**
40.541.5	**1.36**	**Medium Sand**	**1.42**	**0.66**	**Moderately Well Sorted**	**-0.05**	**Symmetrical**	**0.96**	**Mesokurtic**	**0.49**	**1.38**	**2.19**
41.5-42.5	**1.36**	**Medium Sand**	**1.42**	**0.66**	**Moderately Well Sorted**	**-0.02**	**Symmetrical**	**0.94**	**Mesokurtic**	**0.50**	**1.37**	**2.20**
42.5-43.5	**1.61**	**Medium Sand**	**1.60**	**0.67**	**Moderately Well Sorted**	**-0.03**	**Symmetrical**	**0.96**	**Mesokurtic**	**0.73**	**1.62**	**2.47**
43.5-44.5	**1.65**	**Medium Sand**	**1.60**	**0.59**	**Moderately Well Sorted**	**-0.02**	**Symmetrical**	**0.95**	**Mesokurtic**	**0.88**	**1.66**	**2.40**
47-48	1.52	Medium Sand	1.60	0.68	Moderately Well Sorted	-0.03	Symmetrical	0.96	Mesokurtic	0.63	1.53	2.39
48-49	1.46	Medium Sand	1.60	0.71	Moderately Sorted	-0.05	Symmetrical	0.98	Mesokurtic	0.51	1.48	2.36
52.5-54.5	1.71	Medium Sand	1.78	0.62	Moderately Well Sorted	0.00	Symmetrical	0.96	Mesokurtic	0.91	1.71	2.52
54.5-56.5	1.82	Medium Sand	1.78	0.74	Moderately Sorted	0.10	Fine Skewed	1.09	Mesokurtic	0.94	1.80	2.78
56.5-58.6	1.81	Medium Sand	1.78	0.71	Moderately Sorted	0.08	Symmetrical	1.05	Mesokurtic	0.95	1.79	2.75

TABLE S5. Summary grain size statistics for trench PRB3 (TC Pam sediments in bold).

Depth (cm)	Mean (Φ)		Mode (Φ)	Sorting (Φ)		Skewness (Φ)		Kurtosis (Φ)		D10 (Φ)	D50 (Φ)	D90 (Φ)
0-2	3.46	Very Fine Sand	3.26	1.38	Poorly Sorted	0.20	Fine Skewed	1.22	Leptokurtic	1.97	3.39	5.36
2-2.5	**1.97**	**Medium Sand**	**1.97**	**0.63**	**Moderately Well Sorted**	**0.03**	**Symmetrical**	**0.98**	**Mesokurtic**	**1.17**	**1.97**	**2.80**
2.5-4.5	**2.46**	**Fine Sand**	**2.52**	**1.20**	**Poorly Sorted**	**0.02**	**Symmetrical**	**1.09**	**Mesokurtic**	**0.95**	**2.46**	**3.99**
4.5-6.5	**1.66**	**Medium Sand**	**1.78**	**0.77**	**Moderately Sorted**	**-0.10**	**Symmetrical**	**1.04**	**Mesokurtic**	**0.61**	**1.69**	**2.59**
6.5-7.5	**2.14**	**Fine Sand**	**1.97**	**0.72**	**Moderately Sorted**	**0.13**	**Fine Skewed**	**1.14**	**Leptokurtic**	**1.30**	**2.11**	**3.08**
7.5-8.5	**1.74**	**Medium Sand**	**1.78**	**0.65**	**Moderately Well Sorted**	**-0.03**	**Symmetrical**	**0.98**	**Mesokurtic**	**0.90**	**1.75**	**2.57**
8.5-9.5	**1.59**	**Medium Sand**	**1.60**	**0.62**	**Moderately Well Sorted**	**-0.01**	**Symmetrical**	**0.95**	**Mesokurtic**	**0.78**	**1.59**	**2.38**
9.5-10.5	**1.73**	**Medium Sand**	**1.78**	**0.62**	**Moderately Well Sorted**	**-0.01**	**Symmetrical**	**0.96**	**Mesokurtic**	**0.94**	**1.74**	**2.53**
10.5-11.5	**1.80**	**Medium Sand**	**1.78**	**0.69**	**Moderately Well Sorted**	**-0.04**	**Symmetrical**	**1.00**	**Mesokurtic**	**0.88**	**1.81**	**2.67**
11.5-12.5	**1.74**	**Medium Sand**	**1.78**	**0.60**	**Moderately Well Sorted**	**0.00**	**Symmetrical**	**0.95**	**Mesokurtic**	**0.96**	**1.74**	**2.50**
12.5-13.5	**2.04**	**Fine Sand**	**1.97**	**0.60**	**Moderately Well Sorted**	**0.01**	**Symmetrical**	**0.97**	**Mesokurtic**	**1.27**	**2.04**	**2.81**
13.5-14.5	**1.79**	**Medium Sand**	**1.78**	**0.61**	**Moderately Well Sorted**	**-0.02**	**Symmetrical**	**0.95**	**Mesokurtic**	**1.00**	**1.80**	**2.57**
14.5-15.5	**1.57**	**Medium Sand**	**1.60**	**0.61**	**Moderately Well Sorted**	**-0.02**	**Symmetrical**	**0.96**	**Mesokurtic**	**0.78**	**1.58**	**2.35**
15.5-16.5	**1.58**	**Medium Sand**	**1.60**	**0.61**	**Moderately Well Sorted**	**-0.02**	**Symmetrical**	**0.96**	**Mesokurtic**	**0.78**	**1.58**	**2.36**
16.5-17.5	**1.66**	**Medium Sand**	**1.60**	**0.60**	**Moderately Well Sorted**	**-0.02**	**Symmetrical**	**0.95**	**Mesokurtic**	**0.87**	**1.66**	**2.43**
17.5-18.5	**1.56**	**Medium Sand**	**1.60**	**0.62**	**Moderately Well Sorted**	**-0.03**	**Symmetrical**	**0.96**	**Mesokurtic**	**0.75**	**1.57**	**2.36**
18.5-19.5	**1.54**	**Medium Sand**	**1.60**	**0.64**	**Moderately Well Sorted**	**-0.03**	**Symmetrical**	**0.96**	**Mesokurtic**	**0.70**	**1.55**	**2.35**
19.5-20.5	**1.59**	**Medium Sand**	**1.60**	**0.61**	**Moderately Well Sorted**	**-0.02**	**Symmetrical**	**0.95**	**Mesokurtic**	**0.79**	**1.60**	**2.38**
20.5-21.5	**1.57**	**Medium Sand**	**1.60**	**0.65**	**Moderately Well Sorted**	**-0.04**	**Symmetrical**	**0.97**	**Mesokurtic**	**0.71**	**1.58**	**2.39**
21.5-22.5	**1.81**	**Medium Sand**	**1.78**	**0.60**	**Moderately Well Sorted**	**-0.01**	**Symmetrical**	**0.95**	**Mesokurtic**	**1.03**	**1.81**	**2.58**
22.5-23.5	**1.90**	**Medium Sand**	**1.97**	**0.59**	**Moderately Well Sorted**	**0.00**	**Symmetrical**	**0.96**	**Mesokurtic**	**1.14**	**1.90**	**2.66**
23.5-24.5	**1.76**	**Medium Sand**	**1.78**	**0.64**	**Moderately Well Sorted**	**-0.04**	**Symmetrical**	**0.97**	**Mesokurtic**	**0.92**	**1.77**	**2.57**
24.5-25.5	**2.03**	**Fine Sand**	**1.97**	**0.64**	**Moderately Well Sorted**	**0.06**	**Symmetrical**	**1.01**	**Mesokurtic**	**1.23**	**2.02**	**2.88**
25.5-26.5	**1.86**	**Medium Sand**	**1.97**	**0.63**	**Moderately Well Sorted**	**-0.01**	**Symmetrical**	**0.98**	**Mesokurtic**	**1.04**	**1.87**	**2.67**
26.5-28.5	2.01	Fine Sand	1.78	0.89	Moderately Sorted	0.21	Fine Skewed	1.28	Leptokurtic	1.06	1.95	3.21
28.5-30.5	1.96	Medium Sand	1.78	0.86	Moderately Sorted	0.17	Fine Skewed	1.22	Leptokurtic	1.00	1.92	3.10
30.5-32.5	2.00	Fine Sand	1.78	0.85	Moderately Sorted	0.16	Fine Skewed	1.17	Leptokurtic	1.05	1.96	3.14

TABLE S6. Summary grain size statistics for trench PRB4 (TC Pam sediments in bold).

Depth (cm)	Mean (Φ)		Mode (Φ)	Sorting (Φ)		Skewness (Φ)		Kurtosis (Φ)		D10 (Φ)	D50 (Φ)	D90 (Φ)
0-2	3.23	Very Fine Sand	2.34	1.55	Poorly Sorted	0.23	Fine Skewed	1.14	Leptokurtic	1.59	3.11	5.46
2-4	**1.91**	**Medium Sand**	**1.97**	**0.60**	**Moderately Well Sorted**	**0.02**	**Symmetrical**	**0.96**	**Mesokurtic**	**1.15**	**1.91**	**2.69**
4-5	**2.67**	**Fine Sand**	**2.34**	**1.31**	**Poorly Sorted**	**0.15**	**Fine Skewed**	**1.14**	**Leptokurtic**	**1.17**	**2.58**	**4.42**
5-6	**2.00**	**Fine Sand**	**1.97**	**0.65**	**Moderately Well Sorted**	**0.03**	**Symmetrical**	**0.98**	**Mesokurtic**	**1.18**	**2.00**	**2.85**
6-6.5	**2.30**	**Fine Sand**	**2.15**	**0.83**	**Moderately Sorted**	**0.06**	**Symmetrical**	**1.06**	**Mesokurtic**	**1.28**	**2.28**	**3.39**
6.5-7.5	**2.04**	**Fine Sand**	**1.97**	**0.64**	**Moderately Well Sorted**	**0.02**	**Symmetrical**	**0.98**	**Mesokurtic**	**1.23**	**2.04**	**2.87**
7.5-8	**2.52**	**Fine Sand**	**2.34**	**1.06**	**Poorly Sorted**	**0.11**	**Fine Skewed**	**1.13**	**Leptokurtic**	**1.27**	**2.47**	**3.95**
8-8.5	**1.93**	**Medium Sand**	**1.97**	**0.73**	**Moderately Sorted**	**0.00**	**Symmetrical**	**1.01**	**Mesokurtic**	**0.99**	**1.93**	**2.87**
8.5-9	**2.13**	**Fine Sand**	**2.15**	**0.78**	**Moderately Sorted**	**0.08**	**Symmetrical**	**1.08**	**Mesokurtic**	**1.19**	**2.12**	**3.15**
9-11	**1.72**	**Medium Sand**	**1.78**	**0.61**	**Moderately Well Sorted**	**0.00**	**Symmetrical**	**0.96**	**Mesokurtic**	**0.93**	**1.72**	**2.50**
11-13	**1.59**	**Medium Sand**	**1.60**	**0.65**	**Moderately Well Sorted**	**-0.03**	**Symmetrical**	**0.96**	**Mesokurtic**	**0.74**	**1.60**	**2.42**
13-15	**1.76**	**Medium Sand**	**1.78**	**0.61**	**Moderately Well Sorted**	**0.00**	**Symmetrical**	**0.96**	**Mesokurtic**	**0.98**	**1.76**	**2.55**
15-17	**1.96**	**Medium Sand**	**1.97**	**0.61**	**Moderately Well Sorted**	**0.01**	**Symmetrical**	**0.97**	**Mesokurtic**	**1.18**	**1.96**	**2.75**
17-19	**1.87**	**Medium Sand**	**1.78**	**0.63**	**Moderately Well Sorted**	**0.02**	**Symmetrical**	**0.97**	**Mesokurtic**	**1.07**	**1.87**	**2.70**
19-21	**1.69**	**Medium Sand**	**1.78**	**0.59**	**Moderately Well Sorted**	**0.00**	**Symmetrical**	**0.95**	**Mesokurtic**	**0.93**	**1.69**	**2.45**
21-23	**1.94**	**Medium Sand**	**1.97**	**0.68**	**Moderately Well Sorted**	**0.06**	**Symmetrical**	**1.03**	**Mesokurtic**	**1.10**	**1.93**	**2.84**
23-25	**1.99**	**Medium Sand**	**1.97**	**0.63**	**Moderately Well Sorted**	**0.05**	**Symmetrical**	**1.00**	**Mesokurtic**	**1.20**	**1.98**	**2.82**
25-27	**1.92**	**Medium Sand**	**1.97**	**0.59**	**Moderately Well Sorted**	**0.01**	**Symmetrical**	**0.96**	**Mesokurtic**	**1.16**	**1.92**	**2.69**
27-29	1.98	Medium Sand	1.78	0.95	Moderately Sorted	0.23	Fine Skewed	1.41	Leptokurtic	1.01	1.93	3.21
29-31	1.83	Medium Sand	1.78	0.69	Moderately Well Sorted	0.04	Symmetrical	1.02	Mesokurtic	0.96	1.82	2.73
31-33	1.93	Medium Sand	1.78	0.86	Moderately Sorted	0.19	Fine Skewed	1.33	Leptokurtic	1.02	1.90	3.00

Chapter 2: Diatoms zones across intertidal environments of Willapa Bay, Washington, USA: implications for sea-level reconstructions

Abstract

We described and quantified inter- and intra-site variability in diatom distributions along shore-perpendicular transects from tidal flat to salt marsh and forested upland of Willapa Bay, Washington. We conducted diatom and environmental (elevation, grain-size, total organic carbon (TOC), porewater salinity, and nutrient concentrations) analyses from three tidal marshes: Bone River, Niawiakum River, and Naselle River. The modern training set consisted of 367 diatoms species across 94 genera that captures the range of diatoms found in marine, brackish and freshwater environments. Multivariate analyses (hierarchical clustering and ordination) of the training set identified floral zones at each tidal marsh with differing environmental controls. Vertical zonation of diatoms was illustrated at Bone River Transect 1 and the Niawiakum River. Three floral zones were identified at Bone River Transect 1 with elevation (35% of variance) and TOC (14% of variance) as major environmental controls. Similarly, three floral zones were identified at the Niawiakum River Transect with elevation (28% of variance) and salinity (14% of variance) as the major environmental controls. In contrast, vertical zonation was absent at the Naselle River Transect, which had two floral zones with salinity (21% of variance) as the major environmental control. The combined regional training set also did not display a vertical zonation. Four floral zones were identified with salinity (15% of variance) and site (7% of variance) as the major environmental controls. An intra-site comparison of two transects at Bone River show separation based on transect despite overlapping elevation. In the absence of a well-defined relationship with elevation due to the localized nature of assemblages, our results suggest that alternative methods, such as

grouping species based on similarities in abundance and distribution, must be sought to address limitations in diatom-based, relative sea-level reconstructions.

1. Introduction

Diatoms are photosynthetic algae that are widely applied in paleoenvironmental reconstructions (e.g., Birks et al., 1990; Fritz et al., 1991; Battarbee et al., 2002), because they are abundant in marine, coastal, lacustrine, and freshwater environments (e.g., Conger, 1951; Admiraal, 1984; Palmer and Abbott, 1986). The siliceous composition of diatom valves aid in their preservation and identification in sediments long after their burial (Admiraal, 1984; Palmer and Abbott, 1986; Round et al., 1990; Hemphill-Haley, 1996). Diatom species preferences for distinct environments has led to the establishment of multiple paleoenvironmental classification systems based on salinity, substrate, and elevation with respect to the tidal frame (e.g., Hustedt, 1937, 1939, 1953, 1957; Denys, 1991, 1992; Vos and De Wolf, 1993; Zong and Horton, 1998). Furthermore, the short cell cycle of diatoms allows for the rapid colonization of new species in response to sudden environmental change (Oemke and Burton, 1986; Denys, 1991; Vos and De Wolf, 1993; Horton et al., 2017).

The salinity preferences of modern diatom assemblages serve as an analogue from which fossil diatom assemblages can be used to reconstruct relative sea-level (RSL) change (Haggart, 1986; Shennan et al., 1996; Zong and Horton, 1999; Sawai et al., 2004a). Across the intertidal zone, diatom assemblages may vary to reflect the decrease in salinity with increasing elevation, resulting in a vertical zonation of diatom assemblages with respect to the tidal frame (e.g., Hemphill-Haley, 1995b; Sherrod, 1999; Horton et al., 2006, 2007; Sawai et al., 2016). Diatoms have been applied to estimate RSL rise from earthquakes in the Pacific Northwest of North America (e.g., Darienzo and Peterson, 1990; Shennan et al., 1994; Nelson and Kashima, 1993; Hemphill-Haley, 1995a; Atwater and Hemphill-Haley, 1997) because they are

preserved in fresh, brackish, and marine environments (e.g., Hemphill-Haley, 1995b; Sawai et al., 2016). However, quantitative diatom-based estimates of RSL change from earthquakes have been hampered by site-specific diversity of diatom assemblages, an absence of a well-defined relationship with elevation, and no matching analogues (e.g., Nelson and Kashima, 1993; Nelson et al., 2008; Sawai et al., 2016).

Here, we describe and quantify inter- and intra-site variability in diatom distributions along shore-perpendicular transects from tidal flats to salt marshes and forested upland of Willapa Bay, Washington. We collected samples for diatom and environmental analysis (elevation, grain-size, total organic carbon (TOC), porewater salinity, and nutrient concentrations) from three tidal marshes located in Willapa Bay: (1) the Bone River; (2) the Niawiakum River; (3) and the Naselle River. Hierarchical clustering and ordination show inter- and intra-site variability as diatom zonation displayed differing responses to environmental variables. We conclude by examining the implications of inter- and intra-site variability in diatom-based RSL reconstructions.

2. Study Area

Willapa Bay has been a focus of paleoseismological studies seeking to infer past earthquake magnitudes through estimates of RSL change for over 20 years (e.g., Hemphill-Haley, 1995a; Atwater and Hemphill-Haley, 1997; Sabean, 2004). For example, Hemphill-Haley (1995a) and Atwater and Hemphill-Haley (1997) produced a 3500-yr record of six buried soils correlated with earthquake RSL rise using diatom biostratigraphy. Hemphill-Haley (1995b) collected 16 modern diatom samples from two transects along the Niawiakum River (Fig 1d): a lower Niawiakum Transect (ranging from the channel floor to the high marsh-forested upland transition) and an upper Niawiakum Transect (ranging from the channel floor to the highest point of a

brackish marsh). Sawai et al. (2016) analyzed 12 samples throughout the high marsh from the upper reaches of the Niawiakum River (Fig 1d).

Willapa Bay is an estuary located in southwestern Washington, immediately north of the mouth of the Columbia River (Fig 1). It is a drowned-river valley estuarine system (Emmett et al., 2000) formed from the flooding of river valleys as a result of RSL rise after the Last Glacial Maximum ~26 ka (e.g., Engelhart et al., 2015). Sediment from the Columbia River produced a 26-km long barrier spit that protects a portion of Willapa Bay from the Pacific Ocean (Emmett et al., 2000). Willapa Bay has experienced minimal human and industrial disturbance because the majority of the area is nationally or state-protected wetlands (Emmett et al., 2000).

The climate at Willapa Bay is temperate. We sampled in May 2015 during which the average daily temperature (High 16.8 °C Low 8.2 °C) matched historical average temperatures for May (High 17.1 °C, Low 5.4 °C; NCDC, 2019). Mean daily precipitation in May 2015 was 298 mm which is similar to the historical mean of 323 mm in May (NCDC, 2019).

Our study locations consist of four shore-perpendicular transects from three tidal marshes where tides are mixed semidiurnal (Fig 1c-e). At the Bone River and the Niawiakum River, the Great Diurnal range (difference of mean higher high water and mean lower low water) is 2.8 m (NOAA, 2019). At the Naselle River in southern Willapa Bay, the Great Diurnal range is 3.3 m (NOAA, 2019). Nearly half of the surface area of the estuary is in the intertidal zone, resulting in tidal exchange having a more significant impact than freshwater input from rivers on the variations in salinity within the bay (e.g., Roegner et al., 2002; Banas and Hickey 2005). Bathymetry of Willapa

Bay shows three deeper river channels (> 5 m deep) surrounded by an extensive tidal flat (Fig 1b).

The vegetation at Willapa Bay displays intertidal zonation with flora zones separated into the tidal flat, low marsh and high marsh (Hemphill-Haley, 1995a, b; Atwater and Hemphill-Haley, 1997; Cooke, 1997). The tidal flat contains a lack of vegetation, with only sparse amounts of *Zostera sp*. The low marsh (below mean high water) is characterized by the colonization of *Glaux maritima, Jaumea carnosa, Salicornia virginica, Spartina alterniflora,* and *Triglochin maritima*. The high marsh is delineated by the appearance of *Carex lyngbei, Deschampsia caespitosa, Distichlis spicata*, *Juncus balticus, Potentilla pacifica*. The forested upland contains trees such as *Picea sitchensis* and *Pyrus fusca*.

3. Methods

3.1 Field sampling and elevation measurement

We sampled a total of 67 stations along four shore perpendicular transects from three tidal marshes in Willapa Bay to compare inter-site variability within the same estuary and intra-site variability between two transects at Bone River (Fig 1c-e). Sampling along each transect was done at approximately 10-20 cm vertical increments, ranging from the tidal flat to forested upland. We collected surface sediment for diatom, grain-size, TOC, porewater salinity, and nutrient concentration analyses. A water sample was collected at the Bone River, Niawiakum River, and Naselle River for nutrient analysis of dissolved inorganics (NO_3^-/NO_2^-, NH_4^+, PO_4^{3-}, and SiO_4). We noted the modern vegetation cover of our sampling stations using Cooke (1997) as a reference guide. Modern samples were kept refrigerated until transportation to the laboratory.

To determine the elevation of the sampling stations, we measured elevation using a Real Time Kinematic-Global Positioning System (RTK-GPS) and total station. Elevations were surveyed to geodetic benchmarks and referenced to the North American vertical datum (NAVD88). We used VDatum transformation software to tie measured elevation to mean tide level (MTL; NOAA, Accessed 2019). We converted our measured elevations to a standard water level index (SWLI) to allow for the comparison of sites with differing tidal ranges (Horton et al., 1999; Horton and Edwards, 2006). We calculated the elevation of each sampling station (h_n) to its SWLI value ($SWLI_n$) following Horton et al. (1999):

$$SWLI_n = \frac{100(h_n - h_{MTL})}{h_{MHHW} - h_{MTL}} + 100$$

where n is the sample, h_{MTL} is the elevation of MTL, and h_{MHHW} is the elevation of mean higher high water (MHHW). The resulting SWLI values are relative to the same datum where MTL is 100 and MHHW is 200.

3.2 Diatom analysis

Surface sediment samples were mixed to average seasonal effects, and a subsample was selected. In these intertidal environments, the surface diatom assemblages at any sampling points are likely to be a mixture of locally produced taxa and transported taxa (Zong and Horton, 1999). However, this is not a problem since this study assumes that a mixture of allochthonous and autochthonous diatom valves would occur in sediments that accumulated in the past (Zong, 1997). Therefore, in this study, no attempt is made to separate the allochthonous component from the diatom assemblages.

We prepared diatoms for analysis following the methods of Palmer and Abbott (1986). In the laboratory, disposable plastic syringes removed 1 cm^3 of sediment from each sample for diatom analysis. The sediment was placed in a 25 mL plastic Falcon tube with 30% concentration H_2O_2 until no organic material remained in the sample. We dripped, dried, and mounted the diatoms onto a glass slide using Naphrax. For each sample, 400 valves were counted using light microscopy under oil immersion at 1000x magnification with abundance calculated as a percentage of total diatom valves counted. Diatoms were identified to species level using the references of Krammer and Lange-Bertalot (1986, 1988, 1991a, b), and Witkowski et al. (2001).

3.3 Environmental analysis

In addition to measuring the elevation at each sampling station, we analyzed four environmental variables from the top 2 mm of surface sediment: grain-size, TOC, porewater salinity, and nutrient concentrations to characterize the relationship between diatom assemblages and environmental variables. Studies on the distribution of diatom species and assemblages in tidal wetlands of the Pacific Northwest have shown a strong relationship with elevation as a factor of tidal exposure (e.g., Hemphill-Haley, 1995b; Nelson and Kashima, 1993), substrate (e.g., Amspoker and McIntire, 1978; Sawai et al., 2016), and salinity (e.g., McIntire, 1978; Sherrod, 1999). We explore the influence of nutrient concentration, which has been shown to affect diatom species composition (e.g., Underwood et al., 1998; Snoeijs and Weckström, 2010), on the inter-site variability of diatoms at Willapa Bay.

We measured the grain size of each sample by placing sediment from each station in a 25 mL plastic Falcon tube and removing organic matter using 30% concentration H_2O_2 (Donato et al., 2009). We measured grain size using a Malvern Mastersizer 3000 laser

particle-size analyzer (Sperazza et al., 2004). We use the percentage of mud as the indicator for substrate.

Bulk sedimentary organic matter (SOM) for TOC_{SOM} composition was analyzed at the University of North Carolina-Wilmington following the methods of O'Donnell (2017). The samples were dried at 50° C for 24 hours prior to being ground with a mortar and pestle. Bulk values are reported relative to the Vienna Pee Dee Belemnite scale using L-glutamic acid (USGS40, USGS41, and USGS41a). We calculated the percent TOC by using the known weight of each sample, quantity of C in the L-glutamic acid standards, and the relative production of CO_2 after combustion.

We determined porewater salinity using a calibrated refractometer (Sherrod, 1999; Sawai et al., 2016). We centrifuged the samples to extract porewater salinity. When there was no porewater present, 5 mL of deionized water was added to samples before centrifuging and measurement.

We collected riverine water samples from the Bone River, Niawiakum River, and Naselle River to compare the nutrient concentration of dissolved inorganics at each transect (Fig 1c-e). Each sample was collected into a 25 mL Falcon tube with a syringe and filtered through a GF/F filter on site. Samples were frozen for transportation to the laboratory. Analyses were conducted by the Nutrient Analysis Laboratory at Rutgers University using a Lachat QuickChem8500 flow injection Nutrient Analyzer.

3.4 Statistical analysis

We employed hierarchical clustering to identify and classify distinct groupings of diatom assemblages from each transect as well as all transects combined (e.g., van Tongeren, 1987; Theriot, 1992; Zong and Horton, 1998). We classified the modern

samples using the Ward's minimum unconstrained cluster analysis based on unweighted Euclidean distance using the software PAST (Hammer et al., 2001).

We analyzed the relationship between the modern diatom assemblages and the environmental variables measured at every station along each transect as well as all transects combined using the ordination method of principal component analysis (PCA; ter Braak, 1986). PCA is an ordination method that relates community composition to environmental variables by reducing the dimensions to principal components (axes) that represent the most variance between the species assemblages and environment (e.g., Abdi et al., 2010). We performed redundancy analysis (RDA) to identify the total variance in diatom assemblages that can be explained by the environmental variables collected. We determined the contribution of each environmental variable to diatom assemblage variance using constrained analysis and interactive forward selection and use a p value < 0.01 as the threshold for a variable to be considered a major factor. To test the influence of site variability in controlling diatom zonation, we include site as a categorical value in our RDA of our Bone River transects and regional dataset. All analyses were performed using the software CANOCO version 4.5 (ter Braak and Šmilauer, 1998; 2002).

4. Results

4.1 Bone River

4.1.1 Bone River Transect 1

Sampling of Bone River Transect 1 is comprised of 16 sampling stations ranging in elevation from 0.50 to 1.99 m above MTL (139 to 256 SWLI; Fig 2). The tidal flat contains trace amounts of *Zostera sp*. The low marsh is comprised of *Salicornia*

virginica and *Triglochin maritima*. The high marsh is dominated by the presence of *Distichlis spicata* and *Potentilla pacifica*. The forested upland contains trees such as *Picea sitchensis* and *Pyrus fusca*. Dissolved inorganic nutrient concentrations are 2.1 µM for NO_3^-/NO_2^-, 8.6 µM for NH_4^+, 1.2 µM for PO_4^{3-}, and 29.3 µM for SiO_4 (Table 1).

We identified 175 species from 53 genera along Bone River Transect 1. *Planothidium delicatulum* was dominant (> 5%) at every sampling station. Marine species such as *Cocconeis scutellum var parvum, Opehora minuta,* and *Opehophora pacifica* are dominant in tidal flat samples. Brackish species such as *Navicula gregaria, Navicula perminuta,* and *Rhopalodia pacifica* become present in low marsh samples. The freshwater species *Pinnularia lagerstedtii* becomes present in the high marsh to upland samples. *Cocconeis scutellum*, an epiphytic species commonly found in the intertidal, was found at high concentrations (≥ 19%) in the higher elevation stations.

Grain-size analysis shows an increase from sand dominated within the tidal flat (60 to 77% sand) to mud dominated within the salt marsh and upland with the maximum mud content at Station 11 (98% mud). Salinity ranges from 4 to 35 ppt and decreases with increasing elevation with a sharp change at Station 10 from 33 to 16 ppt where there is a transition from low to high marsh. TOC increases with elevation, with a notable increase of > 20% organic carbon at Station 14 where there is a transition from high marsh to upland.

Multivariate analyses using hierarchical clustering identified three floral zones at Bone River Transect 1. Cluster A consists of tidal flat samples from Stations 1-6 with an elevation range of 0.50 to 0.78 m above MTL (139 to 162 SWLI). In contrast to the other zones, we observe a lack of freshwater species such as *Nitzschia frustulum* and

Pinnularia lagerstedtii in Cluster A. Cluster B consists of low marsh samples from Stations 7-11 with an elevation range of 1.10 to 1.57 m above MTL (186 to 223 SWLI). We observe a combination of freshwater (e.g., *Nitzschia frustulum*), brackish (e.g., *Rhopalodia pacifica*), and marine species (e.g., *Opephora pacifica*) in Cluster B. Cluster C consists of high marsh and upland samples from Stations 12-16 with an elevation range of 1.65 to 1.99 m above MTL (230 to 256 SWLI). We observe a high abundance of *Cocconeis scutellum* in Cluster C.

PCA produced an Axis 1 with an eigenvalue of 0.38 and an Axis 2 with an eigenvalue of 0.18 that explains 56% of the total variance in the diatom assemblages with 62% explained by the environmental variables (Table 2). The lengths of the environmental arrows on the PCA sample-environment biplot approximate their relative importance in explaining the variance in the diatom data and their orientation demonstrates the approximate correlation to the ordination axes as well as to other environmental variables. Intra-set correlations of environmental variables with axes 1 and 2 show that elevation and mud fraction are correlated with Axis 1 and that TOC and salinity are correlated with both axes 1 and 2 (Fig 2d). PCA Axis 1, therefore, reflects the major gradient from high marsh plotted on the right (high elevation and mud fraction) to tidal flat plotted on the left (low elevation and mud fraction). PCA axes reflect to some extent a TOC and salinity gradient. Constrained and interactive-forward-selection analyses identified elevation (explains 35% of variance) and TOC (explains 14 % of variance) as major explanatory variables with mud fraction (explains 7% of variance) and salinity (explains 6% of variance) as minor explanatory variables (Table 3).

4.1.2 Bone River Transect 2

Sampling of Bone River Transect 2 is comprised of 13 sampling stations in the high marsh with a relatively narrow elevational range from 1.25 to 1.64 m above MTL (199 to 229 SWLI; Fig 3). The high marsh is comprised of *Carex lyngbei, Deschampsia caespitosa, Distichlis spicata, Juncus balticus,* and *Potentilla pacifica*. Dissolved inorganic nutrient concentrations are 2.5 µM for NO_3^-/NO_2^-, 3.0 µM for NH_4^+, 1.4 µM for PO_4^{3-}, and 33.6 µM for SiO_4 (Table 1).

We identified 176 species from 53 genera along Bone River Transect 2. The freshwater species *Luticola mutica* was dominant (> 7%) at all sampling stations. There is a lack of dominant (> 5% maximum abundance) brackish species throughout the transect.

Grain-size analysis shows the relative percent of mud remains relatively constant (92 to 97%) across the transect with the exception of Station 1 (79%). Salinity also displays a relatively constant (16 to 14 ppt) concentration across the transect. TOC shows an increase of ≥ 15% organic carbon at Stations 10-13.

Multivariate analyses using hierarchical clustering identified two floral zones at Bone River Transect 2. Cluster A consists of high marsh stations 1, 2, 5-9, 12 and 13. We observe a combination of freshwater (e.g., *Navicula cincta*) and marine species (e.g., *Tabularia fasciculata*) in Cluster A. Cluster B consists of high marsh stations 3, 4, 10, and 11. We observe the highest abundance of freshwater species *Denticula subtilis* (15%), *Luticola mutica* (27%), and *Pinnularia lagerstedtii* (15%) in Cluster B. PCA produced an Axis 1 with an eigenvalue of 0.22 and an Axis 2 with an eigenvalue of 0.20 that explains 41% of the total variance in the diatom assemblages with 44% explained by the environmental variables (Table 2). Intra-set correlations of environmental variables with axes 1 and 2 show that TOC and elevation are correlated with Axis 1 and that salinity and mud fraction are correlated with both axes 1 and 2

(Fig 3d). PCA Axis 1, therefore, reflects a gradient primarily driven by increased TOC with elevation. PCA axes reflects to some extent a grain size and salinity gradient. Constrained and interactive-forward-selection analyses identified TOC (explains 20% of variance) as the major explanatory variable with salinity (explains 10% of variance), elevation (explains 8% of variance), and mud fraction (explains 6% of variance) as minor explanatory variables (Table 3).

4.1.3 Bone River combined transects

The Bone River Transect 1 and 2 combined dataset is comprised of 29 sampling stations ranging in elevation from 0.50 to 1.99 m above MTL (139 to 256 SWLI). Hierarchical clustering identified four floral zones (Fig 4). Cluster A is comprised of all sampling stations from Bone River Transect 2. The remaining clusters (Cluster B, C, and D) are zoned identically to the hierarchical clustering results from Bone River Transect 1. Cluster B is comprised of high marsh and upland samples from Stations 12-16. Cluster C is comprised of low marsh samples from Stations 7-11. Cluster D is comprised of tidal flat samples from Stations 1-6. PCA produced an Axis 1 with an eigenvalue of 0.32 and an Axis 2 with an eigenvalue of 0.11 that explains 44% of the total variance in the diatom assemblages with 54% explained by the environmental variables (Table 2). Intra-set correlations of environmental variables with axes 1 and 2 show that all variables are correlated with Axis 1 and that elevation is also partly correlated with Axis 2 (Fig 4d). Constrained and interactive-forward-selection analyses identified site (explains 28% of variance), elevation (explains 12% of variance), and TOC (explains 6% of variance) as the major explanatory variables with salinity (explains 5% of variance) and mud fraction (explains 3% of variance) as minor explanatory variables (Table 3).

4.2 Niawiakum River

Sampling of the Niawiakum River consisted of one transect comprised of 20 sampling stations ranging in elevation from -0.80 to 1.79 m above MTL (38 to 239 SWLI; Fig 5). The tidal flat lacks vegetation. The low marsh contains *Glaux maritima, Salicornia virginica, Spartina alterniflora*, and *Triglochin maritima*. The high marsh is comprised of *Carex lyngbei, Distichlis spicata, Juncus balticus,* and *Potentilla pacifica*. Dissolved inorganic nutrient concentrations are 1.5 µM for NO_3^-/NO_2^-, 3.1 µM for NH_4^+, 0.7 µM for PO_4^{3-}, and 18.5 µM for SiO_4 (Table 1).

We identified 208 species from 64 genera along the Niawiakum River Transect. Marine species *Paralia sulcata* and *Thalassiosira pacifica* are dominant in the tidal flat samples. Marine species *Cocconeis scutellum, Paralia sulcata,* and *Thalassiosira pacifica* as well as freshwater species *Luticola mutica* and *Navicula cincta* are dominant in the low marsh samples. The high marsh is comprised of marine (e.g., *Cocconeis scutellum* and *Grammatophora oceanica*), brackish (e.g., *Navicula halophila* and *Navicula sieminskiae*), and freshwater species (e.g., *Luticola mutica* and *Pinnularia lagerstedtii*).

Grain-size analysis shows the relative percent of mud remains > 70% at all sampling stations except Station 5 (59% mud). Salinity steadily decreases with increasing elevation from 24 to 12 ppt. TOC increases with elevation from 2 to 32% with the most notable change between Stations 17 and 18.

Multivariate analyses using hierarchical clustering identified three floral zones at the Niawiakum River Transect. Cluster A consists of tidal flat and low marsh samples from Stations 1-8 with an elevation range of -0.80 to 1.46 m above MTL (38 to 213 SWLI).

We observe a dominance of brackish (e.g., *Navicula halophila*) and marine (e.g., *Paralia sulcata*) species in Cluster A. Cluster B consists of high marsh samples from Stations 9-18 with an elevation range of 1.55 to 1.71 m above MTL (220 to 233 SWLI). We observe a dominance of freshwater species *Luticola mutica* and *Pinnularia lagerstedtii* in Cluster B. Cluster C consists of high marsh samples from Stations 19-20 with an elevation range of 1.75 to 1.79 m above MTL (236 to 239 SWLI). We observe a high abundance (> 10%) of freshwater species *Navicula cryptocephala* as well as brackish species *Nitzschia palustris* and *Navicula sieminskiae*. PCA produced an Axis 1 with an eigenvalue of 0.34 and an Axis 2 with an eigenvalue of 0.15 that explains 49% of the total variance in the diatom assemblages with 52% explained by the environmental variables (Table 2). Intra-set correlations of environmental variables with axes 1 and 2 show that elevation is correlated with Axis 1 and that all other environmental variables (salinity, TOC, mud fraction) are correlated with both axes 1 and 2 (Fig. 5d). PCA Axis 1, therefore, reflects the major gradient from high marsh to tidal flat. Constrained and interactive-forward-selection analyses identified elevation (explains 28% of variance) and salinity (explains 14% of variance) as major explanatory variables with TOC (explains 6% of variance) and mud fraction (explains 4% of variance) as minor explanatory variables (Table 3).

4.3 Naselle River

Sampling of Naselle River Transect is comprised of 18 sampling stations ranging in elevation from 1.20 to 2.57 m above MTL (179 to 269 SWLI; Fig 6). The tidal flat lacks vegetation with only sparse amounts of *Zostera sp*. The low marsh contains *Salicornia virginica* and *Triglochin maritima*. The high marsh is comprised of *Carex lyngbei, Deschampsia caespitosa, Distichlis spicata, Juncus balticus,* and *Potentilla pacifica*.

The forested upland contains trees such as *Picea sitchensis* and *Pyrus fusca*. Dissolved inorganic nutrient concentrations are 2.3 µM for NO_3^-/NO_2^-, 2.4 µM for NH_4^+, 1.1 µM for PO_4^{3-}, and 25.8 µM for SiO_4 (Table 1).

We identified 225 species from 61 genera along the Naselle River Transect. The tidal flat contains a mixture of diatoms, ranging from marine (e.g., *Paralia sulcata* and *Thalassiosira pacifica*) to brackish (e.g., *Navicula gregaria and Staurosirella pinnata*) as well as freshwater (e.g., *Denticula subtilis* and *Nitzschia frustulum*) species. Dominant species in the low marsh include marine species (*Paralia sulcata*), brackish species (*Frustulia linkei* and *Nitzschia clausii*), and freshwater species (*Navicula cincta*). Brackish species (*Staurosirella pinnata*) and freshwater species (*Denticula subtilis* and *Luticola mutica*) are found at > 10% abundance in the high marsh.

Grain-size analysis shows the relative percent of mud remains relatively constant (91 to 99%) throughout the transect. Salinity steadily decreases with increasing elevation from 20 to 8 ppt. TOC increases with elevation from 3 to 36%. We note an anomalous drop from 34 to 23% organic content at Station 17 where there is a transition from high marsh to upland.

Multivariate analyses using hierarchical clustering identified two floral zones at the Naselle River Transect. Cluster A consists predominantly of high marsh samples (Stations 10, 11, 13-18) with one low marsh (Station 8) and tidal flat (Station 4) station that range in elevation from 1.30 to 2.57 m above MTL (186 to 269 SWLI). We observe a high abundance of freshwater species (e.g., *Luticola mutica* and *Denticula subtilis*) in Cluster A. Cluster B contains predominantly tidal flat (Stations 1-3, 5 and 6) and low marsh (Stations 7 and 9) stations as well as one high marsh (Station 12) station that range in elevation from 1.20 to 2.39 m above MTL (179 to 257 SWLI). We observe a

lack of freshwater species in Cluster B and a dominance of brackish (e.g., *Frustulia linkei*, *Nitzschia clausii*, and *Staurosirella pinnata*) and marine diatoms (e.g., *Paralia sulcata* and *Thalassiosira pacifica*). PCA produced an Axis 1 with an eigenvalue of 0.35 and an Axis 2 with an eigenvalue of 0.17 that explains 51% of the total variance in the diatom assemblages with 40% explained by the environmental variables (Table 2). Intra-set correlations of environmental variables with axes 1 and 2 show that salinity, elevation and mud fraction are correlated with Axis 1 and TOC is correlated with both axes 1 and 2 (Fig 6d). PCA Axis 1, therefore, reflects a salinity gradient. Constrained and interactive-forward-selection analyses identified salinity (explains 21% of variance) as the major explanatory variable with elevation (explains 8% of variance), mud fraction (explains 6% of variance), and TOC (explains 5% of variance) as minor explanatory variables (Table 3).

4.4 Regional dataset

The results of our regional modern diatom training set is comprised of 67 sampling stations from four transects at three tidal marshes: Bone River (Transects 1 and 2), Niawiakum River, and Naselle River. We identified a total of 367 species across 94 genera. Multivariate analysis using hierarchical clustering identified four floral zones from the regional dataset (Fig 7):

Cluster A consists of stations from all three tidal marshes (Niawiakum River, Naselle River, Bone River Transect 2) and ranges in elevation from 38 to 257 SWLI, which includes the lowest elevation of the training set. The diatoms are a mix of marine, brackish, and freshwater diatoms with a relatively high abundance of the marine species *Thalassiosira pacifica* compared to the other clusters. The majority of the stations of Cluster A are comprised of tidal flat and low marsh stations with the remaining stations

in the high marsh. Grain size distributions show a range of 59 to 99% mud. Salinity ranges from 14 to 25 ppt. TOC ranges from 2 to 18% organic carbon.

Cluster B also consists of stations from the same three tidal marshes (Niawiakum River, Naselle River, and Bone River Transect 2) and ranges in elevation from 186 to 269 SWLI, which includes the highest elevation of the training set. The diatoms show a relatively high abundance of the freshwater species *Cosmioneis pusilla*, *Denticula subtilis*, *Luticola mutica*, and *Pinnularia lagerstedtii* compared to the other clusters. The stations of Cluster B are predominantly high marsh stations with the exception of one low marsh (Naselle River Transect Station 4) and one upland (Naselle River Transect Station 18) station. Grain size distributions show a dominance of mud (78 to 99% mud) with relatively low salinities (8 to 20 ppt). There is a large range of TOC from 4 to 36%.

Cluster C consists of Stations 1-11 of Bone River Transect 1, which range in elevation from 139 to 223 SWLI. Cluster C combines Cluster A and B from the hierarchical clustering analysis of Bone River Transect 1. The diatoms show a dominance of marine diatoms with a high concentration (> 5%) of *Planothidium delicatulum* at every sampling station. The stations are predominantly tidal flat and low marsh with one station from the high marsh (Station 11). Grain size distributions range have a large range from 24 to 98% mud. Salinity is relatively high (16 to 35 ppt) and the range of TOC is relatively low (< 1 to 13%).

Cluster D consists of Stations 12-16 of Bone River Transect 1 (identical to Cluster C of section 4.1) with an elevation range of 230 to 256 SWLI. The diatoms also contain a high concentration (> 5%) of *Planothidium delicatulum* at every sampling station in addition to a high abundance of *Cocconeis scutellum*. The stations include high marsh

and upland stations. Grain size distributions range from 41 to 91% mud. Compared to Cluster C, salinity is lower (4 to 14 ppt) and the range of TOC is higher (14 to 27%).

PCA produced an Axis 1 with an eigenvalue of 0.25 and an Axis 2 with an eigenvalue of 0.12 that explains 37% of the total variance in the diatom assemblages with 34% explained by the environmental variables (Table 2). The intra-set correlations of environmental variables with axes 1 and 2 show that site, elevation, TOC, and mud fraction are correlated with Axis 1 and salinity is correlated with Axis 2 (Fig 7d). Constrained and interactive-forward-selection analysis identified salinity (explains 15% of variance), site (explains 7% of variance), elevation (explains 5% of variance), and TOC (explains 4% of variance) as major explanatory variables and mud fraction (explains 3% of variance) as a minor explanatory variable Table 3).

5. Discussion

5.1 Diatom distributions in Willapa Bay

Consistent with other studies throughout the Pacific Northwest (e.g., Nelson and Kashima, 1993; Hemphill-Haley, 1995a,b; Sherrod 1999) and elsewhere (e.g., Admiraal, 1977; Zong and Horton, 1998; Sawai et al., 2001), the Bone River Transect 1 and the Niawiakum River Transect display a vertical zonation of diatom assemblages where diatoms can be used to distinguish the tidal flat, low marsh, and high marsh environment. In particular, Bone River Transect 1 is ideally suited for correlations between diatom abundances and flooding frequency because it slopes gently towards the bay and lacks an undulating topography formed by creeks, levees, and pools (features common to many other salt marshes; Horton et al., 1999).

In the tidal flats of Bone River Transect 1 and the Niawiakum River Transect, which are associated with coarser grain size, low organic content, and high salinity, we see epiphytic (attachment to aquatic plants) and epipsammic (attachment to sand) marine species such as *Cocconeis scutellum var parva*, *Grammatophora oceanica,* and *Opephora pacifica*. Hemphill-Haley (1995b) also found vertical zonation of diatom assemblages from two transects along the Niawiakum River with some comparable marine species (e.g., *Endictya sp*, *Delphineis surirella*, and *Grammatophora oceanica*) that are indicative of the tidal flat. Further, Sawai et al. (2016) found similar marine species indicative of the tidal flat in estuaries along the Oregon coast.

The low marshes are associated with finer grain size, slightly increased organic content, and slightly decreased salinity. The changing environmental conditions from the tidal flat to low marsh coincide with a decrease in marine species (e.g., Nelson and Kashima, 1993; Hemphill-Haley, 1995b; Sherrod, 1999) and the appearance of brackish species such as *Navicula halophila* and *Navicula gregaria* (e.g., Sawai et al., 2016). Additionally, we observe the presence of both marine (e.g., *Opephora pacifica*) and freshwater (e.g., *Luticola mutica*) diatom species, which have been shown to display a wide tolerance of intertidal environments and can be found in high abundances in low marsh environments of the Pacific Northwest (e.g., Hemphill-Haley, 1995b; Sherrod, 1999) and U.K. (Zong and Horton, 1998). Hemphill-Haley (1995b) identified brackish species (e.g., *Frustulia linkei, Gyrosigma eximium*, *and Mastogloia exigua*) indicative of the low marsh. Although we do not find these brackish species in high abundance at the Bone River Transect 1 and the Niawiakum River Transect, we do find *Frustulia linkei* at a high abundance in the low marsh of our Naselle River Transect (Fig 6a).

The high marshes of Bone River Transect 1 and the Niawiakum River Transect are associated with a dominance of mud, high organic content, low salinity and the highest elevations and thus lowest flooding frequency. We observe aerophilous (tolerant of temporarily dry conditions) freshwater species such as *Navicula cincta*, *Nitzschia terrestris*, and *Pinnularia lagerstedtii*. These species have been documented as indicative of the high marsh environment in estuaries throughout the coast of Oregon and Washington, including the Puget Sound (Sherrod, 1999; Hemphill-Haley, 1995b; Sawai et al., 2016). Hemphill-Haley (1995b) found similar freshwater species (e.g., *Navicula cincta*) in the high marsh of both Niawiakum River transects. A regional diatom distribution study by Sawai et al. (2016) included 12 samples throughout the high marsh from the upper reaches of Niawiakum River and found a dominance of freshwater species *Cosmioneis pusilla*, *Denticula subtilis*, *Luticola mutica*, *Nitzschia brevissima*, *and Tryblionella debilis*.

The Naselle River Transect, however, does not display a vertical zonation because marine, brackish, and freshwater diatoms are found in relatively high abundance at all sampling stations. For example, Station 12 is located in the high marsh, but is dominated (> 5%) by the marine species *Cocconeis scutellum*, *Grammatophora oceanica*, and *Paralia sulcata*. In contrast, Station 4 is located in the tidal flat but shows a high abundance of the freshwater species *Denticula subtilis* and *Luticola mutica*. A lack of vertical zonation across intertidal environments has been found in estuaries throughout the Mid-Atlantic region (Desianti et al., 2019) and on the west coast of the United States (e.g. Moore and McIntire, 1977; Sawai et al., 2016). A study by McIntire (1978) shows that discontinuities in environmental conditions will override elevation as the dominant environmental control and can lead to patchy distributions of diatoms.

1.2 Environmental drivers of diatom zonation

The results of our environmental analysis show that elevation, salinity, and substrate (grain size and organic content) are important drivers of diatom variability (Table 3). However, we note that the dominant environmental controls of diatom assemblage zonation differ by site. These results are similar to a regional diatom distribution study of 11 estuaries by Sawai et al. (2016) that found dominant environmental controls varied by site and were attributed to differences in the physiographic features of the individual estuaries.

Elevation is shown to be the dominant environmental factor at Bone River Transect 1 (35% of variation) and the Niawiakum River Transect (28% of variation) where the diatoms display a clear vertical zonation (Table 3; Fig 2 and 5). These results have also been observed by other studies that show the distribution of diatoms across the intertidal are a function of elevation with respect to the tidal frame (e.g., Zong and Horton, 1998; Nelson and Kashima, 1993; Hemphill-Haley, 1995b; Horton et al., 2006). The importance of elevation as an environmental control on modern diatom distributions is due to the co-varying relationship between elevation and other environmental factors that also influence diatom distributions (e.g., Nelson and Kashima, 1993).

Salinity is shown to be the dominant environmental factor at the Naselle River Transect (21% of variance) and the regional training set (15% of variance), which is consistent with studies that show salinity as the dominant control in diatom distribution (e.g., Hendy, 1964; Amspoker and McIntire, 1978; Hassan et al., 2009). The sensitivity of diatoms to salinity is shown in a study of modern diatom distributions from Yaquina Estuary, OR that found large differences in diatom assemblages between adjacent sampling stations as a result of rapid changes in salinity along the sampled gradient

(McIntire, 1978). Despite elevation as the major explanatory variable of diatom assemblage distribution at two of our transects, the regional training set shows salinity is most closely associated with the positive direction of Axis 1 where we observe a separation of Bone River Transect 1 from the other transects. We note that Bone River Transect 1 displays the greatest variance in salinity (4 to 35 ppt) compared to the other transects. The importance of salinity as a control on the distribution of diatom assemblages is shown by Sherrod (1999) who used canonical correspondence analysis to show that elevation is secondary to salinity as the major explanatory variable in diatom assemblage distribution in a Puget Sound, WA salt marsh.

Diatom preferences for attaching to particular substrate (e.g., epipsammic or epiphytic) are well established as influencing the abundance and distribution of diatoms across intertidal zones (e.g., Kosugi, 1987; Vos and de Wolf, 1993). The high frequencies of epipelic diatoms are associated with fine-grained (mud) sediments, whilst sandy substrate is related to epipsammic taxa (e.g. Nelson and Kashima, 1993; Zong, 1997; Zong and Horton, 1998, 1999). Local studies in the Pacific Northwest have shown grain size to be an important environmental variable controlling diatom distributions (e.g., Whiting and McIntire, 1985; Amspoker and McIntire, 1978; Sawai et al., 2016). In contrast, our results show mud concentration is not a major driver of diatom variability at any of our sites. The minor influence of grain size may be due to the relatively uniform distribution of mud at three of the four transects and inter-correlations between mud fraction and elevation at Bone River Transect 1.

At Bone River Transect 2, which is located entirely within the high marsh, we find that TOC is the dominant environmental factor (20% of variance; Table 3) and is the second most dominant factor at Bone River Transect 1 (14% of variance; Table 3). Our study

highlights the importance of organic content (as a factor of substrate) in determining species diversity in the intertidal zone. This conclusion is supported by Sawai et al. (2016) that found loss-on-ignition (% organic matter) explained the most variance at 4 out of 11 estuaries of the Oregon coastline. Diatom sensitivity to organic content, which is an indicator of trophic conditions, is well established and forms the basis of the saprobic diatom classification system (Sladecek, 1986).

Our study provides an opportunity to consider the effects of inter- and intra-site spatial variability in diatom distribution at Willapa Bay from the same study. With the inclusion of site as a categorical value in our regional analysis and the Bone River combined transects, the results show that spatial variability is an influencing factor in diatom distributions across the intertidal zone. The results of the regional training set show salinity (15% of variance) and site (7% of variance) as the two most dominant environmental factors (Table 3). The results from our individual transects show that in spite of overlapping tidal environments and elevation, inter-site variability among dominant diatom assemblages exist (Fig 7) with only the freshwater species *Pinnularia lagerstedtii* and the marine species *Cocconeis scutellum* found at an abundance of > 5% at the Bone River, Niawiakum River, and Naselle River (Fig 2a, 5a, 6a). The widespread distribution of *Cocconeis scutellum* may be due to counting both frustules and P-valves where P-valves are susceptible to secondary transport (e.g., Sawai et al., 2001).

Differences in dominant species between transects and the widespread distribution of species across more than one intertidal zone suggest diatom preference for particular environments are indiscrete and oftentimes transitional across a large range of the intertidal zone (e.g., McIntire, 1978). Previous studies have documented site variability

in diatom assemblages within coastal environments in the United Kingdom (e.g., Gehrels et al., 2001), Indonesia (e.g., Horton et al., 2007), and the Atlantic and Pacific coasts of the United States (e.g., Nelson et al., 2008; Kemp et al., 2009). For example, site-specific variability was also observed by Nelson and Kashima (1993) who noted variations in the vertical range and boundaries of diatom assemblage zones from four transects in southern Oregon. Additionally, variations in nutrient concentrations can influence species diversity (e.g., Peletier, 1996; Lange et al., 2011) and the growth rate of taxa (e.g., Hutchins and Bruland, 1998; Sarthou et al., 2005). However, nutrients strongly co-vary with other environmental factors, which limits our ability to interpret the relationship between diatom assemblages and nutrient concentrations (Desianti et al., 2019). Because many of our species are unassociated with a specific trophic condition (Denys, 1991), we did not explore the role of nutrients as an environmental factor.

We can consider the effects of intra-site variability using the Bone River dataset where transects from the same site have overlapping elevations. Constrained and interactive-forward-selection analyses on the Bone River combined transects identified site (explains 28% of variance) and elevation (explains 12% of variance) as the most dominant environmental factors (Table 3). These results suggest that intra-site variability exists and results in the separation of diatom assemblages within the same site with very similar environmental conditions. This site-specific variability is similar to results found by McIntire (1978) and Sawai et al. (2016), who noted differences in assemblages between adjacent sampling stations and in samples in near-identical environments of the Pacific Northwest. A spatial distribution study by McIntire and Overton (1971) in Yaquina Bay, Oregon partially attributed these differences to the micro-topography of coastal wetlands that may result in irregular or discontinuous

environmental gradients and, subsequently, a patchy distribution of diatom assemblages. In marshes without a distinct elevational gradient (e.g., Bone River Transect 2), variations in the balance between seepage, precipitation, and flooding have been shown to influence the distribution of flora and fauna (de Rijk, 1995a, b; de Rijk and Troelstra, 1997).

Our study shows no one variable consistently defines diatom assemblage distribution in intertidal zones because diatoms exhibit a complex relationship with environmental variables. The results of our regional analysis found that only 34% of the diatom variance could be explained by the measured environmental variables (elevation, grain size, TOC, and salinity). Higher rates of explanation are found at individual transects (Bone River Transect 1: 62%; Bone River Transect 2: 44%; Niawiakum River Transect: 52%; Naselle River Transect: 40%). Although the percentage of explained variation in our study is consistent with other diatom studies due to the large sample size and many zero values inherent in biological datasets (Gasse et al., 1995; Jones and Juggins, 1995; Zong and Horton, 1998, Sawai et al., 2016), the unexplained variance may be due to environmental variables that were not analyzed in this study. In addition to factors such as tidal exposure, substrate, and salinity, diatom assemblages may be influenced by variables such as light intensity (e.g., Castenholz, 1961; McIntire, 1978; Admiraal and Peletier, 1980), temperature (e.g., Amspoker and McIntire, 1978; McIntire, 1978), and desiccation (e.g., Castenholz, 1961; Amspoker and McIntire, 1978).

5.3 Implications of diatom variability for sea-level reconstructions due to earthquakes in the Pacific Northwest of North America

Microfossils (diatoms, foraminifera, and pollen) have been used to reconstruct past RSL change in the United Kingdom (e.g., Zong and Horton, 1999; Horton and Edwards,

2006; Hill et al., 2007), Japan, (Sawai et al., 2004a, b), Alaska, (e.g., Zong et al., 2003; Shennan and Hamilton, 2006; Barlow et al., 2012; Watcham et al., 2013) and elsewhere (e.g., Hughes et al., 2002; Horton et al., 2006; Woodroffe and Long, 2010: Garrett et al., 2013; Hocking et al., 2017). In the Pacific Northwest, microfossil-based transfer functions have provided quantitative estimates of RSL rise from earthquakes with sample-specific errors (e.g., Guilbault et al., 1996; Hawkes et al., 2010; Milker et al., 2016). Sea-level reconstructions using transfer functions rely on an empirically derived relationship between species of microorganisms and tidal inundation to infer quantitative estimates of RSL change (Shennan et al., 1996; Sherrod, 1999; Hawkes et al., 2011). These transfer functions employ a training set of modern assemblages sampled from measured elevations that range from the tidal flat to upland to numerically calibrate the relationship between the modern assemblage and elevation (Birks, 1995; Zong and Horton, 1999; Sherrod, 2001; Horton and Edwards, 2006). The transfer function is applied to fossil assemblage data from sediment sequences to produce a continuous record of earthquake-related RSL change through time (Sawai et al., 2004; Nelson et al., 2008; Milker et al., 2016).

A rapid response time is critical for understanding RSL change caused by earthquakes along active margins, such as the Cascadia subduction zone in the Pacific Northwest of North America (e.g., Engelhart et al., 2013; Horton et al., 2017). Diatom-based reconstructions along the Cascadia subduction zone are important because diatoms have been shown to have an advantage over foraminifera in response time (e.g., Horton et al., 2017). A sudden tidal-flooding experiment in a southern Oregon salt marsh found that diatoms responded within two weeks of flooding compared to the 11 months required before foraminifera assemblages showed notable and lasting change, suggesting that diatom-based transfer functions are more likely to accurately record

immediate changes in sea-level (Horton et al., 2017). However, quantitative estimates of relative sea-level rise from earthquakes in the Pacific Northwest have been hampered by site-specific diversity of diatom assemblages that lead to a no matching analogue problem from which fossil diatom comparisons are limited by the lack of present-day analogues from which to reconstruct past sea levels (e.g., Nelson and Kashima, 1993, Nelson et al., 2008).

The results of our study show the difficulty in overcoming the no matching analogue problem due to the site-specific diversity of diatoms. To address the no matching analogue problem, Sawai et al. (2016) concluded that a large sample size that covers a broad range of modern depositional environments is necessary in order to accurately capture the full ecological tolerance of diatom species. A solution would therefore be to combine our results with the studies of Hemphill-Haley (1995b) and Sawai et al. (2016) in Willapa Bay. Although we have noted similarities with Hemphill-Haley (1995b) and Sawai et al. (2016) in species distributions across the tidal frame, we also identify large differences in relative abundance (e.g., the brackish species *Gyrosigma eximium*) or an absence of dominant species (e.g., the freshwater species *Diadesmis contenta*). Differences in dominant species across the intertidal zone compared to Hemphill-Haley (1995b) and Sawai et al. (2016) may be due to differences in taxonomic identification. Differences in taxonomy are difficult to amend and have been shown to affect interpretations between diatom assemblages and environmental variables (e.g., Lee et al., 2019). Furthermore the study by Hemphill-Haley (1995b) was collected > 20 years ago, since when environmental conditions of the estuary will have changed. For example, the rapid spread of eastern cordgrass (*Spartina alterniflora*) since the 1980's has reduced the usability of the mudflat environment for fish, birds, and shellfish throughout Willapa Bay (Emmett et al., 2000).

Even if we were able to overcome taxonomic differences, a large sample size may fail to provide a modern analogue. For example, Watcham et al. (2013) found that a regional training set with a sample size as high as 166 was insufficient in providing a reliable relative sea-level reconstruction due to modern diatoms displaying site-specific, highly diverse distributions and local factors that exert a greater influence on diatom ecology. Therefore, to address the no matching analogue problem, we suggest the grouping of species that display similarities in abundance and distribution across the intertidal zone. Bioassessment studies of riverine pollution have shown that grouping diatoms is an effective approach for providing ecological assessments. Fore and Grafe (2002) developed a multi-metric index of diatoms that were grouped based on attributes (e.g., tolerance or intolerance for pollution, autoecological guild, morphological guild, and individual condition). The results of grouping diatoms resulted in the amplification of observed ecological patterns that were also observed at the species level, suggesting that grouping diatoms does not diminish its ability to provide accurate ecological assessments (Fore and Grafe, 2002). Passy (2007) grouped diatoms based on growth form to show more distinct distributions along nutrient and disturbance gradients than the species-level analysis. These studies show that grouping species based on abundance and distribution across the intertidal zone are likely to maintain its ability to predict elevation while addressing the matching analogue problem. Grouping diatoms would provide the added advantage of reducing the number of species to allow for performing statistical analyses requiring fewer species than samples (e.g., ter Braak and Šmilauer, 2002; Sawai et al., 2016).

6. Conclusion

We assess the inter- and intra-site variability of a modern diatom training set from Willapa Bay, Washington. We collected 67 samples from four shore-perpendicular transects at three tidal marshes: (1) the Bone River; (2) the Niawiakum River; (3) and the Naselle River.

In addition to measuring the elevation at each sampling station, we analyzed four environmental variables: grain-size, TOC, porewater salinity, and nutrient concentrations to characterize the relationship between diatom assemblages and environmental variables. Grain-size analysis shows the relative percent of mud remains above 50% at all sampling stations except the tidal flat, low marsh, and Station 12 from Bone River Transect 1 where sand is dominant. Salinity decreases with increasing elevation at all sites with the greatest range in salinity occurring at Bone River Transect 1 (4 to 35 ppt). TOC increases with elevation with the greatest range in organic carbon occurring at the Naselle River Transect (3 to 36%). Dissolved inorganic nutrient values showed NO_3^-/NO_2^- ranging from 1.50 at the Niawiakum River to 2.50 µM at the Bone River near Transect 2. Concentrations of NH_4^+ ranged in value from 2.40 at the Naselle River to 8.60 µM at the Bone River near Transect 1. PO_4^{3-} values ranged from 0.70 at the Niawiakum River to 1.40 µM at the Bone River near Transect 2. SiO_4 concentrations ranged in value from 18.5 at the Niawiakum River to 33.6 µM at the Bone River near Transect 2.

The modern training set consisted of 367 diatoms species across 94 genera and captures the range of diatoms found in marine, brackish, and freshwater environments. In the tidal flat, which is associated with coarser grain size, low organic content, and high salinity, we see epiphytic and epipsammic marine species such as *Cocconeis scutellum*

var parva, *Grammatophora oceanica,* and *Opephora pacifica*. Transitioning from the tidal flat to low marsh resulted in finer grain size, slightly increased organic content, and lower salinity where species that are tolerant of a wider salinity range (e.g., *Opephora pacifica*, *Navicula gregaria*, and *Luticola mutica*) were found. In the high marsh, which is associated with a dominance of mud, high organic content, and low salinity, we observe aerophilous freshwater species such as *Navicula cincta*, *Nitzschia terrestris*, and *Pinnularia lagertedtii*.

Hierarchical clustering and ordination of individual and regional training sets identified floral zones with differing controls by the environmental variables. We can summarize the analyses as follows:

1. We observed vertical zonation of diatom assemblages at two of our sites where diatom assemblages showed a distinct separation of the tidal flat, low marsh, and high marsh. Three floral zones were identified at Bone River Transect 1, which displayed a vertical zonation with elevation (35% of variance) and TOC (14% of variance) as major environmental controls. Three floral zones were identified at Niawiakum Transect, which had a vertical zonation with elevation (28% of variance) and salinity (14% of variance) as the major environmental controls.
2. The Naselle River Transect does not show vertical zonation as marine, brackish, and freshwater species are found in relatively high abundance across the transect. We identified two floral zones with salinity (21% of variance) as the major environmental control.
3. Our regional training set shows that in spite of overlapping tidal environments and elevation, site-specific variability among dominant diatom assemblages

exist. We identified four floral zones with salinity (15% of variance), site (7% of variance), elevation (5% of variance), and TOC (4% of variance) as the major environmental controls.

4. An intra-site comparison of two transects at Bone River show separation based on transect despite overlapping elevation. Four floral zones were identified with one cluster consisting entirely of Bone River Transect 2 stations and the remaining three clusters separating identically to the hierarchical clustering results from Bone River Transect 1.

Our findings show that the precision of diatom-based, relative sea-level reconstructions can be limited due to the high spatial variability of coastal diatoms in Willapa Bay that lead to a no matching analogue problem. In the absence of a large training set that covers a broad range of environments across intertidal zones, alternative methods must be sought to address these limitations.

References

Abdi, H., and Williams, L. J., 2010, Principal component analysis: Wiley interdisciplinary reviews: computational statistics, v. 2, no. 4, p. 433-459.

Admiraal, W. 1977a. Influence of light and temperature on the growth rate of estuarine benthic diatoms in culture. Marine Biology 39: 1–9.

Admiraal, W., and Peletier, H., 1980, Influence of seasonal variations of temperature and light on the growth rate of cultures and natural populations of intertidal diatoms: Mar. Ecol. Prog. Ser, v. 2, no. 35-43.

Admiraal, W., 1984. The ecology of estuarine sediment-inhabiting diatoms. Progress in Phycological Research 3, 269-322.

Amspoker, M. C., and McIntire, C. D., 1978, Distribution of intertidal diatoms assoicated with sediments in Yaquina Bay Estuary, Oregon 1, 2: Journal of Phycology, v. 14, no. 4, p. 387-395.

Atwater, B. F., and Hemphill-Haley, E., 1997, Recurrence intervals for great earthquakes of the past 3,500 years at northeastern Willapa Bay, Washington: USGPO; Information Services [distributor], 2330-7102.

Banas, N., and Hickey, B., 2005, Mapping exchange and residence time in a model of Willapa Bay, Washington, a branching, macrotidal estuary: Journal of Geophysical Research: Oceans, v. 110, no. C11.

Barlow, N.L.M., Shennan, I., Long, A.J., 2012. Relative sea-level response to Little Ice Age ice mass change in south central Alaska: reconciling model predictions and geological evidence. Earth and Planetary Science Letters, v. 315, p. 62-75.

Barlow, N. L.M., Shennan, I., Long, A. J., Gehrels, W. R., Saher, M. H., Woodroffe, S. A., and Hillier, C., 2013, Salt marshes as late Holocene tide gauges: Global and Planetary Change, v. 106, p. 90-110.

Battarbee, R. W., Jones, V. J., Flower, R. J., Cameron, N. G., Bennion, H., Carvalho, L., and Juggins, S., 2002, Diatoms, Tracking environmental change using lake sediments, Springer, p. 155-202.

Birks, H. j. b., Braak, C. j. f. T., Line, J. M., Juggins, S., Stevenson, A. C., Battarbee, R. W., Mason, B. J., Renberg, I., and Talling, J. F., 1990, Diatoms and pH reconstruction: Philosophical Transactions of the Royal Society of London. B, Biological Sciences, v. 327, no. 1240, p. 263-278.

Castenholz, R. W., 1961, The effect of grazing on marine littoral diatom populations: Ecology, v. 42, no. 4, p. 783-794.

Conger, P. S., 1951, Diatoms: The Scientific Monthly, v. 73, p. 315-323.

Cooke, S.S., 1997. *A Field Guide to the Common Wetland Plants of Western Washington & Northwestern Oregon*. Seattle Audubon Society.

Darienzo, M. E., and Peterson, C. D., 1990, Episodic tectonic subsidence of late Holocene salt marshes, northern Oregon central Cascadia margin: Tectonics, v. 9, no. 1, p. 1-22.

Denys, L., 1991/2, A check-list of the diatoms in the Holocene deposits of the western Belgian coastal plain with a survey of their apparent ecological requirements. I. Introduction, ecological code and complete list, Geological Survey of Belgium.

de Rijk, S., 1995a. Agglutinated foraminifera as indicators of salt marsh development in relation to Late Holocene sea level rise (PhD Dissertation), Vrije Universiteit Amsterdam, 188 p.

de Rijk, S., 1995b. Salinity control on the distributon of salt marsh foraminifera (Great Marshes, Massachusetts: Journal of Foraminiferal Research, n. 25, no. 2, p. 156-166.

Desianti, N., Enache, M.D., Griffiths, M., Biskup, K., Dege, A., DaSilva, M., Millermann, D., Lippincott, L., Watson, E., Gray, A., Nikitina, D., Potapova, M., 2019. The potential and Limitations of Diatoms as Environmental Indicators in Mid-Atlantic Coastal Wetlands: Estuaries and Coasts. doi: https://doi.org/10.1007/s12237-019-00603-4.

Donato, S., Reinhardt, E., Boyce, J., Pilarczyk, J., and Jupp, B., 2009, Particle-size distribution of inferred tsunami deposits in Sur Lagoon, Sultanate of Oman: Marine Geology, v. 257, no. 1-4, p. 54-64.

Emmett, R., Llansó, R., Newton, J., Thom, R., Hornberger, M., Morgan, C., Levings, C., Copping, A., and Fishman, P., 2000, Geographic signatures of North American West Coast estuaries: Estuaries, v. 23, no. 6, p. 765-792.

Engelhart, S. E., Vacchi, M., Horton, B. P., Nelson, A. R., and Kopp, R. E., 2015, A sea-level database for the Pacific coast of central North America: Quaternary Science Reviews, v. 113, p. 78-92.

Fore, L. S., and Grafe, C., 2002, Using diatoms to assess the biological condition of large rivers in Idaho (USA): Freshwater Biology, v. 47, no. 10, p. 2015-2037.

Fritz, S. C., Juggins, S., Battarbee, R. W., and Engstrom, D. R., 1991, Reconstruction of past changes in salinity and climate using a diatom-based transfer function: Nature, v. 352, no. 6337, p. 706-708.

Garrett, E., Shennan, I., Watcham, E., and Woodroffe, S., 2013, Reconstructing paleoseismic deformation, 1: modern analogues from the 1960 and 2010 Chilean great earthquakes: Quaternary Science Reviews, v. 75, p. 11-21.

Gasse, F., Juggins, S., Khelifa, L.B., 1995. Diatom-based transfer functions for inferring past hydrochemical characteristics of African lakes: Palaeogeography, Palaeoclimatology, Palaeoecology, v. 117, p. 31-54.

Gehrels, W. R., Roe, H. M., and Charman, D. J., 2001, Foraminifera, testate amoebae and diatoms as sea-level indicators in UK saltmarshes: a quantitative multiproxy approach: Journal of Quaternary Science: Published for the Quaternary Research Association, v. 16, no. 3, p. 201-220.

Haggart, B. A., 1986, Relative sea-level change in the Beauly Firth, Scotland: Boreas, v. 15, no. 2, p. 191-207.

Hassan, G. S., Espinosa, M. A., and Isla, F. I., 2009, Diatom-based inference model for paleosalinity reconstructions in estuaries along the northeastern coast of Argentina: Palaeogeography, Palaeoclimatology, Palaeoecology, v. 275, no. 1-4, p. 77-91.

Hammer, Ø., Harper, D.A.T., Ryan, P.D. 2001. PAST: Paleontological statistics software package for education and data analysis. Palaeontologia Electronica 4(1): 9pp. http://palaeo-electronica.org/2001_1/past/issue1_01.htm

Hemphill-Haley, E., 1995a. Diatom evidence for earthquake-induced subsidence and tsunami 300 years ago in southern coastal Washing. Geol. Soc. Am. Bull. 107, 367-378.

Hemphill-Haley, E., 1995b. Intertidal diatoms from Willapa Bay, Washington: applications to studies of small-scale sea-level changes. Northwest Science 69, 29-45.

Hemphill-Haley, E., 1996, Diatoms as an aid in identifying late-Holocene tsunami deposits: The Holocene, v. 6, no. 4, p. 439-448.

HemphillHaley, E., 1995, Intertidal diatoms from Willapa Bay, Washington: application to studies of small-scale sea-level changes.

Hendy, N., 1964, An introductory account of the smaller algae of British Coastal Waters. V: Bacillariophyceae (Diatoms), p. 1-317.

Hill, T. C., Woodland, W. A., Spencer, C. D., and Marriott, S. B., 2007, Holocene sea-level change in the Severn Estuary, southwest England: a diatom-based sea-level transfer function for macrotidal settings: The Holocene, v. 17, no. 5, p. 639-648.

Hocking, E. P., Garrett, E., and Cisternas, M., 2017, Modern diatom assemblages from Chilean tidal marshes and their application for quantifying deformation during past great earthquakes: Journal of Quaternary Science, v. 32, no. 3, p. 396-415.

Horton, B., Edwards, R., and Lloyd, J., 1999, A foraminiferal-based transfer function: implications for sea-level studies: The Journal of Foraminiferal Research, v. 29, no. 2, p. 117-129.

Horton, B. P., Corbett, R., Culver, S. J., Edwards, R. J., and Hillier, C., 2006, Modern saltmarsh diatom distributions of the Outer Banks, North Carolina, and the development of a transfer function for high resolution reconstructions of sea level: Estuarine, Coastal and Shelf Science, v. 69, no. 3-4, p. 381-394.

Horton, B. P., and Edwards, R. J., 2006, Quantifying Holocene sea level change using intertidal foraminifera: lessons from the British Isles: Departmental Papers (EES), p. 50.

Horton, B. P., Zong, Y., Hillier, C., and Engelhart, S., 2007, Diatoms from Indonesian mangroves and their suitability as sea-level indicators for tropical environments: Marine Micropaleontology, v. 63, no. 3-4, p. 155-168.

Horton, B. P., Milker, Y., Dura, T., Wang, K., Bridgeland, W. T., Brophy, L. S., Ewald, M., Khan, N., Engelhart, S. E., Nelson, A. R., and Witter, R. C., 2017, Microfossil measures of rapid sea-level rise: Timing of response of two microfossil groups to a sudden tidal-flooding experiment in Cascadia: Geology, v. 45, no. 6, p. 535-538.

Hughes, J.F., Mathewes, W.R., and Clague, J.J., 2002, Use of pollen and vascular plants to estimate coseismic subsidence at a tidal marsh near Tofino, British Columbia: Palaeogeography, Palaeoclimatology, Plaeoecology, v. 185, p. 145-161.

Hutchins, D. A., and Bruland, K. W., 1998, Iron-limited diatom growth and Si: N uptake ratios in a coastal upwelling regime: Nature, v. 393, no. 6685, p. 561.

Hustedt, F., 1937. Systematische und okologische Untersuchungen der Diatomeen floren von Java, Bali, Sumatra. Arch. Hydrobiol. Suppl. 15, 131–506.

Hustedt, F., 1939. Systematische und okologische Untersuchungen der Diatomeen floren von Java, Bali, Sumatra. Arch. Hydrobiol. Suppl. 16, 1–394.

Hustedt, F., 1953. Diatomeen ausdem Naturschutzpark Seeon. Archiv f¨ur. Hydrobiologie 47, 625–635.

Hustedt, F., 1957. Die Diatomeenflora des Fluss-systems der Weser im Gebiet der Hansestadt Bremen. Abhandlungen vom Naturwissenschaftlichen Verein zu Bremen 4, 181–440

Jones, V., and Juggins, S., 1995, The construction of a diatom-based chlorophyll a transfer function and its application at three lakes on Signy Island (maritime Antarctic) subject to differing degrees of nutrient enrichment: Freshwater biology, v. 34, no. 3, p. 433-445.

Lee, S.S., Bishop, I.W., Spaulding, S.A., Mitchell, R.M., Yuan, L.L., 2019. Taxonomic harmonization may reveal a stronger association between diatom assemblages and total phosphorus in large datasets: Ecological Indicators, v. 102, p. 166-174.

Kemp, A. C., Horton, B. P., Corbett, D. R., Culver, S. J., Edwards, R. J., and van de Plassche, O., 2009, The relative utility of foraminifera and diatoms for reconstructing late Holocene sea-level change in North Carolina, USA: Quaternary Research, v. 71, no. 1, p. 9-21.

Kosugi, M. 1987. Limiting factors on the distribution of benthic diatoms in coastal regions – salinity and substratum. Diatom v. 3, p. 21–31.

Krammer K and Lange-Bertalot H (1986) Bacillarophyceae 2/1. Naviculaceae. In: Ettl H, Gerloff J, Heynig H and Mollenhauser (Eds.) *Süsswasserflora von Mitteleuropa*. Stuttgart: Gustav Fischer Verlag.

Krammer K and Lange-Bertalot H (1988) Bacillarophyceae 2/2. Basillariaceae, Epithemiaceae, Surirellaceae. In: Ettl H, Gerloff J, Heynig H and Mollenhauser (Eds.) *Süsswasserflora von Mitteleuropa*. Stuttgart: Gustav Fischer Verlag.

Krammer K and Lange-Bertalot H (1991a) Bacillarophyceae 2/3. Centrales, Fragilariaceae, Eunotiaceae. In: Ettl H, Gerloff J, Heynig H and Mollenhauser (Eds.) *Süsswasserflora von Mitteleuropa*. Stuttgart: Gustav Fischer Verlag.

Krammer K and Lange-Bertalot H (1991b) Bacillarophyceae 2/4. Achnanthaceae, Kritische Erganzungen zu Navicula (Lineolatae) und Gomphonema. In: Ettl H (Ed.) *Pascher's Süsswasserflora von Mitteleuropa* 2(4). Stuttgart: Gustav Fischer Verlag.

Lange, K., Liess, A., Piggott, J. J., Townsend, C. R., and Matthaei, C. D., 2011, Light, nutrients and grazing interact to determine stream diatom community composition and functional group structure: Freshwater Biology, v. 56, no. 2, p. 264-278.

McIntire, C. D., 1978, The distribution of estuarine diatoms along environmental gradients: a canonical correlation: Estuarine and Coastal Marine Science, v. 6, no. 5, p. 447-457.

Mcintire, C. D., and Amspoker, M. C., 1986, Effects of sediment properties on benthic primary production in the Columbia River estuary: Aquatic botany, v. 24, no. 3, p. 249-267.

McIntire, C. D., and Overton, W. S., 1971, Distributional patterns in assemblages of attached diatoms from Yaquina Estuary, Oregon: Ecology, v. 52, no. 5, p. 758-777.

Moore, W.W., and McIntire, C.D., 1977. Spatial and Seasonal Distribution of Littoral Diatoms in Yaquina Estuary, Oregon (USA): Botanica Marina, v. 20, no. 2, p. 99-109.

Nelson, A. R., and Kashima, K., 1993, Diatom zonation in southern Oregon tidal marshes relative to vascular plants, foraminifera, and sea level: Journal of Coastal Research, p. 673-697.

Nelson, A. R., Sawai, Y., Jennings, A. E., Bradley, L.-A., Gerson, L., Sherrod, B. L., Sabean, J., and Horton, B. P., 2008, Great-earthquake paleogeodesy and tsunamis of the past 2000 years at Alsea Bay, central Oregon coast, USA: Quaternary Science Reviews, v. 27, no. 7-8, p. 747-768.

National Climatic Data Center, and Ncdc. "COOP Select State." *IPS - Record of Climatological Observations - Select State | IPS | National Climatic Data Center (NCDC)*, NOAA, 2019, www.ncdc.noaa.gov/IPS/coop/coop.html.

"NOAA Tides & Currents." *Station Home Page - NOAA Tides & Currents*, NOAA, 2019, tidesandcurrents.noaa.gov/stationhome.html?id=9440846.

Oemke, M. P., and Burton, T. M., 1986, Diatom colonization dynamics in a lotic system: Hydrobiologia, v. 139, no. 2, p. 153-166.

O'Donnell III, R. J., (2017). Geochemical variance of salt marshes along the cascadian subduction zone and their utility in estimating coseismic subsidence (Masters Thesis). University of North Carolina Wilmington.

Palmer, A. J., and Abbott, W. H., 1986, Diatoms as indicators of sea-level change, Sea-level Research, Springer, p. 457-487.

Passy, S. I., 2007, Diatom ecological guilds display distinct and predictable behavior along nutrient and disturbance gradients in running waters: Aquatic botany, v. 86, no. 2, p. 171-178.

Peletier, H., 1996, Long-term changes in intertidal estuarine diatom assemblages related to reduced input of organic waste: Marine Ecology Progress Series, v. 137, p. 265-271.

Peterson, C. D., and Darienzo, M. E., 1991, Discrimination of climatic, oceanic and tectonic mechanisms of cyclic marsh burial from Alsea Bay, Oregon, USA: US Geological Survey, 2331-1258.

Roegner, G.C., Hickey, B.M., Newton, J.A., Shanks, A.L., Armstrong, D.A., 2002. Wind-induced plume and bloom instrusions into Willapa Bay, Washington: Limnology and Oceanography, v. 47, no.4, p. 1033-1042.

Round, F. E., Crawford, R. M., and Mann, D. G., 1990, Diatoms: biology and morphology of the genera, Cambridge university press.

Sabean, J. A., 2004, Applications of foraminifera to detecting land level change associated with great earthquakes along the west coast of North America: Theses (Dept. of Earth Sciences)/Simon Fraser University.

Sarthou, G., Timmermans, K. R., Blain, S., and Tréguer, P., 2005, Growth physiology and fate of diatoms in the ocean: a review: Journal of sea research, v. 53, no. 1-2, p. 25-42.

Sawi, Y., 2001. Distribution of living and dead diatoms in tidal wetlands of northern Japan: relations to taphonomy: Palaeography, Palaeoclimatology, Palaeoecology, v. 173, p. 125-141.

Sawai, Y., Horton, B., and Nagumo, T., 2004a, The development of a diatom-based transfer function along the Pacific coast of eastern Hokkaido, northern Japan?an aid in paleoseismic studies of the Kuril subduction zone: Quaternary Science Reviews, v. 23, no. 23-24, p. 2467-2483.

Sawai, Y., Satake, K., Kamataki, T., Nasu, H., Shishikura, M., Atwater, B. F., Horton, B. P., Kelsey, H. M., Nagumo, T., and Yamaguchi, M., 2004b, Transient uplift after a 17th-century earthquake along the Kuril subduction zone: Science, v. 306, no. 5703, p. 1918-1920.

Sawai, Y., Horton, B. P., Kemp, A. C., Hawkes, A. D., Nagumo, T., and Nelson, A. R., 2016, Relationships between diatoms and tidal environments in Oregon and Washington, USA: Diatom research, v. 31, no. 1, p. 17-38.

Shennan, I., Innes, J. B., Long, A. J., and Zong, Y., 1994, Late Devensian and Holocene relative sealevel changes at Loch nan Eala, near Arisaig, northwest Scotland: Journal of Quaternary Science, v. 9, no. 3, p. 261-283.

Shennan, I., Long, A. J., Rutherford, M. M., Green, F. M., Innes, J. B., Lloyd, J. M., Zong, Y., and Walker, K. J., 1996, Tidal marsh stratigraphy, sea-level change and large earthquakes, i: a 5000 year record in washington, U.S.A: Quaternary Science Reviews, v. 15, no. 10, p. 1023-1059.

Shennan, I., and Hamilton, S., 2006, Coseismic and pre-seismic subsidence associated with great earthquakes in Alaska: Quaternary Science Reviews, v. 25, no. 1-2, p. 1-8.

Sherrod, B., 1999, Gradient analysis of diatom assemblages in a Puget Sound salt marsh: can such assemblages be used for quantitative paleoecological reconstructions?: Palaeogeography, Palaeoclimatology, Palaeoecology, v. 149, no. 1-4, p. 213-226.

Sladecek, V., 1986. Diatoms as indicators of organic pollution. Acta Hydrochimica et Hydrobiologica, v. 14, no. 5, p. 555–566.

Snoeijs, P., and Weckström, K., 2010, Diatoms and environmental change in large brackish-water ecosystems: The diatoms: applications for the environmental and earth sciences, no. Ed. 2, p. 287-308.

Sperazza, M., Moore, J. N., and Hendrix, M. S., 2004, High-resolution particle size analysis of naturally occurring very fine-grained sediment through laser diffractometry: Journal of Sedimentary Research, v. 74, no. 5, p. 736-743.

ter Braak, C. J., 1986, Canonical correspondence analysis: a new eigenvector technique for multivariate direct gradient analysis: Ecology, v. 67, no. 5, p. 1167-1179.

ter Braak, C. J., and Smilauer, P., 1998, CANOCO reference manual and user's guide to Canoco for Windows: software for canonical community ordination (version 4).

-, 2002, CANOCO reference manual and CanoDraw for Windows user's guide: software for canonical community ordination (version 4.5): www. canoco. com.

Theriot, E., 1992, Clusters, species concepts, and morphological evolution of diatoms: Systematic biology, v. 41, no. 2, p. 141-157.

Troelstra, S.R., 1997. Saltmarsh foraminifera from the Great Marshes: Palaeogeography, Palaeoclimatology, Palaeoecology, v. 130, p. 81-112.

Underwood, G. J., Phillips, J., and Saunders, K., 1998, Distribution of estuarine benthic diatom species along salinity and nutrient gradients: European Journal of Phycology, v. 33, no. 2, p. 173-183.

van Togeren, O.F.R., 1987. Cluster analysis. In: *Data analysis in community and landscape ecology* (R.H.G. Jongman, C.J.F. ter Braak & O.F.R. van Tongeren, eds), 174-212. AC Wageningen.

Vos, P. C., and de Wolf, H., 1993, Diatoms as a tool for reconstructing sedimentary environments in coastal wetlands; methodological aspects: Hydrobiologia, v. 269, no. 1, p. 285-296.

Watcham, E. P., Shennan, I., and Barlow, N. L., 2013, Scale considerations in using diatoms as indicators of sea-level change: lessons from Alaska: Journal of Quaternary Science, v. 28, no. 2, p. 165-179.

Whiting, M. C., and McIntire, C. D., 1985, An investigation of distributional patterns in the diatom flora of Netarts Bay, Oregon, by correspondence analysis 1: Journal of Phycology, v. 21, no. 4, p. 655-661.

Witkowski A (2000) Diatom flora of marine coasts. In: Lange-Bertalot H (ed) *Iconagraphia Diatomologica, v.7*. Germany: A.R.G. Gantner.

Woodroffe, S.A., and Long, A.J., 2010. Reconstructing recent relative sea-level changes in West Greenland: Local diatom-based transfer functions are superior to regional models: Quaternary International, v. 221, no. 1-2, p. 91-103.

Zong, Y., 1997. Mid- and late-Holocene sea-level changes in Roudsea Marsh, northwest England: a diatom biostratigraphical investigation: The Holocene, v. 3, no. 3, p. 311-323.

Zong, Y., and Horton, B. P., 1998, Diatom zones across intertidal flats and coastal saltmarshes in Britain: Diatom Research, v. 13, no. 2, p. 375-394.

-, 1999, Diatom-based tidal-level transfer functions as an aid in reconstructing Quaternary history of sea-level movements in the UK: Journal of Quaternary Science, v. 14, no. 2, p. 153-167.

Zong, Y., Shennan, I., Combellick, R., Hamilton, S., and Rutherford, M., 2003, Microfossil evidence for land movements associated with the AD 1964 Alaska earthquake: The Holocene, v. 13, no. 1, p. 7-20.

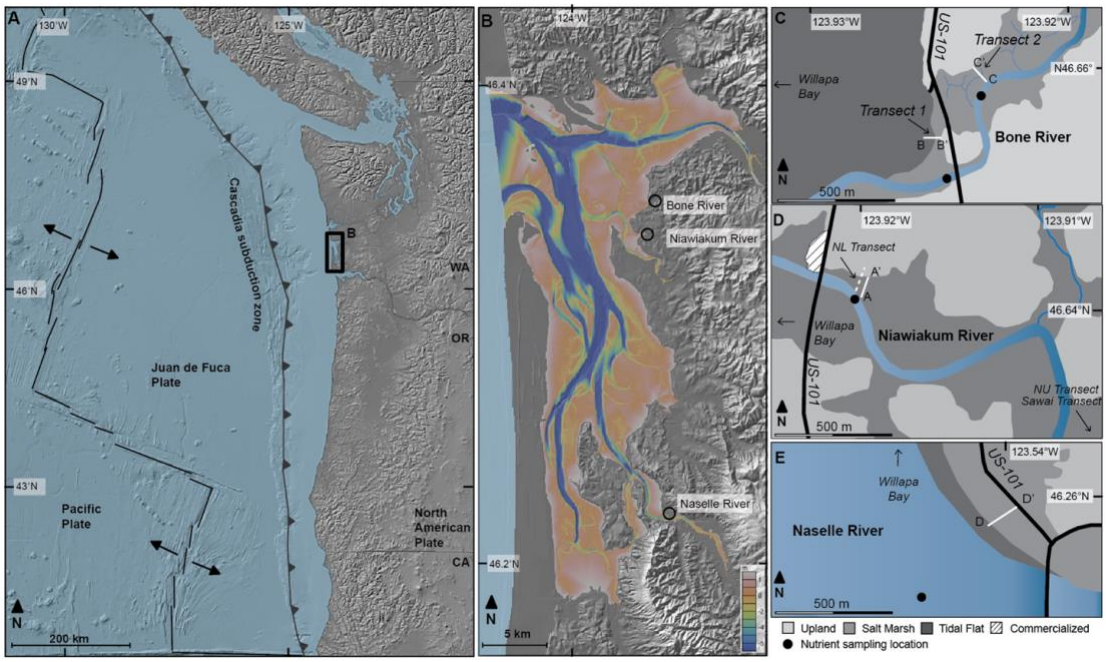

Figure 1. (A) Map of the Cascadia subduction zone and its major features. (B) Bathymetry of Willapa Bay, WA (50 m resolution; NOAA, 2016) with sampling sites marked by circles. (C) Bone River with sampled transects marked with solid white lines. (D) Niawiakum River with sampled transect marked with a solid white line and the Lower Niawiakum transect (Hemphill-Haley, 1995b) marked with a dashed white line. The Upper Niawiakum transect of Hemphill-Haley (1995b) and Sawai et al. (2016) are marked by arrows indicating its location farther upstream. (D) Naselle River with sampled transect marked with a solid white line.

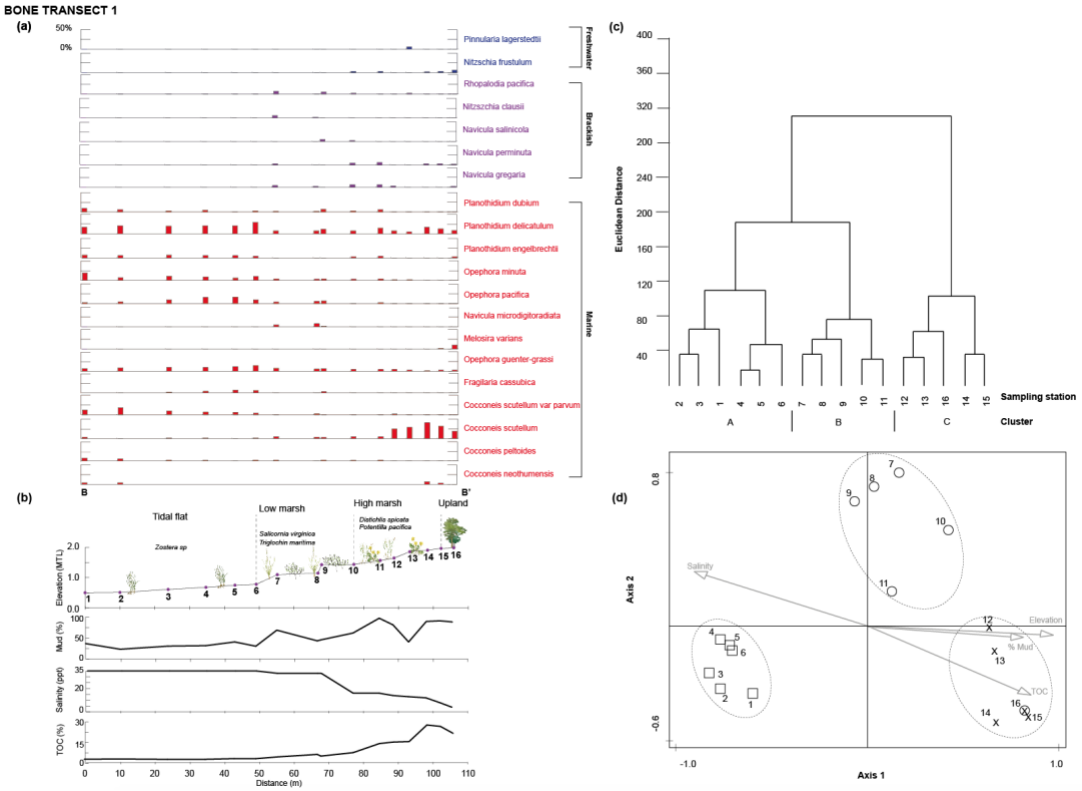

Figure 2. Bone River Transect 1. (A) Sampled transect showing the distribution of dominant diatoms (> 5% maximum abundance in at least one sample) with elevation. Diatoms are separated based on their salinity preferences (blue: freshwater; purple: brackish; red: marine). (B) Sampled transect showing the location of the sampling stations and major vegetation separated by flora zones relative to distance and elevation (m MTL). The % sand, salinity (ppt), and TOC of each sampling station is plotted relative to distance. (C) Results of hierarchical cluster analysis with (D) PCA results shown below. Station symbols indicate their sampling location (square: tidal flat; circle: low marsh; cross: high marsh).

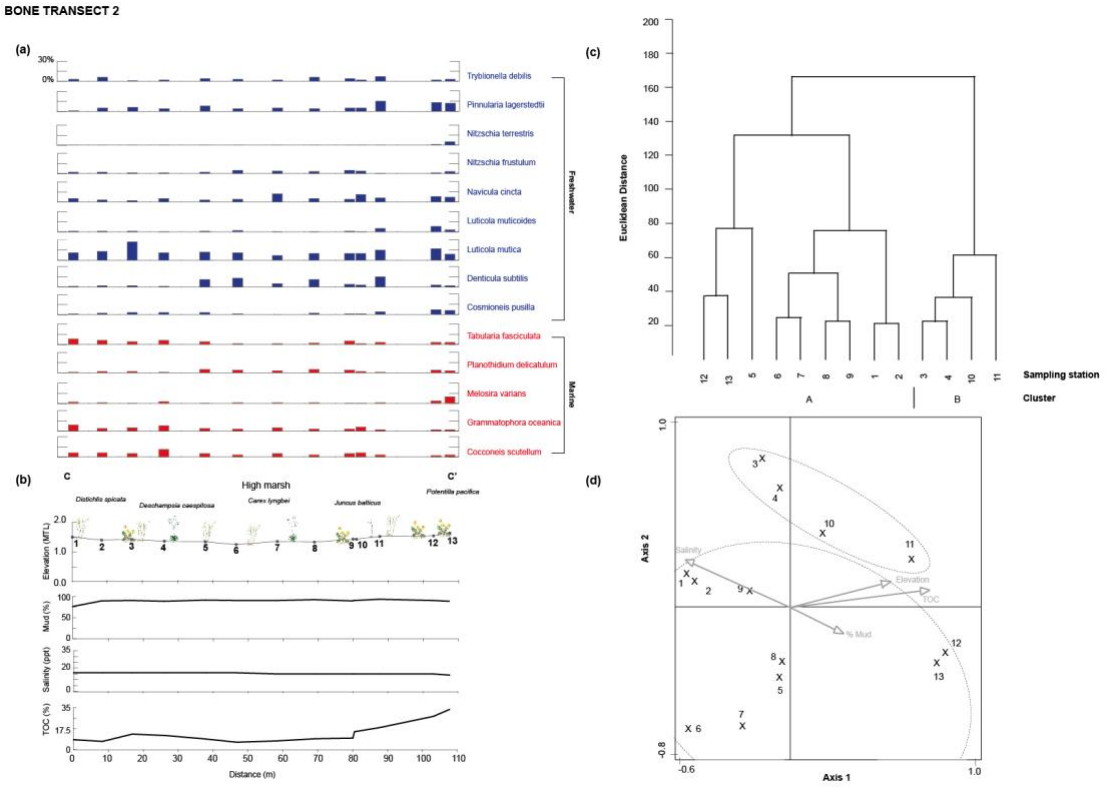

Figure 3. Bone River Transect 2. (A) Sampled transect showing the distribution of dominant diatoms (> 5% maximum abundance in at least one sample) with elevation. Diatoms are separated based on their salinity preferences (blue: freshwater; red: marine). (B) Sampled transect showing the location of the sampling stations and major vegetation separated by flora zones relative to distance and elevation (m MTL). The % sand, salinity (ppt), and TOC of each sampling station is plotted relative to distance. (C) Results of hierarchical cluster analysis with (D) PCA results shown below. Station symbols indicate their sampling location (cross: high marsh).

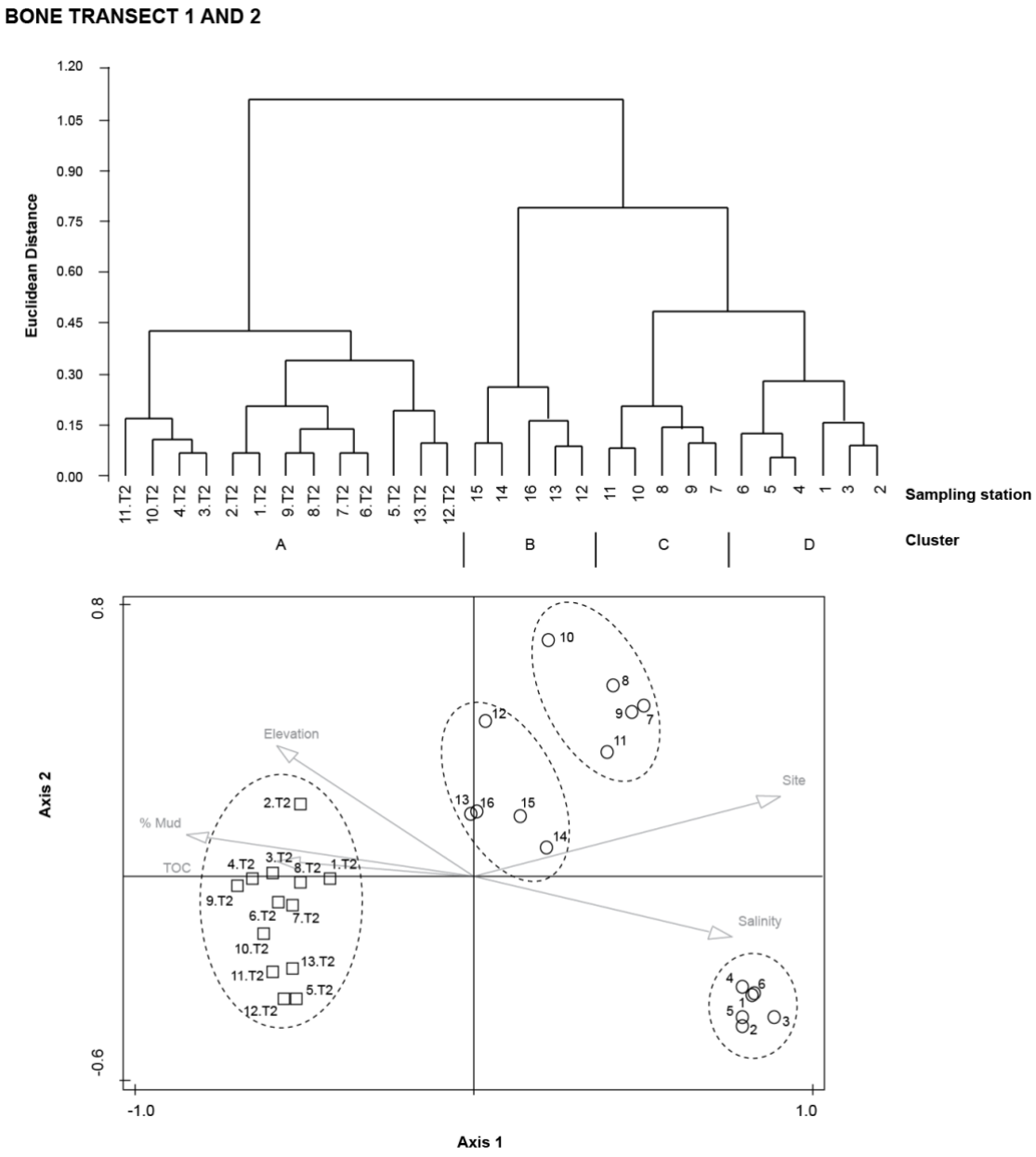

Figure 4. (Top) Results of hierarchical cluster analysis and (Bottom) PCA of Bone River Transect 1 and 2 (samples labeled with extension .T2).

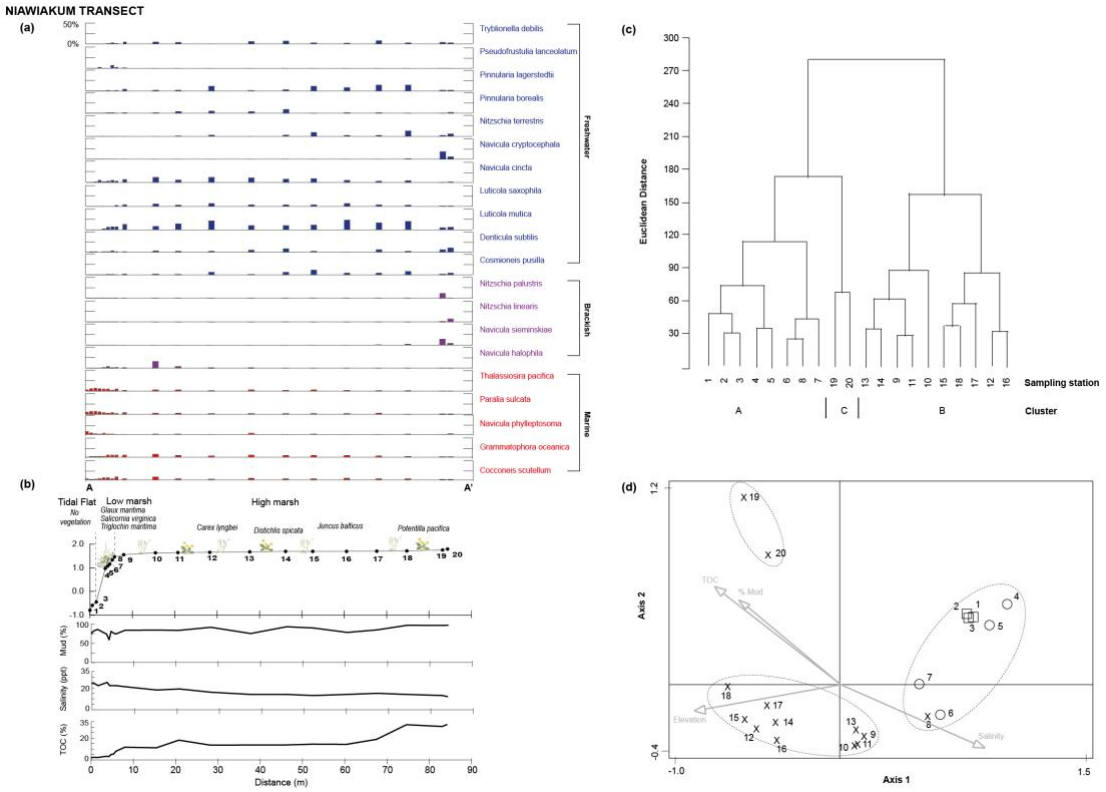

Figure 5. Niawiakum River Transect. (A) Sampled transect showing the distribution of dominant diatoms (> 5% maximum abundance in at least one sample) with elevation. Diatoms are separated based on their salinity preferences (blue: freshwater; purple: brackish; red: marine). (B) Sampled transect showing the location of the sampling stations and major vegetation separated by flora zones relative to distance and elevation (m MTL). The % sand, salinity (ppt), and TOC of each sampling station is plotted relative to distance. (C) Results of hierarchical cluster analysis with (D) PCA results shown below. Station symbols indicate their sampling location (square: tidal flat; circle: low marsh; cross: high marsh).

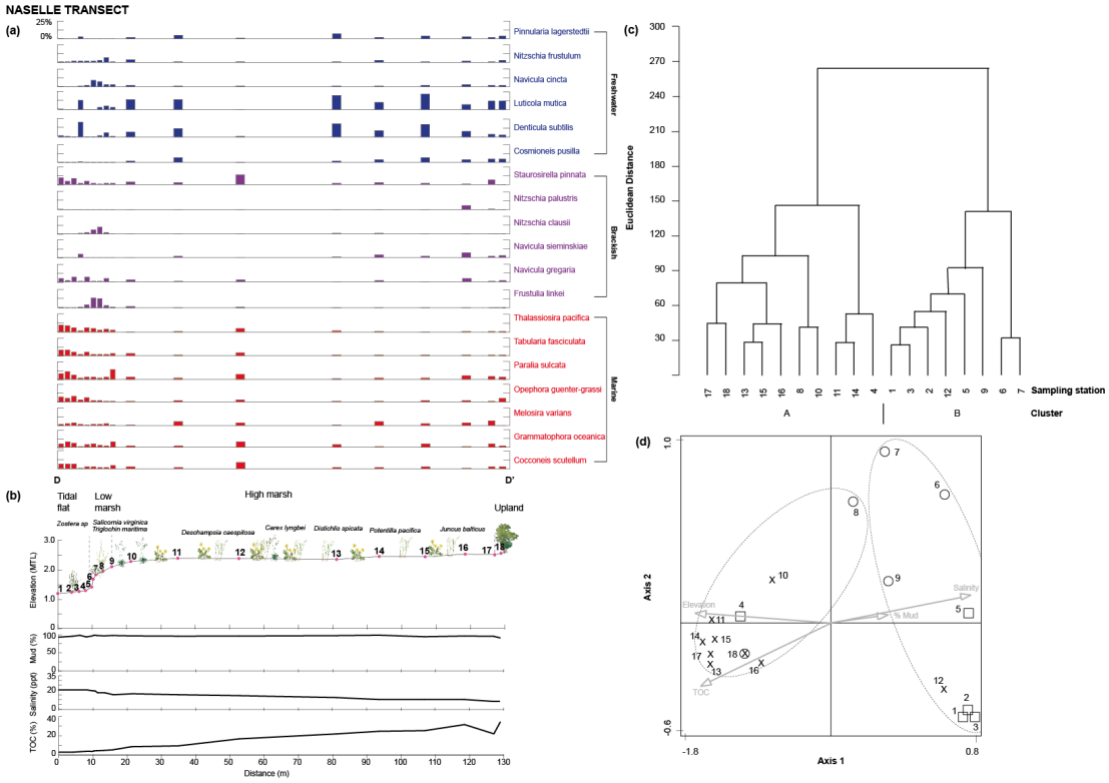

Figure 6. Naselle River Transect. (A) Sampled transect showing the distribution of dominant diatoms (> 5% maximum abundance in at least one sample) with elevation. Diatoms are separated based on their salinity preferences (blue: freshwater; purple: brackish; red: marine). (B) Sampled transect showing the location of the sampling stations and major vegetation separated by flora zones relative to distance and elevation (m MTL). The % sand, salinity (ppt), and TOC of each sampling station is plotted relative to distance. (C) Results of hierarchical cluster analysis with (D) PCA results shown below. Station symbols indicate their sampling location (square: tidal flat; circle: low marsh; cross: high marsh; crossed circle: upland).

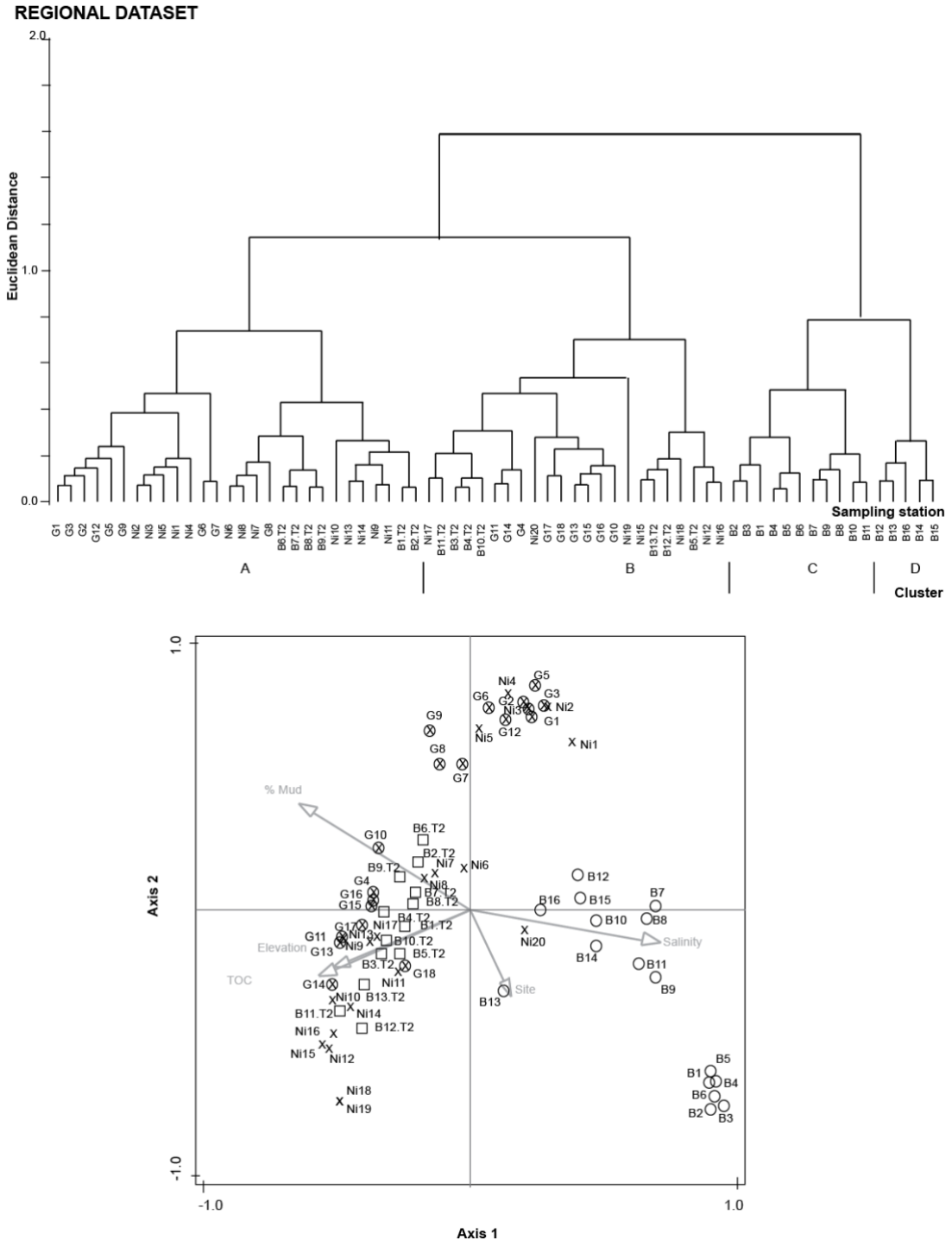

Figure 7. (Top) Results of hierarchical cluster analysis and (Bottom) PCA of the regional dataset. The symbols indicate individual transects (circle: Bone River Transect 1; square: Bone River Transect 2; cross: Niawiakum River Transect; crossed circle: Naselle River Transect).

TABLE 1. Nutrient concentrations from Willapa Bay, WA

Location	Nitrate-Nitrite (µM)	Ammonium (µM)	Orthophosphate (µM)	Silicate (µM)
Bone River Transect 1	2.10	8.60	1.20	29.3
Bone River Transect 2	2.50	3.00	1.40	33.6
Niawiakum River Transect	1.50	3.10	0.70	18.5
Naselle River Transect	2.30	2.40	1.10	25.8

TABLE 2. Summary PCA results

Sample	Axis 1 Eigenvalue	Axis 2 Eigenvalue	Axis 3 Eigenvalue	Axis 4 Eigenvalue
Bone River Transect 1	0.38	0.18	0.09	0.06
Bone River Transect 2	0.22	0.20	0.12	0.08
Bone Transects Combined	0.32	0.11	0.07	0.05
Niawiakum River Transect	0.34	0.15	0.10	0.06
Naselle River Transect	0.35	0.17	0.07	0.06
Regional Dataset	0.25	0.12	0.08	0.05

TABLE 3. Summary RDA results

Bone River Transect 1		***Niawiakum River Transect***	
Variable	*Contribution (%)*	*Variable*	*Contribution (%)*
Elevation	35	Elevation	28
TOC	14	Salinity	14
% Mud	7	TOC	6
Salinity	6	% Mud	4
Bone River Transect 2		***Naselle River Transect***	
Variable	*Contribution (%)*	*Variable*	*Contribution (%)*
TOC	20	Salinity	21
Salinity	10	Elevation	8
Elevation	8	% Mud	6
% Mud	6	TOC	5
Bone Transects Combined		***Regional Dataset***	
Variable	*Contribution (%)*	*Variable*	*Contribution (%)*
Site	28	Salinity	15
Elevation	12	Site	7
TOC	6	Elevation	5
Salinity	5	TOC	4
% Mud	3	% Mud	3

Chapter 3: Quantifying coastal subsidence during megathrust earthquakes at the Cascadia subduction zone with a Bayesian diatom transfer function

Abstract

Estimates of coastal subsidence derived from microfossils (e.g., diatoms, foraminifera) within stratigraphic records are the most precise means to reconstruct deformation during past megathrust ruptures, but the application of diatoms has been limited at Cascadia due to a no modern analogue problem. Here, the application of an established transfer function (weighted-averaging partial least squares) developed from a training set of 67 samples from Willapa Bay, WA to a stratigraphic sequence of earthquake subsidence events found that all 77 fossil samples had a poor modern analogues. To improve the dissimilarity between modern and fossil samples, we used a hierarchical clustering method to identify 12 diatom groups with similar abundance and distributions with elevation. We subsequently developed a new Bayesian diatom transfer function (BDTF) that integrates the grouped species response curves (positive and negative linear, unimodal, bimodal and multimodal) and lithology prior information about each sample to improve the precision of reconstructed earthquake subsidence. We apply the BDTF to a stratigraphic sequence at the Redtail locality of Willapa Bay where six, mud-over-peat contacts have been inferred to record subsidence during great Cascadia earthquakes (Atwater and Hemphill-Haley, 1997). The grouping of species increased the proportion of good analogue samples from 0 to 21%, which were predominantly from above and below the stratigraphic contact created by subsidence during the 1700 CE earthquake (Contact 1) and the next older contact

(Contact 2, 1130 to 1350 yrs CE). The BDTF produced subsidence estimates of 0.46 m ± 0.33 m and 0.51 m ± 0.34 m, respectively. No matching analogues were found for older Contacts 3, 4, 5, and 6, which suggests that the modern intertidal samples of the training set do not represent the range of paleoenvironmental conditions in Willapa Bay from ~1400 to 3500 yrs CE.

1. Introduction

Despite the fact that intertidal sediments fringing estuaries at the Cascadia subduction zone (CSZ) harbor a record of megathrust earthquakes during the past 5000 years (e.g., Atwater, 1992; Darienzo and Peterson, 1994; Atwater and Hemphill-Haley, 1997; Kelsey et al., 2002; Witter et al., 2003; Nelson et al., 1996a; Nelson et al., 2006; Milker et al., 2016), Cascadia has not experienced rupture during the instrumental or regional historical period (e.g., Atwater, 1987; Clague, 1997; Wang and Tréhu, 2016). Intertidal stratigraphic sequences of mud-over-peat contacts in coastal wetlands record land-level change during earthquake deformation cycles with recurrence intervals of centuries (e.g., Shennan et al., 1996; Nelson et al., 2006; Atwater et al., 2004). The earthquake deformation cycle is characterized by strain accumulation of the subduction zone during the interseismic period when the coastline slowly rises, resulting in gradual relative sea-level (RSL) fall (e.g., Thatcher, 1984; Shennan et al., 1996; Bourgeois, 2006). Coseismic slip releases this strain during an earthquake, causing instantaneous subsidence and rapid RSL rise. The preservation of these mud-over-peat contacts is largely the outcome of the middle to late Holocene regional relative sea-level (RSL) rise of 0.7 to 1.5 mm/yr (Engelhart et al., 2015; Yousefi et al., 2018) that creates sediment accommodation space (Atwater, 1987; Long and Shennan, 1994; Kelsey et al., 2015; Dura et al. 2016).

Diatoms are one of the most useful and widely applicable environmental proxies for the reconstruction of land-level change associated with megathrust earthquakes along the CSZ (e.g., Hemphill-Haley, 1995a; Shennan et al., 1996) because they thrive in nearly all aqueous environments and the siliceous valves of diatoms aid in their

preservation and identification in sediment long after burial (Admiraal, 1984; Palmer and Abbott, 1986; Hemphill-Haley, 1995b; Dura et al., 2016). Diatom assemblages in intertidal environments are commonly vertically zoned with respect to the tidal frame, making them suitable for precise estimates of the tidal elevation at which they were deposited (e.g., Shennan et al., 1996; Hemphill-Haley, 1995a; Zong and Horton, 1999; Sherrod, 2001; Sawai et al., 2004).

Estimates of coastal subsidence derived from microfossils (e.g., diatoms, foraminifera) preserved within intertidal stratigraphic sequences of Cascadia allow us to reconstruct site-specific, land-level change during earth deformation cycles (e.g., Jennings and Nelson, 1992; Nelson and Kashima, 1993; Hemphill-Haley, 1995a, b; Sawai et al., 2004a, b; Shennan and Hamilton, 2006; Hawkes et al., 2011; Milker et al., 2016). The development and application of statistically based microfossil analysis (transfer function) of the rapid change in tidal environment across mud-over-peat intertidal sequences in Cascadia provided fully quantitative estimates of coseismic subsidence with sample-specific errors (e.g., Guilbault et al., 1995, 1996; Shennan et al., 1996, 1998; Hawkes et al., 2010; Milker et al., 2016). To estimate values of subsidence using a transfer function, the contemporary response of the species of microorganisms to elevation with respect to the tidal frame is modeled (Zong and Horton, 1998). This involves a contemporary 'training set' of species from a range of environments that will provide modern analogues for fossil assemblages (e.g., Zong and Horton, 1999; Zong et al., 2003; Horton et al., 2006; Sawai et al., 2004; Watcham et al., 2013).

Diatom-based transfer functions have been applied to fossil data to produce quantitative estimates of coseismic subsidence from Alaska (Zong et al., 2003; Hamilton and Shennan, 2005a, b; Shennan and Hamilton, 2006; Watcham et al., 2013), Chile (Garrett

et al., 2013; Hocking et al., 2017), and Japan (Sawai et al., 2004a, b). However, the use of a diatom transfer function in Cascadia have been hindered by the absence of modern analogues for fossil assemblages, which has led to unreliable estimates of subsidence (e.g., Nelson et al., 2008). In this study, we address current transfer function limitations in Cascadia with the development and application of a new Bayesian diatom transfer function. We illustrate the problem of no modern analogues using a standard transfer function (weighted-averaging partial least squares; WA-PLS) developed from a training set of 67 samples from Willapa Bay, Washington. We subsequently develop a novel Bayesian diatom transfer function that combines species with similar distributions across elevation and allows for the addition of prior lithologic information, which resulted in reduced uncertainty. The grouping of species increased the proportion of good analogues from 0 to 21%. We apply the transfer functions to an intertidal stratigraphic sequence taken from the Redtail locality of Willapa Bay (Figure 1) where six, mud-over-peat contacts have been inferred to record subsidence during great Cascadia earthquakes (Atwater and Hemphill-Haley, 1997). Reconstructions from the Bayesian diatom transfer function resulted in subsidence estimates for the six earthquakes that ranged from 0.37 to 0.51 m (± 0.33 to 0.37 m).

2. Study Area

2.1 Tectonic Setting

The CSZ extends from northern California to British Columbia and includes subduction of the Explorer, Gorda, and Juan de Fuca plates underneath the North American plate (e.g., Flück et al., 1997; Miller et al., 2001; DeMets et al., 2010). In the Pacific Northwest, the oblique subduction of the Juan de Fuca plate is occurring at a rate of

~30 to 42 mm/yr (DeMets et al., 2010). The accurate assessment of Cascadia's regional earthquake hazards requires well-constrained, realistic geophysical models of upper-plate deformation both during (coseismic) and in-between (interseismic) great ($M_w \geq$ 8.0) megathrust earthquakes (Wang and Tréhu, 2016; Gomberg and Ludwig, 2017; Ludwig et al., 2018). However, current models of upper-plate deformation at the CSZ are unconstrained by the lack of instrumental measurements or observational accounts that span more than a fraction of the earthquake deformation cycle (Wang and Tréhu, 2016).

Geologic records of mud-over-peat contacts in Cascadia intertidal environments (e.g., Nelson et al., 1996b; Atwater and Hemphill-Haley, 1997; Kelsey et al., 1998) and offshore turbidites (e.g., Goldfinger et al., 2012) are evidence for multiple, great megathrust earthquakes. Paleoseismology and Japanese historical studies identified the most recent megathrust earthquake, which occurred in 1700 CE and produced an estimated ~M_w 9.0 earthquake (as inferred from the accompanying tsunami) that ruptured the entire length of the subduction zone (e.g., Nelson et al., 1995; Satake et al., 1996; Clague, 1997; Satake et al., 2003). Since then, the CSZ has been in a state of interseismic strain accumulation and questions remain regarding the along-strike variation of interseismic locking and heterogeneity of slip behavior (e.g., Flück et al., 1997; Wang et al., 2003; McCaffrey et al., 2013; Wang and Tréhu, 2016).

2.2 Willapa Bay

Willapa Bay is an estuary located in southwestern Washington. The bay formed as a result of river valley flooding caused by sea-level rise after the Last Glacial Maximum (e.g., Engelhart et al., 2015) and has subsequently experienced minimal human and

industrial disturbance (US Fish and Wildlife, 2019; WA DNR, 2019). Tides in Willapa Bay display a Great Diurnal range (difference of mean higher high water and mean lower low water) of 2.8 m that increases to 3.3 m in the southern portion of the bay (NCDC, 2019). The vascular plants in wetlands fringing Willapa Bay display the following intertidal zonation: tidal flat (no vegetation or sparse amounts of *Zostera sp*), low marsh (*Glaux maritima, Jaumea carnosa, Salicornia virginica, Spartina alterniflora,* and *Triglochin maritima*), high marsh (*Carex lyngbei, Deschampsia caespitosa, Distichlis spicata*, *Juncus balticus, Potentilla pacifica*), and forested upland (e.g., *Picea sitchensis* and *Pyrus fusca*; Hemphill-Haley, 1995a; Atwater and Hemphill-Haley, 1997; Cooke, 1997).

Paleoseismological studies in Willapa Bay have uncovered litho- and bio-stratigraphic evidence of coseismic subsidence during multiple earthquakes (Atwater, 1987; Atwater and Yamaguchi, 1991; Hemphill-Haley, 1995a, b; Atwater and Hemphill-Haley, 1997; Sabean, 2004). Our study area is at the Redtail locality along the Niawiakum River in Willapa Bay, Washington, where Hemphill-Haley (1995a) and Atwater and Hemphill-Haley (1997) developed a 3500-yr chronology of six mud-over peat contacts at the tops of six wetland soils (Y, U, S, N, L, and J) correlated with earthquake subsidence of > 1 m (Figure 2) but with no formal error assessment. The subsidence estimates were based on riverbank stratigraphy that revealed a pattern of high marsh and spruce swamp peat sharply overlain by tidal mud coincident with abrupt changes in diatom assemblages from high marsh to intertidal or subtidal flat environments.

3. Methods

3.1 Sampling and elevation measurement

We described the color, thickness, characteristics of upper and lower contacts, and proportions of sand, silt, and organic material for each stratigraphic unit at the Redtail locality using the nomenclature of Troels-Smith (1955). In the field, we correlated our mud-over-peat contacts with the six contacts at the tops of the wetland soils described by Atwater and Hemphill-Haley (1997). Using a gouge corer (100 mm diameter), we collected a 4-m long sediment core from a riverbank section of the Redtail locality at the Niawiakum River (Figure 1; 1997). The sample was kept refrigerated until transportation to the laboratory. To determine the elevation of the sampled monolith, we measured elevation using a Real Time Kinematic-Global Positioning System (RTK-GPS). Elevations were surveyed to geodetic benchmarks and referenced to the North American vertical datum (NAVD88). We used VDatum to tie measured elevation to mean tide level (VDatum, accessed 2019).

3.2 Dating

We supplemented the radiocarbon dating of Atwater and Hemphill-Haley (1997) at the Redtail locality by sampling the core for additional radiocarbon ages using the methods of Kemp et al. (2013). Plant macrofossils were selected from 3- to 5-cm-thick slices directly above or below mud-over-peat contacts from the sediment core in an attempt to obtain maximum and minimum ages for subsidence marked by each contact. The cut slices were placed on a 0.5-mm sieve and examined under a microscope, carefully searching for detrital organic material or growth position rooted plant structures. (Table

1). Three samples were submitted to the National Ocean Sciences Accelerator Mass Spectrometry (NOSAMS) facility for AMS ^{14}C dating (Table 1). However, because the three samples were all detrital our ages are inconclusive indicators of the times of sediment deposition.

3.3 Laboratory analysis

To characterize the substrate and provide lithologic prior information for the Bayesian transfer function we sampled the core for grain-size and loss-on-ignition (LOI) analyses at depth intervals of 1 cm near lithologic contacts and every 5 cm in the continuous and homogeneous sediment (Cahill et al.., 2016; Kemp et al., 2018). Samples for grain-size analysis were placed in a 25 mL plastic Falcon tube and organic matter was removed using 30% concentration H_2O_2 prior to measurement using a Malvern Mastersizer 3000 laser particle-size analyzer (Sperazza et al., 2004; Donato 2009). We report the mean grain size (Φ) for each sample. We performed LOI following methods outlined by Plater et al. (2015) by placing samples into crucibles and weighing and burning the sample in a muffle furnace at 475° C for three hours (2015).

3.4 Diatom analysis

We sampled the core at depth intervals of 1 cm near lithologic contacts and every 5-25 cm in the continuous and homogeneous sediment for diatom analysis. We prepared diatoms for analysis following the methods of Palmer and Abbott (1986). In the laboratory, disposable plastic syringes removed 1 cm^3 of sediment from each sample for diatom analysis. The sediment was placed in a 25 mL plastic Falcon tube with 30% concentration H_2O_2 to remove all organic material from the sample. We dripped, dried, and mounted the diatoms onto a glass slide using Naphrax. For each sample, 400 valves

were counted using light microscopy under oil immersion at 1000x magnification. Diatoms were identified to species level using the references of Krammer and Lange-Bertalot (1986, 1988, 1991a, b), and Witkowski et al. (2001).

3.5 Quantifying coseismic subsidence

Quantifying coseismic subsidence using a transfer function is not dependent on a singular method. Determining the appropriate transfer function requires an assessment of the species-environment response of the dataset whereby either species abundance and distribution is driven by an environmental variable (classical approach) or the environmental variable is driven by species abundance and distribution (inverse approach; e.g., Birks, 1995). Previous studies have employed a variety of regression-based transfer function techniques (e.g., Weighted averaging, Partial least squares, Weighted averaging partial least squares, etc.) that uses a fixed species response (e.g., unimodal) to reconstruct past RSL (e.g., Guilbault et al., 1995; Horton et al., 1999; Edwards and Horton, 2000; Sawai et al., 2004). The recent development of a Bayesian method provided an alternative approach to reconstructing RSL that allows for the species-environment response of the dataset to be flexible (nonunimodal) for all species and the addition of prior information from other proxies (e.g., $\delta_{13}C$; Cahill et al., 2016).

Irrespective of the method, using a transfer function to reconstruct RSL is a three stage process involving: (1) development of a training set that pairs observed biological data (i.e., diatom assemblages) to the environmental variable of interest (i.e., elevation); (2) formalizing of the relationship between diatoms and elevation using an appropriate numerical technique (i.e., transfer function); and (3) application of the transfer function

to fossil diatoms in a sediment core to reconstruct past elevation (Horton and Edwards, 2006).

We developed a transfer function from a training set consisting of 367 taxa from 67 samples collected from shore-perpendicular transects from three Willapa Bay tidal marshes: the Bone River, Niawiakum River, and Naselle River (Figure 1; Chapter 2). The sampled transects ranged in elevation from the tidal flat to forested upland and captured the range of diatoms found in marine (e.g., *Cocconeis scutellum var parva*, *Grammatophora oceanica*, and *Opephora pacifica*), brackish (e.g., *Frustulia linkei*, *Navicula halophila*, and *Navicula gregaria*), and freshwater environments (e.g., *Navicula cincta*, *Nitzschia terrestris*, and *Pinnularia lagerstedtii*). Hierarchical clustering and ordination of the training set showed that elevation is a statistically significant (p value < 0.01) environmental factor that explains the variance of diatom assemblage distribution, explaining 8 to 35% of the variance at individual transects and 5% for the regional dataset of all modern samples (Chapter 2: Table 3), that potentially allows for its use in reconstructing elevation (e.g., Sherrod, 1999; Sawai et al., 2004a, b; Woodroffe and Long, 2010). Following Sawai et al. (2004a, b), rare species with a maximum abundance of < 2% in a single sample were removed prior to the development of the transfer function resulting in a reduction of diatoms to 153 species across 45 genera.

We converted the measured elevations of each sampling station (h_n) to a standard water level index ($SWLI_n$) value to allow for the assimilation of a modern training set that consisted of sites with differing tidal ranges (Horton et al., 1999):

$$SWLI_n = \frac{100(h_n - h_{MTL})}{h_{MHHW} - h_{MTL}} + 100$$

where n is the sample, h_{MTL} is the elevation of MTL, and h_{MHHW} is the elevation of mean higher high water (MHHW). The resulting SWLI values are relative to the same datum where MTL is 100 and MHHW is 200. To determine paleoelevation, we perform a back transformation of SWLI values to m (MTL) by rearranging the equation.

3.5.1 Weighted-averaging partial least squares transfer function

We developed a weighted-averaging partial least squares (WA-PLS) transfer function using the software C2 where species abundance is expressed as a percentage (Juggins, 2011) to illustrate the current limitations of an established diatom transfer function approach in Cascadia. The WA-PLS transfer function uses the species and their abundance to quantify the ecological optima (i.e., elevation where an individual taxa is most abundant) and tolerance (i.e., elevation range over which the species is found) from which we can reconstruct the paleoelevation of the fossil sample using the weighted average of the species optima (Birks, 1995; Juggins and Birks, 2012). We ran an initial transfer function on the modern training set to remove samples identified to be ecological outliers based on having a residual greater than the standard deviation of SWLI (Gasse et al., 1995; Horton et al., 1999). The performance of the WA-PLS transfer function was measured using bootstrap cross validation (n=1000) and evaluated using the root-mean square error of prediction (RMSEP) and squared correlation (r^2) of the observed versus predicted values.

The transfer function calculates statistics for five components from which the number of components is chosen for reconstruction (Juggins, 2011). The selection of components is based on the lowest number of components that produces reasonable RMSEP and r^2 values (e.g., Birks, 1995; Horton et al., 2006; Barlow et al., 2013).

3.5.2 Bayesian diatom transfer function

We developed the first, diatom-based Bayesian transfer function (BDTF) for RSL reconstructions to address the limitations of established diatom transfer functions. Prior to the development of the BDTF, we performed a dimension reduction (grouping) technique to address limitations caused by no modern analogues and to improve the computational efficiency of the BDTF. For each species we found the mean and standard deviation of abundance as well as the elevations corresponding to the maximum abundance of four abundance percentiles (2.5%, 16%, 84%, and 97.5%). These statistical summaries of the modern data provided a set of variables that allowed for grouping the species based on their similarities with respect to abundance and their distribution along the elevational gradient (Figure 3). A hierarchical clustering method was applied to these variables to create 12 groups of species (Figure 4). The same groupings were applied to the fossil species.

Following the approach of Cahill et al. (2016), we developed a BDTF where species abundance is expressed as counts. The BDTF uses a penalized spline model to describe the relationship between the grouped diatom species and tidal elevation. Unlike the WA-PLS transfer function, this approach allows for multi- and non-unimodal group response curves. The performance of the BDTF was measured using 10-fold cross-validation.

To reduce uncertainty in the reconstruction, we provided independent environmental data of well-established sea-level proxies as prior information in the BDTF (Cahill et al., 2016). Adapting the method of Kemp et al. (2018), we used sediment lithology

(Troels Smith, 1955), stratigraphic context, and laboratory analyses (grain size and LOI) to attach the following priors to the fossil samples:

1. Mud or rooted mud with mean grain size ranging from 4.33 to 6.90 Φ and LOI ranging from 3 to 34% as having formed in the tidal flat or low marsh environment with a paleoelevation of between mean low water to mean higher high water
2. Organic-rich silt (e.g., peaty mud, muddy peat, or peat) with mean grain size ranging from 4.22 to 7.84 Φ and LOI ranging from 5 to 73% as having formed in the high marsh environment with a paleoelevation above mean high water.

We applied threshold values consistent with observations of other RSL reconstruction studies. For example, Shennan et al. (1995) used an LOI of 19 to 28% to define the low marsh and an LOI of >28 to 72% to define the zone between the high marsh and highest astronomical tide. Similarly, observations of grain size in tidal wetlands show a shift of sand-dominated sediments (-1 to 4 Φ) in the tidal flat that transition to silt-dominated sediments (4 to 8 Φ) with increasing elevation (e.g., Zong and Horton, 1999; Sawai et al., 2004b; Yang et al., 2008).

3.5.3 Paleoelevation reconstruction and assessment

We applied the WA-PLS and BDTF transfer function to fossil diatom assemblages in the stratigraphic sequence at Redtail to reconstruct the elevation at which the fossil diatoms lived with a sample specific error of 1 σ (Juggins and Birks, 2012; Cahill et al., 2016).

We follow the methods of Hawkes et al. (2011) to calculate coseismic land-level change and its accompanying uncertainty. We calculate coseismic land-level change (E_{change}) by subtracting the pre-seismic paleoelevation (E_{pre}) from the post-seismic paleoelevation (E_{post}):

$$E_{change} = E_{pre} - E_{post}$$

and determine the uncertainty using the following equation:

$$uncertainty = \sqrt{(Error_{pre}^2 + Error_{post}^2)}$$

Where $Error_{pre}^2$ is the sample-specific, pre-seismic elevation error and the $Error_{post}^2$ is sample-specific, post-seismic elevation error provided by the WA-PLS transfer function. To evaluate the ability of the dimension reduction approach to address the issue of no modern analogues, we used the modern analogue technique (MAT), which applies a chi-squared distance measure to quantify the similarity between each fossil sample and the modern training set (Birks, 1995). Fossil samples with a minimum distance coefficient below the 5th percentile are considered to have a good modern analogue whereas a coefficient above the 20th percentile of the modern training set are considered to have a poor analogue (Birks, 1995; Horton and Edwards, 2006; Kemp et al., 2009; Hamilton and Shennan, 2005a). We apply the 20th percentile of the modern training set as a threshold between good and poor analogue for our reconstruction.

4. Results

4.1 Transfer function

4.1.2 BDTF group-response curves

We identified 12 diatoms groups from the hierarchical clustering method (Figure 4). Using the abundance (counts) of the grouped diatoms across elevation (SWLI) from the modern training set, the group response curves (mean with a 95% credible interval) display the probability of the grouped species being present at a given elevation (Figure 5).

Group 1: unimodal relationship with elevation and a maximum probability of occurrence of 0.04 at 187 SWLI (Figure 5). Species in Group 1 are a mixture of marine (e.g., *Gyrosigma obscurum*), brackish (e.g., *Caloneis westii*), and freshwater (e.g., *Staurosirella construens*) species (Figure 4). The probability of occurrence of species in Group 1 is very low with many species recording 0 at sampling stations across all the SWLI gradient.

Group 2: bimodal distribution with elevation and a maximum probability of occurrence of 0.03 at 201 SWLI (Figure 5). Species in Group 2 are a mixture of marine (e.g., *Cocconeis palcentula var euglypta*), brackish (e.g., *Gyrosigma eximium*), and freshwater (e.g., *Nitzschia fasciculata*) species (Figure 4). The probability of occurrence of species in Group 2 is low especially with SWLI values less than 170 where there are many species recording 0.

Group 3: bimodal distribution with elevation and a maximum probability of occurrence of 0.09 at 187 SWLI (Figure 5). Species in Group 3 are a mixture of marine (e.g., *Delphineis surirella*), brackish (e.g., *Berekelya rutilans*), and freshwater (e.g., *Navicula radiosa*) species (Figure 4). The probability of occurrence of species in Group 3 is very low with SWLI values less than 155.

Group 4: includes species with very low abundances at all elevations (Figure 5). Species in Group 4 are a mixture of marine (e.g., *Mastogolia smithii*), brackish (e.g., *Scolioneis tumida*), and freshwater (e.g., *Pinnularia obscura*) species (Figure 4).

Group 5: bimodal distribution with elevation and a maximum probability of occurrence of 0.23 at 176 SWLI (Figure 5). Species in Group 5 are predominantly marine (e.g., *Cocconeis placentula*, *Melosira moniliformis*, and *Opephora krumbeinii*) species (Figure 4). Species in Group 5 are present at all elevations with an increased occurrence between 160 to 215 SWLI and 240 to 260 SWLI.

Group 6: bimodal distribution with elevation and a maximum probability of occurrence of 0.23 at 156 SWLI (Figure 5). Species in Group 6 are composed of allocthonous marine species *Cocconeis scutellum* and *Planothidium delicatulum* (Figure 4). The probability of occurrence of species in Group 6 shows a high proportion (> 0.15) of occurrence below 170 SWLI.

Group 7: probabilities of occurrence show a negative relationship with elevation and a maximum probability of occurrence of 0.26 at 136 SWLI (Figure 5). Species in Group 7 are composed of marine species *Cocconeis scutellum var parvum*, *Opephora minuta*, and *Opephora pacifica* (Figure 4). The probability of occurrence of species in Group 7

is very low except for SWLI values less than 190 where probability of occurrence increases with decreasing elevation.

Group 8: positive linear with elevation and a maximum probability of occurrence of 0.25 at 267 SWLI (Figure 5). Species in Group 8 are a combination of freshwater (e.g., *Cosmioneis pusilla*) and allochthonous marine (e.g., *Paralia sulcata*) species (Figure 4). The probability of occurrence of species in Group 8 is very low at SWLI values less than 150 but steadily increases with elevation thereafter.

Group 9: multimodal distribution with elevation and a maximum probability of occurrence of 0.18 at 221 SWLI (Figure 5). Species in Group 9 are freshwater (e.g., *Denticula subtilis*, *Navicula cincta*, and *Pinnularia lagerstedtii*) with the exception of brackish species *Opephora guenter-grassi* (Figure 4). Species in Group 9 are present at all elevations with an increased occurrence between 210 and 236 SWLI.

Group 10: bimodal distribution with elevation and a maximum probability of occurrence of 0.04 at 241 SWLI (Figure 5). Species in Group 10 are a combination of freshwater (e.g., *Nitzschia terrestris*) and brackish (e.g., *Navicula sieminskiae*) species (Figure 4). The probability of occurrence of species is low in Group 10 and steadily increases (0 to 0.04) with elevation.

Group 11: positive linear relationship with elevation and a maximum probability of occurrence of 0.07 at 224 SWLI (Figure 5). The freshwater species *Lutica mutica* is the only species in Group 10 (Figure 4). The probability of occurrence of *Luticola mutica* is 0 at SWLI values less than 184 but shows an increase with elevation at SWLI values above 184.

Group 12: bimodal distribution with elevation and a maximum probability of occurrence of 0.18 at 136 SWLI (Figure 5). Species in Group 12 are a combination of marine (e.g., *Planothidium engelbrechtii*), brackish (e.g., *Nitzschia clausii*) and freshwater (e.g., *Luticola muticoides*) species (Figure 4). Species in Group 12 show an increasing probability of occurrence with decreasing elevation with the exception of a slight increase in probability of occurrence from 213 to 250 SWLI.

4.1.1 Validation of WA-PLS and BDTF

We chose Component 2 of the WA-PLS transfer function due to its low RMSEP (0.30) and high r^2 (0.86) values (Figure 6). The WA-PLS transfer function shows a strong relationship between observed (0.50 to 2.57 m MTL) and predicted elevations (0.54 to 2.43 m MTL; Figure 6a). The residuals display no obvious structure with the residuals ranging from -0.38 to 0.50 (mean: 0.01; Figure 6b). But the application of the MAT of the WAPLS transfer function to the fossil diatoms assemblages of Redtail show all samples have poor modern analogues (Figure 7).

The BDTF displays a good relationship between observed and predicted elevations (0.50 to 2.00 m MTL; Figure 8a). The residuals display no clear structure with the residuals ranging from -0.50 to 0.71 (mean: -0.03; Figure 8b). The grouping of species improves the MAT results; 21% of fossil samples have a good analogue (Figure 7). We note all but one of the good analogues were found in the upper 1.5 m of the sediment core, which spans the two uppermost mud-over-peat contacts at Redtail. Dominant species in the fossil samples with poor analogues not found in high abundance from our modern training set include marine (*Delphineis surirella*, *Fragilaria investiens*, and *Navicula microdigitoradiata*) and brackish (*Caloneis westii*) species.

The comparison of MAT between WA-PLS and BDTF show that grouping species led to a reduction of dissimilarity (Figure 9). For each sample, we plot the minimum distance coefficients of the individual versus grouped species. The average minimum distance coefficient of the individuals species is 2.20 (SD: 0.58) compared to the grouped species is 0.78 (SD: 0.23)

4.2 Stratigraphy of Redtail

The stratigraphy of our Redtail core consists of six transgressive sequences of mud or rooted mud that gradually grades into an organic-rich O or O/A horizon of a high marsh of spruce swamp soil that is abruptly overlain by mud or rooted mud. At the Redtail locality these abrupt mud-over-peat contacts occur at the tops of each of the six wetland soils described and named by Atwater and Hemphill-Haley (1997; Figure 10; Soils Y, U, S, N, L, and J). Atwater (1987) and Atwater and Hemphill-Haley (1997) used the pattern of thick, boldly developed and thin weakly developed O and O/A horizons of these soils in outcrops and cores to widely correlate the soils at tidal sites in the Willapa Bay region. At the Redtail locality, the O and O/A horizons are dark brown, organic-rich silt that we classified as peaty mud, muddy peat, or peat depending on the relative concentration of organics (Troels Smith 1955). All soils have a sharp (< 2 mm) upper contact and are directly overlain by a light gray to brown mud or rooted mud with the exception of the uppermost soil (Soil Y), which is sharply overlain by a silty sand bed that we interpret to be a tsunami sand. Because the abrupt contacts at the tops of the organic-rich soil horizons at Redtail record rapid RSL rises that we and previous researchers infer to have been caused by earthquake subsidence, we describe in detail the mud-over-peat contacts formed during coseismic subsidence:

4.2.1 *Mud-Peat Contact 1*

Contact 1 is our uppermost mud-over-peat contact found at 0.30 m depth (Figure 10). In the field, we correlated this contact with the mud-over peat upper contact of Soil Y described by Atwater and Hemphill-Haley (1997; Figure 2). Tree-ring dating of buried tree roots and radiocarbon dating of organic material in Soil Y from southern Washington correlates with the 1700 CE earthquake (e.g., Atwater and Yamaguchi, 1991; Atwater, 1992; Atwater and Hemphill-Haley, 1997)

Contact 1 is characterized by a 15-cm thick dark brown, silty peat (mean: 6.09 Φ) that is sharply (< 1 mm) overlain by a 1-cm interval of light gray silty sand (mean: 3.15 Φ), which transitions to a light gray to brown mud (mean: 5.52 Φ; Figure 10). LOI shows a notable amount of organic matter in the peat (28 to 37%) that decreases in the overlying mud (7 to 32%).

The diatoms display a sudden shift from freshwater (51 to 74% abundance) to marine (44 to 68% abundance) species from peat to mud across contact 1 (Figure 11). In the underlying peat, freshwater species such as *Cosmioneis pusilla*, *Luticola mutica*, and *Navicula cincta* dominate. In the silty sand unit directly above the peat, freshwater species remain dominant with no noticeable change in species abundance. However, the overlying mud shows a shift to marine diatom species such as *Delphineis surirella*, *Fragilaria investiens*, and *Navicula microdigitoradiata*.

Results of the WA-PLS transfer function show the pre-seismic paleoelevation of the buried peat ranged from 1.37 to 1.46 m above MTL (Figure 12). We select the uppermost centimeter of peat as our pre-seismic elevation (1.44 m above MTL). Directly overlying the peat is a silty sand unit that was deposited by a tsunami. For this

reason, we do not consider the reconstructed elevation at this sample to be a reliable post-seismic estimate (e.g., Nelson et al., 2008). We select the mud sample directly overlying the silty sand unit as our post-seismic elevation (1.09 m above MTL). From these two values we estimate a coseismic subsidence of 0.35 m (± 0.41 m). MAT results indicate that the fossil samples across Contact 1 have poor analogues.

Results of the BDTF show the pre-seismic paleoelevation of the buried peat ranged from 1.17 to 1.60 m above MTL (Figure 12). We follow the same guideline as the WA-PLS reconstruction to select our pre- (1.58 m above MTL) and post-seismic (1.12 m above MTL) elevations. From these two values we estimate a coseismic subsidence of 0.46 (± 0.33 m). MAT results indicate that the fossil samples have poor analogues in the mud overlying the peat (0 to 28 cm depth) but good analogues in the underlying peat as well as the silty sand unit directly overlying the peat (29 to 46 cm depth).

4.2.2 Mud-Peat Contact 2

Contact 2, at the top of Soil U, is located at 1.30 m depth in the core (Figure 10). Atwater and Hemphill-Haley (1997) were unable to find suitable material to radiocarbon date the burial of Soil U at Redtail. However, at their Oyster locality (located ~1 km downstream of the Niawiakum River; Figure 1), *Salicornia virginica* stems in Soil U (1260 ± 14 ^{14}C yr BP) and *Triglochin maritimum* rhizomes in the overlying mud (1302 ± 21 ^{14}C yr BP) narrowly constrain the timing of Soil U burial (Figure 10).

Contact 2 is characterized by a 10-cm thick dark brown to black, silty peat (mean: 5.53 Φ) that is sharply (< 2 mm undulating over 2 cm) overlain by a light gray and brown rooted mud (mean: 5.09 Φ) with mica (Figure 10). LOI shows a slight increase of organic matter in the peat (7 to 15%) compared to the overlying mud (3 to 6%).

The diatoms display a sudden shift from freshwater (66 to 79% abundance) to marine (39 to 66% abundance) species concurrent with the change in lithostratigraphy from peat to mud (Figure 11). In the underlying peat, freshwater species such as *Achnanthidium minutissima var affinis*, *Cosmioneis pusilla*, *Melosira varians*, *Navicula cincta*, and *Nitzschia frustulum* dominate. The overlying mud shows a shift to marine diatom species such as *Delphineis surirella*, *Fragilaria investiens*, *Planothidium engelbrechtii*, and *Tabularia fasciculata*.

Results of the WA-PLS transfer function show the pre-seismic paleoelevation of the buried peat ranged from 1.49 to 1.80 m above MTL (Figure 12). Due to the undulating nature of the contact between the peat and overlying mud causing the uppermost peat sample to contain a small portion of the overlying mud, we selected the next lowest sample in the peat as our pre-seismic elevation (1.80 m above MTL; Nelson et al., 1996a). We select the mud sample directly overlying the peat as our post-seismic elevation (1.47 m above MTL). From these two values we estimate a coseismic subsidence of 0.33 m (± 0.47 m). MAT results indicate that the fossil samples across Contact 2 have poor analogues.

Results of the BDTF show the pre-seismic paleoelevation of the buried peat ranged from 1.13 to 1.53 m above MTL (Figure 12). We follow the same guideline as the WA-PLS reconstruction to select our pre- (1.53 m above MTL) and post-seismic (1.02 m above MTL) elevations. From these two values we estimate a coseismic subsidence of 0.51 m (± 0.34 m). MAT results indicate good analogues for the fossil samples from the transgressive mud to peat sequence (130 to 139 cm and 141 to 142 cm depth) and overlying mud (126 to 129 cm depth).

4.2.3 Mud-Peat Contact 3

Contact 3, at the top of Soil S, is located at 2.22 to 2.25 m depth in the core (Figure 10). Roots or sticks found at the top of Soil S provide a maximum age range of 1720 to 1830 ± 40 to 70 ^{14}C yr BP for Soil S burial (Atwater and Hemphill-Haley (1997).

Contact 3 is characterized by a 3-cm thick, faint reddish brown, silty peat (mean: 6.28 Φ) that is sharply (< 2 mm) overlain by a light gray and brown mud (mean: 5.84 Φ; Figure 10). LOI shows a slight increase of organic matter in the peat (5 to 10%) compared to the overlying mud (minimum: 4 to 8%).

The diatoms display a shift from freshwater (67 to 78% abundance) to marine (41 to 69% abundance) species concurrent with the change in lithostratigraphy from peat to mud (Figure 11). In the underlying peat, freshwater species such as *Achnanthidium minutissima var affinis*, *Cosmioneis pusilla*, *Melosira varians*, *Navicula cincta*, and *Pinnularia lagerstedtii* dominate. The overlying mud shows a shift to marine diatom species such as *Delphineis surirella*, *Fragilaria investiens*, *Navicula microdigitoradiata*, and *Tabularia fasciculata*.

Results of the WA-PLS transfer function show the pre-seismic paleoelevation of the buried peat ranged from 1.36 to 1.67 m above MTL (Figure 12). We select the uppermost cm of peat as our pre-seismic elevation (1.36 m above MTL). We select the mud sample directly overlying the peat as our post-seismic elevation (1.40 m above MTL). From these two values we estimate a slight coseismic uplift of 0.04 m (± 0.43 m). MAT results indicate that the fossil samples across Contact 3 have poor analogues that exceed the 20th percentile threshold.

Results of the BDTF show the pre-seismic paleoelevation of the buried peat ranged from 1.10 to 1.55 m above MTL (Figure 12). We follow the same guideline as the WA-PLS reconstruction to select our pre- (1.55 m above MTL) and post-seismic (1.05 m above MTL) elevations. From these two values we estimate a coseismic subsidence of 0.50 m (± 0.35 m). MAT results indicate that the fossil samples across Contact 3 have poor analogues that exceed the 20th percentile threshold.

4.2.4 Mud-Peat Contact 4

Contact 4, at the top of Soil N, is located at 2.58 m depth in the core (Figure 10). Sticks and spruce cones found at the top of Soil N provide a maximum age range of 2258 to 2780 ± 23 to 100 ^{14}C yr BP for Soil N burial (Atwater and Hemphill-Haley (1997).

Contact 4 is characterized by a 14-cm thick dark brown to black, silty peat (mean: 7.00 Φ) that is sharply (< 1 mm) overlain by a light gray and brown mud (mean: 6.13 Φ; Figure 10). LOI shows a notable amount of organic matter in the peat (11 to 73%) compared to the overlying mud (4 to 5%).

The diatoms display a mixture of freshwater (33 to 52% abundance) to marine (45 to 47% abundance) species across the contact (Figure 11). In the underlying peat, freshwater species such as *Achnanthidium minutissima var affinis* and *Melosira varians* as well as marine species *Delphineis surirella* are found in high abundance in the peat. The overlying mud shows a high abundance of the marine species *Delphineis surirella* and *Navicula microdigitoradiata* as well as the brackish species *Gyrosigma eximium*.

Results of the WA-PLS transfer function show the pre-seismic paleoelevation of the buried peat ranged from 1.45 to 2.23 m above MTL (Figure 12). We select the

uppermost cm of peat as our pre-seismic elevation (1.45 m above MTL). We select the mud sample directly overlying the peat as our post-seismic elevation (1.39 m above MTL). From these two values we estimate a coseismic subsidence of 0.06 m (± 0.45 m). MAT results indicate that the fossil samples across Contact 4 have poor analogues that exceed the 20th percentile threshold.

Results of the BDTF show the pre-seismic paleoelevation of the buried peat ranged from 1.36 to 1.45 m above MTL (Figure 12). We follow the same guideline as the WA-PLS reconstruction to select our pre- (1.45 m above MTL) and post-seismic (1.06 m above MTL) elevations. From these two values we estimate a coseismic subsidence of 0.39 m (± 0.35 m). MAT results indicate that the fossil samples across Contact 4 have poor analogues that exceed the 20th percentile threshold.

4.2.5 Mud-Peat Contact 5

Contact 5 is located at 3.06 m depth in the core (Figure 10). Roots and peat found at the top of Soil L provide a maximum age range of 2790 to 3190 ± 30 to 120 ^{14}C yr BP for Soil L burial (Atwater and Hemphill-Haley (1997).

Contact 5 is characterized by a 2-cm thick dark brown, silty peat (mean: 6.65 Φ) that is sharply (< 2 mm) overlain by a light gray and brown mud (mean: 6.34 Φ; Figure 10). LOI shows a similar concentration of organic matter in the peat (6%) and the overlying mud (minimum: 4 to 5%).

The diatoms display a shift from freshwater (72 to 73% abundance) to marine (38 to 58% abundance) species concurrent with the change in lithostratigraphy from peat to mud (Figure 11). In the underlying peat, freshwater species such as *Achnanthidium*

minutissima var affinis, *Cosmioneis pusilla*, *Luticola mutica*, *Navicula cincta* and *Pinnularia lagerstedtii* dominate. The overlying mud shows a high abundance of the marine species *Delphineis surirella* and *Nitzschia compressa var compressa* as well as the brackish species *Caloneis westii*.

Results of the WA-PLS transfer function show the pre-seismic paleoelevation of the buried peat ranged from 1.68 to 1.81 m above MTL (Figure 12). We select the uppermost cm of peat as our pre-seismic elevation (1.68 m above MTL). We select the mud sample directly overlying the peat as our post-seismic elevation (1.57 m above MTL). From these two values we estimate a coseismic subsidence of 0.11 m (± 0.52 m). MAT results indicate that the fossil samples across Contact 5 have poor analogues that exceed the 20th percentile threshold.

Results of the BDTF show the pre-seismic paleoelevation of the buried peat ranged from 1.50 to 1.55 m above MTL (Figure 12). We follow the same guideline as the WA-PLS reconstruction to select our pre- (1.50 m above MTL) and post-seismic (1.13 m above MTL) elevations. From these two values we estimate a coseismic subsidence of 0.37 m (± 0.37 m). MAT results indicate that the fossil samples across Contact 5 have poor analogues that exceed the 20th percentile threshold.

4.2.6 Mud-Peat Contact 6

Contact 6 is located at 3.62 m depth in the core (Figure 10). Twigs, spruce cones, and sticks found at the top of Soil J provide a maximum age range of 3063 to 3730 ± 17 to 210 ^{14}C yr BP for Soil J burial (Atwater and Hemphill-Haley (1997).

Contact 6 is characterized by a 16-cm dark brown to black, silty peat (mean: 6.69 Φ) that is sharply (< 1 mm) overlain by a light gray and brown rooted mud (mean: 5.56 Φ; Figure 10). LOI shows a notable amount of organic matter in the peat (7 to 60%) compared to the overlying mud (6 to 7%).

The diatoms display a mixture of freshwater to marine species across the contact with marine diatoms becoming gradually dominant (17 to 67% abundance) moving upward in the peat and remaining dominant (52 to 67% abundance) in the overlying mud (Figure 11). In the underlying peat, freshwater species such as *Cosimioneis pusilla* and *Luticola mutica* as well as marine species *Delphineis surirella*, *Fragilaria investiens,* and *Tabularia fasciculata* are found in high abundance in the peat. The overlying mud shows a high abundance of the marine species *Delphineis surirella* and *Fragilaria investiens*.

Results of the WA-PLS transfer function show the pre-seismic paleoelevation of the buried peat ranged from 1.28 to 1.92 m above MTL (Figure 12). We select the uppermost cm of peat as our pre-seismic elevation (1.28 m above MTL). We select the mud sample directly overlying the peat as our post-seismic elevation (1.33 m above MTL). From these two values we estimate a slight coseismic uplift of 0.05 m (± 0.43 m). MAT results indicate that the fossil samples across Contact 6 have poor analogues that exceed the 20th percentile threshold.

Results of the BDTF show the pre-seismic paleoelevation of the buried peat ranged from 1.39 to 1.60 m above MTL (Figure 12). We follow the same guideline as the WA-PLS reconstruction to select our pre- (1.46 m above MTL) and post-seismic (1.08 m above MTL) elevation. From these two values we estimate a coseismic subsidence of

0.38 m (± 0.34 m). MAT results indicate that the fossil samples across Contact 6 have poor analogues with the exception of one sample in the peat (364 to 365 cm depth) that shows a good analogue.

5. Discussion

5.1 Diatom transfer functions in Cascadia

The accurate assessment of Cascadia's regional earthquake hazards requires well-constrained, realistic geophysical models of upper-plate deformation during great megathrust earthquakes (Wang and Tréhu, 2016; Gomberg and Ludwig, 2017; Ludwig et al., 2018). Estimates of coastal land-level change derived from microfossil-based transfer functions within stratigraphic records are the most precise means to reconstruct deformation during past megathrust earthquakes in Cascadia (Wang et al., 2013).

Diatom-based transfer functions have been applied to reconstruct land-level change from megathrust earthquakes in Alaska (e.g., Zong et al., 2003; Shennan and Hamilton, 2006; Barlow et al., 2012), Chile (Hocking et al., 2017), and Japan (Sawai et al., 2004a, b). In Cascadia, Nelson et al. (2008) showed that a limited modern training set with a lack of good analogues resulted in unreliable estimates of subsidence from the WA-PLS transfer function for a sequence at Alsea Bay, OR. Our results from the WA-PLS transfer function reinforce the limitations of an established diatom transfer function approach in Cascadia. While the WA-PLS transfer function displayed a strong relationship between observed and predicted elevations (Figures 6 and 8), all reconstructions had poor modern analogues (Figure 7). Indeed, high dissimilarity between fossil samples and training sets from local sites was also found in south central

Chile was found by Garrett et al. (2013) who showed that despite a modern training set with a high number of samples (n=96), the limited range of modern environments sampled resulted in poor analogues. Site-specific variability in diatom assemblage distribution often results in local training sets that fail to capture a broad enough range of environments to provide a good analogue for fossil reconstructions (e.g., Weilhoefer and Pan, 2006; Nelson et al., 2008; Sawai et al., 2016). RSL reconstruction studies in the North Atlantic (e.g., Woodroffe and Long, 2010; Barlow et al., 2013), Chile (Hocking et al., 2017), and Alaska (e.g., Watcham et al., 2013) compared local and regional training sets to show that diatom transfer functions using a regional training set resulted in many more modern analogues.

In Cascadia, our novel approach of grouping species based on their similarities with respect to abundance and their distribution along the elevational gradient provides a solution by diminishing the influence of site-specific assemblages and improving the issue of no modern analogues. A comparison of the MAT analysis of individual versus grouped species showed an increase in the number of good analogues from 0% to 21% (Figure 9). The grouping of diatoms has been applied in bioassessment studies of pollution to more readily identify ecological patterns obscured at species level (e.g., Fore and Grafe, 2002). For example, a study by Passy (2007) developed a method of grouping diatoms to show more distinct distributions along nutrient and disturbance gradients. Although Hamilton and Shennan (2005a) did not group diatom species to reconstruct land-level change from megathrust earthquakes in Alaska, they developed multiple transfer functions by limiting the modern training set to narrow elevation ranges based on lithostratigraphic context (e.g., peat forming elevations) and selecting

the appropriate transfer function to apply to the fossil sample, which resulted in 74% of fossil samples having a good modern analogue.

The improvement of modern analogues varied among substrate and mud-over-peat contacts. All but one of our good analogue samples were found in the upper 1.50 m of the core across Contacts 1 and 2 (Figure 7). Dominant fossil diatoms (maximum abundance of > 5% in a single sample) in the good analogue samples were predominantly freshwater (e.g., *Achnanthidium minutissimum var affinis*, *Cosmioneis pusilla*, *Luticola mutica*, *Melosira varians*, and *Pinnularia lagerstedtii*) and marine (e.g., *Planothidium engelbrechtii*) species (Figure 9). The freshwater species are found in the modern training set at similar elevations that span the low and high marsh environments (Chapter 2). Additionally, we note the tsunami sand deposited over Contact 1 also displayed a good analogue (Figure 7). Fossil diatoms from tsunami beds are likely to have good analogues because tsunamis entrain and deposit local sediments (e.g., Pilarczyk et al., 2014; Dura et al., 2016), but they are unreliable post-seismic estimates due to the allochthonous (not *in situ*) nature of the sediments (e.g., Nelson et al., 2008). The fossil samples in the upper 1.50 m of the core with poor analogues are found within the tidal mud (Figure 7). Dominant fossil diatoms these poor analogue samples are marine (*Berkeleya scopolorum* and *Gyrosigma acuminatum*), brackish (*Caloneis westii*), and freshwater (*Nitzschia capitellata*) species (Figure 9). These species were not found in high abundance in the modern training set (Chapter 2).

Fossil samples below 1.50 m depth in the core had poor analogues with the exception of one sample (364 to 365 cm depth) in Soil J (Figure 7). Abundant (maximum abundance of > 2%) fossil species in this sample are a combination of marine (e.g., *Delphineis surirella*), brackish (e.g., *Navicula perminuta*), and freshwater (e.g.,

Luticola mutica) species. Dominant species in Soils S, N, L, and J are freshwater species (e.g., *Cosmioneis pusilla, Luticola mutica,* and *Navicula cincta*) found in the modern training set at low and high marsh environments and marine species (e.g., *Melosria nummuloides, Opephora guenter-grassi, and Paralia sulcata*) found across the intertidal (Chapter 2). Fossil samples with the greatest dissimilarity value was found in the mud/rooted mud units rather than the wetland soils (Figure 9). Dominant fossil diatoms in the mud/rooted mud are marine (e.g., *Berkeleya scopolorum, Mastogloia smithii*, and *Nitzschia granulata*) and brackish (e.g., *Caloneis westii*, *Gyrosigma eximium*, and *Scolioneis tumida*) species (Figure 9). These species were not found in high abundance in the modern training set (Chapter 2) but have been observed in the low marsh and tidal flat environments of Willapa Bay (Hemphill-Haley, 1995a). The lack of good analogues below 1.50 m depth suggests that the modern intertidal environment from which the training set was collected does not capture the range of paleoenvironmental conditions that existed in Willapa Bay from ~1400 to 3500 yrs ago.

Modern diatom distribution studies of intertidal environments at the Niawiakum River by Hemphill-Haley (1995b) and Sawai et al. (2016) could be combined with our data to produce a much larger regional training set that may increase the number of good modern analogues in fossil assemblages in Cascadia. For example, we observe highly abundant species (e.g., *Dephineis surirella* and *Caloneis westii*) below 1.50 m depth in our core that is also found in high abundance in the modern dataset of Hemphill-Haley (1995a) but is not abundant in our modern training set. However, we identified differences in species distributions across the tidal frame that we primarily attribute to variances in taxonomy (Chapter 2). Harmonizing taxonomy is difficult to accomplish due to the high diversity of diatom species that result in analyst bias influencing diatom

identification (Lee et al., 2019). For this reason, expanding our analysis with other training sets may be difficult. Furthermore, the difference of several decades between the sampling of our modern training set compared to the modern training set of Hemphill-Haley (1995b) would make it difficult to account for environmental changes in Willapa Bay. For example, Willapa Bay has undergone rapid changes in flora and fauna in the last 40 years with the introduction of invasive species such as eastern cordgrass (*Spartina alterniflora*) that has reduced the surface area, and thus productivity, of mudflats (e.g., Sayce, 1988; Atwater and Hemphill-Haley, 1997; Emmett et al., 2000). This change is vascular plant communities is likely also reflected by changes in diatom floras.

The BDTF provides two further advantages compared to the WA-PLS transfer function: (1) inclusion of flexible (non-unimodal) species response curves; and (2) integration of prior information (in our case, assumptions about elevation based on lithostratigraphy) from proxies (Cahill et al., 2016). Firstly, although the assumption that diatoms exhibit a unimodal relationship with elevation is ecologically plausible (e.g., Hemphill-Haley, 1995a; Zong and Horton, 1999; Juggins and Birks, 2012), our findings show that this assumption does not hold for our modern diatom distributions (Figure 7). Unlike the WA-PLS, which forces species into a unimodal distribution, the BDTF is able to model the observed distributions of the modern training set (Cahill et al., 2016). Many of the group response curves show broad unimodal, bimodal or multimodal distributions of occurrence with respect to elevation (Figure 5). Other group response curves display a high probability of occurrence within a narrow range of low (Group 7) and high (Groups 8 and 11) elevations (Figure 5).

Secondly, we show that the addition of prior information to the reconstruction resulted exclusively in subsidence estimates for all six mud-over-peat contacts (Figure 12). The BDTF produces subsidence estimates that range from 0.37 to 0.51 m. In contrast, the WA-PLS transfer function reconstructs land-level change that ranges from subsidence (0.06 to 0.35 m) to uplift (0.04 to 0.05 m). Without the ability to incorporate priors, Garrett et al. (2013) showed that land-level change reconstructions using the WA-PLS diatom transfer function resulted in estimates that did not distinguish between uplift or subsidence during the 1960 and 2010 Chilean great earthquakes despite observations of uplift (0.3 to 1.3 m) in 1960 and in 2010 (0.5 to 2 m) for south-central Chile (e.g., Plafker and Savage, 1970 Farías et al., 2010: Melnick et al., 2012).

The results of the BDTF reconstruction are more consistent with stratigraphic evidence for subsidence. The six soil horizons are sharply overlain by mud or rooted mud that is indicative of a drop in land level from the a high marsh/spruce swamp to a tidal flat/low marsh. Hemphill-Haley (1995a, b) and Atwater and Hemphill-Haley (1997) estimate this change in environment is equivalent to subsidence of at least 1 m at the Niawiakum River based on the observed elevation range of the tidal flat, low marsh, high marsh, and forested swamp environments. Atwater and Yamaguchi (1991) produced similar subsidence estimates (0.5 to 2 m) by comparing the stratigraphic position of growth position fossil plants to their modern elevation throughout Willapa Bay. Horton et al. (2018) analyzed >780 Holocene reconstructions of tidal marsh evolution in Great Britain. The authors showed that transgressive contacts (peat overlain by mud) exclusively form when RSL is rising.

Our results show that the incorporation of prior information to the BDTF reconstruction resulted in reduced uncertainty. The mean uncertainty for the WA-PLS transfer

function is 0.34 whereas for the BDTF it is 0.16. With the addition of our lithologic prior, the BDTF was able to model the increased probability of paleoelevation within a formally defined range that resulted in more realistic reconstruction estimates. A similar result was shown by Cahill et al., (2016) who used a foraminifera-based Bayesian transfer function to model sea-level rise in New Jersey with the use of prior information ($\delta_{13}C$) resulting in a reduced uncertainty of ~28%.

However, without an instrumentally observed megathrust earthquake along the CSZ, we are unable to conclusively assess the accuracy of the BDTF in reconstructing subsidence. Engelhart et al. (2013) simulated coseismic subsidence in South Slough, OR by transplanting marsh at a lower elevation and showed that foraminifera-based transfer functions were able to reconstruct subsidence. We suggest conducting a similar control study using the BDTF to test the reconstruction against a known "subsidence" event.

5.2. Comparison of subsidence estimates

The results of our BDTF estimated coseismic subsidence of Contacts 1-6 at Redtail ranged from 0.37 to 0.51 m (± 0.33 to 0.37 m; Figure 12). MAT analysis showed that fossil samples across Contact 1 and 2 had good analogues, which suggests that the estimated subsidence of Soil Y (0.46 m ± 0.33 m) and Soil U (0.51 m ± 0.34 m) may be reliable estimates of subsidence at Redtail (Figure 7). In contrast, fossil samples from Soil S, N, L, and J and the overlying mud/rooted mud resulted in a poor analogue match, which suggests that the estimated subsidence may be unreliable (Horton and Edwards, 2006; Barlow et al., 2013; Watcham et al., 2013). For this reason, we will limit our comparison of subsidence estimates to Contacts 1 and 2.

The mud-over-peat contact (Contact 1) at the top of Soil Y has a coseismic subsidence of 0.46 m ± 0.33 m, which is smaller than other microfossil estimates of 1700 CE subsidence at Willapa Bay (e.g., Atwater and Hemphill-Haley, 1997; Sabean, 2004; Wang et al., 2013). Wang et al. (2013) reassessed the subsidence value of Sabean's (2004) using a foraminiferal-based WA-PLS transfer function to produce a subsidence estimate of 0.58 ± 0.28 m at the nearby Oyster locality (Figure 1). More recently, Kemp et al. (2018) also reanalyzed Sabean (2004) using a foraminifera-based Bayesian transfer function to produce a subsidence estimate of 1.25 m ± 0.85. Atwater and Hemphill-Haley (1997) used an observed shift of diatom assemblages from high marsh or upland to low marsh or tidal flat environments to infer subsidence of at least 1 m at Redtail but with no error assessment. Wang et al. (2013) also reinterpreted this data to suggest subsidence of 0.7 to 1.1 m is a more reasonable estimate of subsidence at the Redtail locality.

The mud-over-peat contact (Contact 2) at the top of Soil U has a coseismic subsidence of 0.51 m ± 0.34 m that is similar to our subsidence estimate of the 1700 CE earthquake. Like Contact 1, Atwater and Hemphill-Haley (1997) infer a subsidence estimate of at least 1 m at Redtail with no formal error assessment. Sabean (2004) produced an estimate of 0.86 ± 1.03 m of subsidence at the Oyster locality (error assessed using a 95% confidence interval bootstrap method). Based on radiocarbon ages by Atwater and Hemphill-Haley at the Oyster locality, we correlate the burial of Soil U with transfer function estimates of subsidence by Milker et al. (2016) at Talbot Creek, OR (0.63 to 0.65 m ± 0.22 m). Leonard et al. (2010) averaged subsidence estimates of earthquakes preceding 1700 CE to model rupture area and displacement along the CSZ and found

that coseismic displacement remained similar between earthquakes, which is consistent with our findings that subsidence was similar for Contacts 1 and 2.

Variations in our subsidence estimates compared to foraminifera-based transfer function estimates at Willapa Bay may be due to differences in the response time of the two microorganisms. A sudden tidal-flooding experiment in Bandon, OR found that diatoms responded within two weeks of flooding compared to the 11 to 25 months required before foraminifera assemblages showed notable and lasting change, suggesting that diatom-based transfer functions are more likely to accurately record immediate coseismic land-level change (Horton et al., 2017). The delay in foraminifera recolonization may result in larger subsidence estimates compared to diatoms because the foraminifera may reflect both coseismic and postseismic deformation (Horton et al., 2017). Geodetic observations of coseismic and postseismic slip of megathrust earthquakes have found that the afterslip can release a moment of ~10 to 30% of the mainshock over the course of weeks to a year (e.g., Heki et al., 1997; Chleih et al., 2007; Ozawa et al., 2011).

Our results show that while the BDTF produced reasonable subsidence estimates of Contact 1 and 2, fossil samples from Contacts 4-6 resulted in a poor analogue match. A solution to the no modern analogue problem would be to collect more samples that cover environments not currently represented in our training set. This solution is supported by a comparison of local versus regional diatom training sets by Watcham et al. (2013) who found that a larger training set from a sub-regional or regional scale resulted in an increase of good analogues that produced more reliable estimates of subsidence during the AD 1964 earthquake in Alaska. Future work will focus on identifying sites with a high abundance of fossil species that are not represented in our

modern training set (e.g., *Caloneis westii*, *Delphineis surirella*, *Fragilaria investiens*, and *Navicula microdigitoradiata*). An increase in tidal flat or sub-tidal samples would also help the BDTF differentiate between these two environments and may increase subsidence estimates.

Conclusions

We assessed the limitations of developing and applying a diatom-based transfer function in Cascadia where no modern analogues have resulted in unreliable estimates of coseismic subsidence. Using a modern training set of 67 samples collected from three tidal marshes in Willapa Bay, we develop and apply two transfer functions to a sediment core from the Redtail locality: (1) weighted-averaging partial least squares (WA-PLS) transfer function and (2) a new, Bayesian diatom transfer function (BDTF). We summarize the results as follows:

1. The WA-PLS transfer function resulted in reconstructions of land-level change that ranged from subsidence (0.06 to 0.35 m) to uplift (0.04 to 0.05 m) with large uncertainties (± 0.41 to 0.52 m). MAT results of the individual species using the WA-PLS transfer function showed that all fossil samples had poor modern analogues.
2. To address the no modern analogue problem in our training set, we grouped species based on similarities in abundance and distribution across elevation, resulting in the creation of 12 groups. While many of the group response curves showed broad, unimodal and bimodal distributions of occurrence across elevation, response curves of Group 7, 8, and 11 displayed a high probability of occurrence within a narrow range of SWLI values, suggesting that the BDTF is

more suitable for reconstructing coseismic subsidence because it is able to more accurately model response curves at higher and lower elevations.

3. The BDTF produced subsidence estimates that ranged from 0.37 to 0.51 m (± 0.33 to 0.37 m). MAT results of the grouped species showed improvement with 21% of fossil samples showing good analogues. We note all but one of the good analogues were found in the upper 1.5 m of the sediment core, which spans the two uppermost mud-over-peat contacts at Redtail. These results show that modern training set does not fully capture the range of paleoenvironmental conditions that existed in Willapa Bay from ~1400 to 3500 yrs.

MAT results show Contact 1 and 2 have good modern analogues, which suggests the BDTF estimates may be reliable estimates of subsidence from the 1700 CE earthquake (Contact 1; 0.46 m ± 0.33 m) and Contact 2 (0.51 m ± 0.34 m). If these estimates are reliable, they match with modeled observations that southern Washington was an area of low slip during the 1700 CE earthquake. Future work will include the collection of modern samples that will reduce the no analogue issue and the application of the BDTF to a simulated marsh subsidence experiment to assess the accuracy of the BDTF in reconstructing land-level change.

References

Adams, J. (1990). Paleoseismicity of the Cascadia subduction zone: Evidence from turbidites off the Oregon-Washington margin. *Tectonics, 9*(4), 569-583.

Admiraal, W. (1984). The ecology of estuarine sediment-inhabiting diatoms. *Progress in phycological research, 3*, 269-322.

Atwater, B. F. (1987). Evidence for great Holocene earthquakes along the outer coast of Washington State. *Science, 236*(4804), 942-944.

Atwater, B. F. (1992). Geologic evidence for earthquakes during the past 2000 years along the Copalis River, southern coastal Washington. *Journal of Geophysical Research: Solid Earth, 97*(B2), 1901-1919.

Atwater, B. F., & Hemphill-Haley, E. (1997). *Recurrence intervals for great earthquakes of the past 3,500 years at northeastern Willapa Bay, Washington* (2330-7102).

Atwater, B.F., & Yamaguchi, D.K. (1991). Sudden, probably coseismic submergence of Holocene trees and grass in coastal Washington State. *Geology*, 9, 706-709.

Atwater, B. F., Tuttle, M. P., Schweig, E. S., Rubin, C. M., Yamaguchi, D. K., & Hemphill-Haley, E. (2003). Earthquake recurrence inferred from paleoseismology. *Developments in Quaternary Sciences, 1*, 331-350.

Barlow, N. L., Shennan, I., Long, A. J., Gehrels, W. R., Saher, M. H., Woodroffe, S. A., & Hillier, C. (2013). Salt marshes as late Holocene tide gauges. *Global and Planetary Change, 106*, 90-110.

Birks, H. (1995). Quantitative palaeoenvironmental reconstructions. *Statistical modelling of Quaternary science data. Technical Guide, 5*, 161-254.

Bourgeois, J. (2006). Earthquakes: A movement in four parts? *Nature, 440*(7083), 430.

Butzin, M., Köhler, P., & Lohmann, G. (2017). Marine radiocarbon reservoir age simulations for the past 50,000 years. *Geophysical Research Letters, 44*(16), 8473-8480.

Cahill, N., Kemp, A. C., Horton, B. P., & Parnell, A. C. (2016). A Bayesian hierarchical model for reconstructing relative sea level: from raw data to rates of change. *Climate of the Past, 12*(2), 525-542.

Campeau, S., Hequette, A., & Pienitz, R. (1995). *The distribution of modern diatom assemblages in coastal sedimentary environments of the Canadian Beufort sea: an accurate tool for monitoring coastal changes*. Paper presented at the Proceedings of the 1995 Canadian coastal conference.

Chlieh, M., Avoua, J.P., Hjorleifsdottir, V., Song, T.A., Ji, C., Sieh, K., Sladen, A., Hebert, H., Prawirodirdjo, L., Bock, Y., & Galetzka, J. (2007). Coseismic slip and afterslip of the great M_w 9.15 Sumatra-Andaman earthquake of 2004. *Bull. Seismol. Soc. Am.,* 97, S152-S173.

Clague, J. J. (1997). Evidence for large earthquakes at the Cascadia subduction zone. *Reviews of Geophysics, 35*(4), 439-460.

Cooke, S.S., 1997. *A Field Guide to the Common Wetland Plants of Western Washington & Northwestern Oregon*. Seattle Audubon Society.

Darienzo, M. E., Peterson, C. D., & Clough, C. (1994). Stratigraphic evidence for great subduction-zone earthquakes at four estuaries in northern Oregon, USA. *Journal of Coastal Research*, 850-876.

DeMets, C., Gordon, R. G., & Argus, D. F. (2010). Geologically current plate motions. *Geophysical Journal International, 181*(1), 1-80.

Dixit, S. S., Smol, J. P., Charles, D. F., Hughes, R. M., Paulsen, S. G., & Collins, G. B. (1999). Assessing water quality changes in the lakes of the northeastern United States using sediment diatoms. *Canadian Journal of Fisheries and Aquatic Sciences, 56*(1), 131-152.

Donato, S., Reinhardt, E., Boyce, J., Pilarczyk, J., & Jupp, B. (2009). Particle-size distribution of inferred tsunami deposits in Sur Lagoon, Sultanate of Oman. *Marine Geology, 257*(1-4), 54-64.

Dura, T., Hemphill-Haley, E., Sawai, Y., & Horton, B. P. (2016). The application of diatoms to reconstruct the history of subduction zone earthquakes and tsunamis. *Earth-Science Reviews, 152*, 181-197.

Edwards, R., & Horton, B. (2000). Reconstructing relative sea-level change using UK salt-marsh foraminifera. *Marine Geology, 169*(1-2), 41-56.

Engelhart, S.E., Horton, B.P., Nelson, A.R., Hawkes, A.D., Witter, R.C., Wang, K., Wang, P.-L. & Vane, C.H. (2013). Testing the use of microfossils to reconstruct great earthquakes at Cascadia, *Geology*, 41(10), 1067-1070.

Engelhart, S. E., Vacchi, M., Horton, B. P., Nelson, A. R., & Kopp, R. E. (2015). A sea-level database for the Pacific coast of central North America. *Quaternary Science Reviews, 113*, 78-92.

Farías, M., Vargas G., Tassara, A., Carretier, S., Baize, S., Melnick, D., & Bataille, K. (2010). Land-level changes produced by the Mw 8.8 2010 Chilean earthquake. *Science* 329(5994), 916.

Flück, P., Hyndman, R., & Wang, K. (1997). Three-dimensional dislocation model for great earthquakes of the Cascadia subduction zone. *Journal of Geophysical Research: Solid Earth, 102*(B9), 20539-20550.

Fore, L. S., and Grafe, C., 2002, Using diatoms to assess the biological condition of large rivers in Idaho (USA): *Freshwater Biology*, v. 47, no. 10, p. 2015-2037.

Gasse, F., Juggins, S., Kehlifa L.B. (1995). Diatom-based transfer functions for inferring hydrochemical characteristics of African lakes. *Palaeogeography, Palaeoclimatology, Palaeoecology*, 117, 31-54.

Garrett, E., Shennan, I., Watcham, E., & Woodroffe, S. (2013). Reconstructing paleoseismic deformation, 1: modern analogues from the 1960 and 2010 Chilean great earthquakes. *Quaternary Science Reviews, 75*, 11-21.

Goldfinger, C., Nelson, C. H., Morey, A. E., Johnson, J. E., Patton, J. R., Karabanov, E. B., . . . Dunhill, G. (2012). *Turbidite event history--Methods and implications for Holocene paleoseismicity of the Cascadia subduction zone* (2330-7102).

Gomberg, J.S., & Ludwig, K.A. (2017). Reducing risk where tectonic plates collide: *U.S. Geological Survey Fact Sheet* 3024, 4 p.

Guilbault, J.-P., Clague, J. J., & Lapointe, M. (1995). Amount of subsidence during a late Holocene earthquake—Evidence from fossil tidal marsh foraminifera at Vancouver Island, west coast of Canada. *Palaeogeography, Palaeoclimatology, Palaeoecology, 118*(1-2), 49-71.

Guilbault, J.-P., Clague, J. J., & Lapointe, M. (1996). Foraminiferal evidence for the amount of coseismic subsidence during a late Holocene earthquake on Vancouver Island, west coast of Canada. *Quaternary Science Reviews, 15*(8-9), 913-937.

Hamilton, S., & Shennan, I. (2005). Late Holocene great earthquakes and relative sea-level change at Kenai, southern Alaska. *Journal of Quaternary Science: Published for the Quaternary Research Association, 20*(2), 95-111.

Hamilton, S., & Shennan, I. (2005). Late Holocene relative sea-level changes and the earthquake deformation cycle around upper Cook Inlet, Alaska. *Quaternary Science Reviews, 24*(12-13), 1479-1498.

Hawkes, A. D., Horton, B., Nelson, A., & Hill, D. (2010). The application of intertidal foraminifera to reconstruct coastal subsidence during the giant Cascadia earthquake of AD 1700 in Oregon, USA. *Quaternary International, 221*(1-2), 116-140.

Hawkes, A. D., Horton, B., Nelson, A., Vane, C., & Sawai, Y. (2011). Coastal subsidence in Oregon, USA, during the giant Cascadia earthquake of AD 1700. *Quaternary Science Reviews, 30*(3-4), 364-376.

Heki, K., Miyazaki, S, & Tsuji, H. (1997). Silent fault slip following an interpolate thrust earthquake at the Japan Trench. *Nature* 386, 595-597.

Hemphill-Haley, E. (1995b). Intertidal diatoms from Willapa Bay, Washington: application to studies of small-scale sea-level changes.

Hemphill-Haley, E. (1995a). Diatom evidence for earthquake-induced subsidence and tsunami 300 yr ago in southern coastal Washington. *Geological Society of America Bulletin, 107*(3), 367-378.

Hemphill-Haley, E. (1996). Diatoms as an aid in identifying late-Holocene tsunami deposits. *The Holocene, 6*(4), 439-448.

Hocking, E. P., Garrett, E., & Cisternas, M. (2017). Modern diatom assemblages from Chilean tidal marshes and their application for quantifying deformation during past great earthquakes. *Journal of Quaternary Science, 32*(3), 396-415.

Horton, B. (1999). The distribution of contemporary intertidal foraminifera at Cowpen Marsh, Tees Estuary, UK: implications for studies of Holocene sea-level changes. *Palaeogeography, Palaeoclimatology, Palaeoecology, 149*(1-4), 127-149.

Horton, B., Edwards, R., & Lloyd, J. (1999). A foraminiferal-based transfer function: implications for sea-level studies. *The Journal of Foraminiferal Research, 29*(2), 117-129.

Horton, B. P., Corbett, R., Culver, S. J., Edwards, R. J., & Hillier, C. (2006). Modern saltmarsh diatom distributions of the Outer Banks, North Carolina, and the development of a transfer function for high resolution reconstructions of sea level. *Estuarine, Coastal and Shelf Science, 69*(3-4), 381-394.

Horton, B. P., & Edwards, R. J. (2006). Quantifying Holocene sea level change using intertidal foraminifera: lessons from the British Isles. *Departmental Papers (EES)*, 50.

Horton, B.P., Milker, Y., Dura, T., Wang, K., Bridgeland, W.T., Brophy, L., Ewald, M., Khan, N.S., Engelhart, S.E., Nelson, A.R., & Witter, R.C. (2017). Microfossil measures of rapid sea-level rise: Timing of response of two microfossil groups to a sudden tidal-flooding experiment in Cascadia. *Geology*, 45, 535-538.

Horton, B.P., Shennan, I., Bradley, S.L., Cahill, N., Kirwan, M., Kopp, R.E., & Shaw, T.A. (2018). Predicting marsh vulnerability to sea-level rise using Holocene relative sea-level data: *Nature Communications*, 9, 2687.

Hyndman, R. D. (2013). Downdip landward limit of Cascadia great earthquake rupture. *Journal of Geophysical Research: Solid Earth, 118*(10), 5530-5549.

Hyndman, R. D., & Wang, K. (1993). Thermal constraints on the zone of major thrust earthquake failure: The Cascadia subduction zone. *Journal of Geophysical Research: Solid Earth, 98*(B2), 2039-2060.

Jackson, S. T., & Williams, J. W. (2004). Modern analogs in Quaternary paleoecology: here today, gone yesterday, gone tomorrow? *Annual Review of Earth and Planetary Sciences, 32*.

Jennings, A. E., & Nelson, A. R. (1992). Foraminiferal assemblage zones in Oregon tidal marshes; relation to marsh floral zones and sea level. *The Journal of Foraminiferal Research, 22*(1), 13-29.

Juggins, S. (2011). C2 Version 1.7.7. Retrieved from https://www.staff.ncl.ac.uk/stephen.juggins/software/C2Home.htm

Juggins, S., & Birks, H. J. B. (2012). Quantitative environmental reconstructions from biological data. In *Tracking environmental change using lake sediments* (pp. 431-494): Springer.

Kelsey, H. M., Engelhart, S. E., Pilarczyk, J. E., Horton, B. P., Rubin, C. M., Daryono, M. R., . . . Cahill, N. (2015). Accommodation space, relative sea level, and the archiving of paleo-earthquakes along subduction zones. *Geology, 43*(8), 675-678.

Kelsey, H. M., Witter, R. C., & Hemphill-Haley, E. (1998). Response of a small Oregon estuary to coseismic subsidence and postseismic uplift in the past 300 years. *Geology, 26*(3), 231-234.

Kelsey, H. M., Witter, R. C., & Hemphill-Haley, E. (2002). Plate-boundary earthquakes and tsunamis of the past 5500 yr, Sixes River estuary, southern Oregon. *GSA Bulletin, 114*(3), 298-314.

Kemp, A.C, Nelson, A. R., & Horton, B. (2013). Radiocarbon dating of plant macrofossils from tidal-marsh sediment. In *Treatise on geomorphology* (pp. 370-388): Elsevier Inc.

Kemp, A. C., Cahill, N., Engelhart, S. E., Hawkes, A. D., & Wang, K. (2018). Revising estimates of spatially variable subsidence during the AD 1700 Cascadia earthquake using a Bayesian foraminiferal transfer function. *Bulletin of the Seismological Society of America, 108*(2), 654-673.

Kemp, A. C., Horton, B. P., Corbett, D. R., Culver, S. J., Edwards, R. J., & van de Plassche, O. (2009). The relative utility of foraminifera and diatoms for reconstructing late Holocene sea-level change in North Carolina, USA. *Quaternary Research, 71*(1), 9-21.

Krammer, K. (1986). Sub wasserflora von Mitteleuropa. Bacillariophyceae 1. Teil. *Gustav Fischer Verlag Stuttgart New York, 876*.

Krammer, K. (1988). Bacillariophyceae 2. Teil: Bacillariaceae, Epithemiaceae, Surirellaceae. *SuBwasserflora von Mitteleuropa*.

Krammer, K. (1991). Bacillariophyceae 4. Teil: Achnanthaceae, Kritische Erganzungen zu Navicula (Lineolatae) und Gomphonema. *Sußwasserflora von Mitteleuropa, 2*.

Krammer, K., & Lange-Bertalot, H. (1991). Bacillariophyceae Teil: Naviculaceae; Bacillariaceae, Epithemiaceae, Surirellaceae; Centrales, Fragilariaceae, Eunotiaceae; Achnathaceae. *Kritische Erganzungen zu Navicula und Gomphonema*, 1-5.

Lee, S.S., Bishop, I.W., Spaulding, S.A., Mitchell, R.M., Yuan, L.L., 2019. Taxonomic harmonization may reveal a stronger association between diatom assemblages and total phosphorus in large datasets: *Ecological Indicators*, v. 102, p. 166-174.

Leonard, L.J., Currie, C.A., Mazzotti, S., & Hyndman, R.D. (2010). Rupture area and displacement of past Cascadia great earthquakes from coastal coseismic subsidence: *GSA Bulletin*, 122(11/12), 2079-2096.

Long, A., & Shennan, I. (1994). Sea-level changes in Washington and Oregon and the" earthquake deformation cycle". *Journal of Coastal Research*, 825-838.

Ludwig, K.A. et al. (2018). Science for a risky world – A U.S. Geological Survey plan for risk research and applications: *U.S. Geological Survey Circular* 1444, 57 p.

Mazzotti, S., Dragert, H., Henton, J., Schmidt, M., Hyndman, R., James, T., Craymer, M. (2003). Current tectonics of northern Cascadia from a decade of GPS measurements. *Journal of Geophysical Research: Solid Earth, 108*(B12).

McCaffrey, R., King, R. W., Payne, S. J., & Lancaster, M. (2013). Active tectonics of northwestern US inferred from GPS-derived surface velocities. *Journal of Geophysical Research: Solid Earth, 118*(2), 709-723.

Melnick, D., Cisternas, M., Moreno, M., & Norambuean, R. (2012). Estimating coseismic coastal uplift with an intertidal mussel: calibration for the 2010 Maule Chile earthquake (M_w = 8.8): *Quaternary Science Reviews*, 42, 29-42.

Milker, Y., Nelson, A. R., Horton, B. P., Engelhart, S. E., Bradley, L.-A., & Witter, R. C. (2016). Differences in coastal subsidence in southern Oregon (USA) during at least six prehistoric megathrust earthquakes. *Quaternary Science Reviews, 142*, 143-163.

National Climatic Data Center, and Ncdc. “COOP Select State.” *IPS - Record of Climatological Observations - Select State | IPS | National Climatic Data Center (NCDC)*, NOAA, 2019, www.ncdc.noaa.gov/IPS/coop/coop.html.

Nelson, A. R., Asquith, A. C., & Grant, W. C. (2004). Great earthquakes and tsunamis of the past 2000 years at the Salmon River estuary, central Oregon coast, USA. *Bulletin of the Seismological Society of America, 94*(4), 1276-1292.

Nelson, A.R., Shennan, E., Long, A.J. (1996b). Identifying coseismic subsidence in tidal-
wetland stratigraphic sequences at the Cascadia subduction zone of western North
America. *J. Geophys. Res*. 101, 6115-6135.

Nelson, A.R., Jennings, A.E., Kashima, K. (1996a). An earthquake history derived from stratigraphic and microfossil evidence of relative sea-level change at Coos Bay, Southern coastal Oregon. *Geological Society of America Bulletin*. 108(2), 141-152.

Nelson, A. R., Atwater, B. F., Bobrowsky, P. T., Bradley, L.-A., Clague, J. J., Carver, G. A., . . . Sparks, R. (1995). Radiocarbon evidence for extensive plate-boundary rupture about 300 years ago at the Cascadia subduction zone. *Nature, 378*(6555), 371.

Nelson, A. R., & Kashima, K. (1993). Diatom zonation in southern Oregon tidal marshes relative to vascular plants, foraminifera, and sea level. *Journal of Coastal Research*, 673-697.

Nelson, A. R., Kelsey, H. M., & Witter, R. C. (2006). Great earthquakes of variable magnitude at the Cascadia subduction zone. *Quaternary Research, 65*(3), 354-365.

Nelson, A. R., Sawai, Y., Jennings, A. E., Bradley, L.-A., Gerson, L., Sherrod, B. L., Sabean, J., Horton, B. P. (2008). Great-earthquake paleogeodesy and tsunamis of the past 2000 years at Alsea Bay, central Oregon coast, USA. *Quaternary Science Reviews, 27*(7-8), 747-768.

Ozawa, S., Nishimura, T., Suito, H., Kobayashi, T., Tobita, M., & Imakiire, T. (2011). Coseismic and postseismic slip of the 2011 magnitude-9 Tohoku-Oki earthquake. *Nature* 475, 373-376.

Palmer, A. J., & Abbott, W. H. (1986). Diatoms as indicators of sea-level change. In *Sea-level Research* (pp. 457-487): Springer.

Park, J., Yuan, H., & Levin, V. (2004). Subduction zone anisotropy beneath Corvallis, Oregon: A serpentinite skid mark of trench-parallel terrane migration? *Journal of Geophysical Research: Solid Earth, 109*(B10).

Passy, S. I. (2007). Diatom ecological guilds display distinct and predictable behavior along nutrient and disturbance gradients in running waters: *Aquatic botany*, v. 86, no. 2, p. 171-178.

Plafker, G. & Savage, J.C. (1970). Mechanisms of Chilean earthquakes of May 21 and May 22, 1960. *Geological Society of America Bulletin* 81(4), 1001-1030.

Plater, A. J., Kirby, J. R., Boyle, J. F., Shaw, T., & Mills, H. (2015). Loss on ignition and organic content. *Handbook of Sea-Level Research, edited by: Shennan, I., Long, AJ, and Horton, BP*, 312-330.

Sabean, J. (2004). Application of foraminifera to detecting land level change associated with great earthquakes along the west coast of North America, *MS Thesis*, Department of Earth Sciences, Simon Fraser Universtiy, 85 p.

Satake, K., Shimazaki, K., Tsuji, Y., & Ueda, K. (1996). Time and size of a giant earthquake in Cascadia inferred from Japanese tsunami records of January 1700. *Nature, 379*(6562), 246.

Sawada, M. (2006). An open source implementation of the Modern Analog Technique (MAT) within the R computing environment. *Computers & Geosciences, 32*(6), 818-833.

Sawai, Y., Horton, B. P., & Nagumo, T. (2004b). The development of a diatom-based transfer function along the Pacific coast of eastern Hokkaido, northern Japan—an aid in paleoseismic studies of the Kuril subduction zone. *Quaternary Science Reviews, 23*(23-24), 2467-2483.

Sawai, Y., Satake, K., Kamataki, T., Nasu, H., Shishikura, M., Atwater, B. F., Yamaguchi, M. (2004a). Transient uplift after a 17th-century earthquake along the Kuril subduction zone. *Science, 306*(5703), 1918-1920.

Shennan, I., & Hamilton, S. (2006). Coseismic and pre-seismic subsidence associated with great earthquakes in Alaska. *Quaternary Science Reviews, 25*(1-2), 1-8.

Shennan, I., Long, A., Rutherford, M., Green, F., Innes, J., Lloyd, J., Walker, K. (1996). Tidal marsh stratigraphy, sea-level change and large earthquakes, I: a 5000 year record in Washington, USA. *Quaternary Science Reviews, 15*(10), 1023-1059.

Shennan, I., Innes, J.B., Long, A.J., & Zong, Y. (1995). Holocene relative sea-level changes and coastal vegetation history at Kentra Moss, Argyll, northwest Scotland. *Marine Geology*, 124, 43-59.

Shennan, I., Long, A., Rutherford, M., Innes, J., Green, F., & Walker, K. (1998). Tidal marsh stratigraphy, sea-level change and large earthquakes—II: submergence events during the last 3500 years at Netarts Bay, Oregon, USA. *Quaternary Science Reviews, 17*(4-5), 365-393.

Sherrod, B. (1999). Gradient analysis of diatom assemblages in a Puget Sound salt marsh: can such assemblages be used for quantitative paleoecological reconstructions? *Palaeogeography, Palaeoclimatology, Palaeoecology, 149*(1-4), 213-226.

Sherrod, B. L. (2001). Evidence for earthquake-induced subsidence about 1100 yr ago in coastal marshes of southern Puget Sound, Washington. *GSA Bulletin, 113*(10), 1299-1311.

Sperazza, M., Moore, J. N., & Hendrix, M. S. (2004). High-resolution particle size analysis of naturally occurring very fine-grained sediment through laser diffractometry. *Journal of Sedimentary Research, 74*(5), 736-743.

Thatcher, W. (1984). The earthquake deformation cycle, recurrence, and the time-predictable model. *Journal of Geophysical Research: Solid Earth, 89*(B7), 5674-5680.

Troels-Smith, J. (1955). Karakterisering af lose jordarter. Characterization of unconsolidated sediments.

Ulm, S. (2002). Marine and estuarine reservoir effects in central Queensland, Australia: determination of ΔR values. *Geoarchaeology: An International Journal, 17*(4), 319-348.

Wang, K., & Tréhu, A. M. (2016). Invited review paper: Some outstanding issues in the study of great megathrust earthquakes—The Cascadia example. *Journal of Geodynamics, 98*, 1-18.

Wang, K., Wells, R., Mazzotti, S., Hyndman, R. D., & Sagiya, T. (2003). A revised dislocation model of interseismic deformation of the Cascadia subduction zone. *Journal of Geophysical Research: Solid Earth, 108*(B1).

Wang, P. L., Engelhart, S. E., Wang, K., Hawkes, A. D., Horton, B. P., Nelson, A. R., & Witter, R. C. (2013). Heterogeneous rupture in the great Cascadia earthquake of 1700 inferred from coastal subsidence estimates. *Journal of Geophysical Research: Solid Earth, 118*(5), 2460-2473.

Watcham, E. P., Shennan, I., & Barlow, N. L. (2013). Scale considerations in using diatoms as indicators of sea-level change: lessons from Alaska. *Journal of Quaternary Science, 28*(2), 165-179.

Weckström, K., & Juggins, S. (2006). COASTAL DIATOM–ENVIRONMENT RELATIONSHIPS FROM THE GULF OF FINLAND, BALTIC SEA 1. *Journal of Phycology, 42*(1), 21-35.

Weilhoefer, C. L., & Pan, Y. (2006). Diatom-based bioassessment in wetlands: How many samples do we need to characterize the diatom assemblage in a wetland adequately? *Wetlands, 26*(3), 793-802.

Witkowski, A. (2000). Diatom flora of marine coasts I. *Iconographia diatomologica*.

Witter, R. C., Kelsey, H. M., & Hemphill-Haley, E. (2003). Great Cascadia earthquakes and tsunamis of the past 6700 years, Coquille River estuary, southern coastal Oregon. *Geological Society of America Bulletin, 115*(10), 1289-1306.

Woodroffe, S.A., and Long, A.J. (2010). Reconstructing recent relative sea-level changes in West Greenland: Local diatom-based transfer functions are superior to regional models: *Quaternary International*, v. 221, no. 1-2, 91-103.

Yang, S.L., Li., H., Ysebaert, T., Bouma, T.J., Zhang, W.X., Wang, Y.Y., Li, P., Li, M., & Ding, P.X. (2008). Spatial and temporal variations in sediment grain size in tidal wetlands, Yangtze Delta: On the role of physical biotic controls. *Estuarine Coastal and Shelf Science*,77, 657-671.

Yousefi, M., Milne, G. A., Love, R., & Tarasov, L. (2018). Glacial isostatic adjustment along the Pacific coast of central North America. *Quaternary Science Reviews, 193*, 288-311.

Zong, Y., & Horton, B. P. (1998). Diatom zones across intertidal flats and coastal saltmarshes in Britain. *Diatom Research, 13*(2), 375-394.

Zong, Y., & Horton, B. P. (1999). Diatom-based tidal-level transfer functions as an aid in reconstructing Quaternary history of sea-level movements in the UK. *Journal of Quaternary Science, 14*(2), 153-167.

Zong, Y., Shennan, I., Combellick, R., Hamilton, S., & Rutherford, M. (2003). Microfossil evidence for land movements associated with the AD 1964 Alaska earthquake. *The Holocene, 13*(1), 7-20.

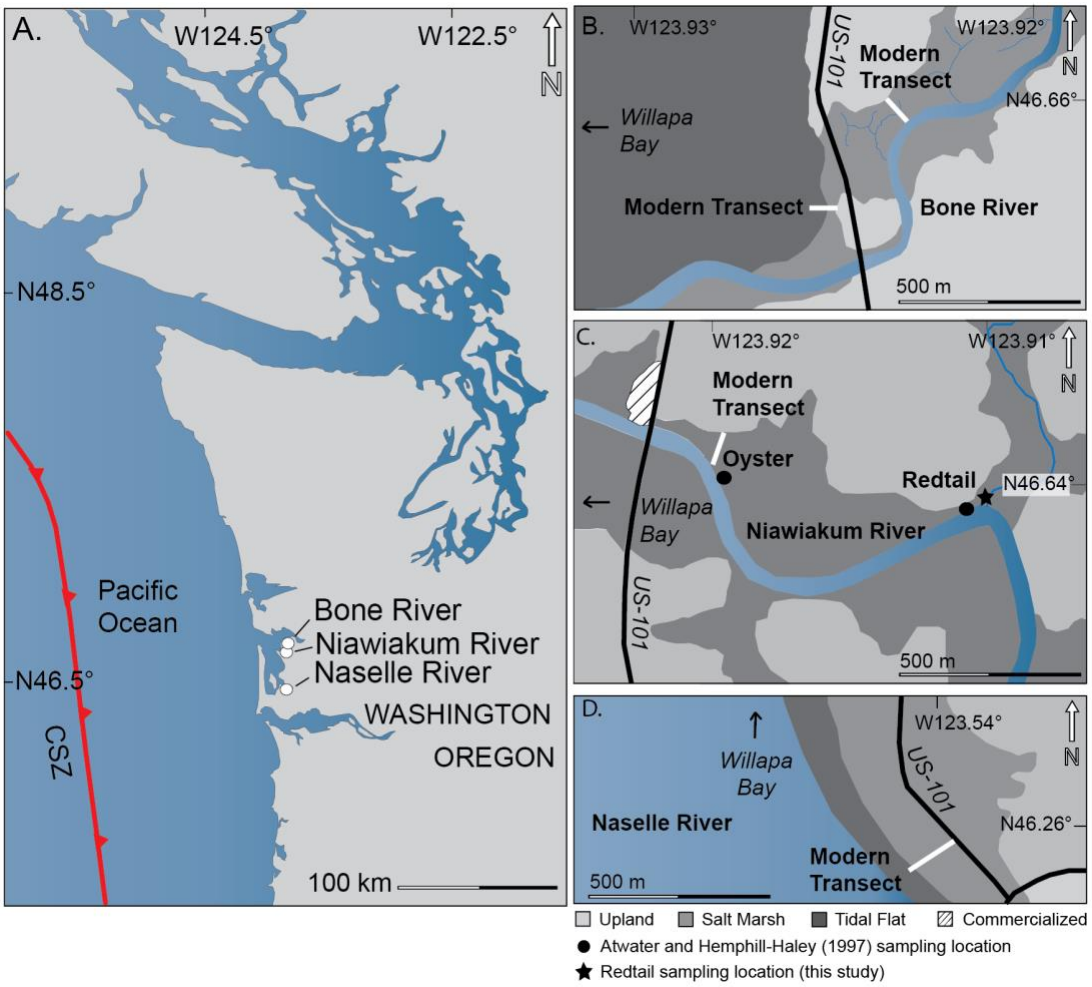

Figure 1: (A) Map of the Cascadia subduction zone and the coast of Washington. The circles indicate study areas from which samples were collected. (B) Map of the Bone River and location of sampled modern training set transects (white lines). (C) Map of the Niawiakum River and Redtail locality. Sampled modern transect is indicated with white line. (D) Map of the Naselle River and location of sampled modern training set transect (white line).

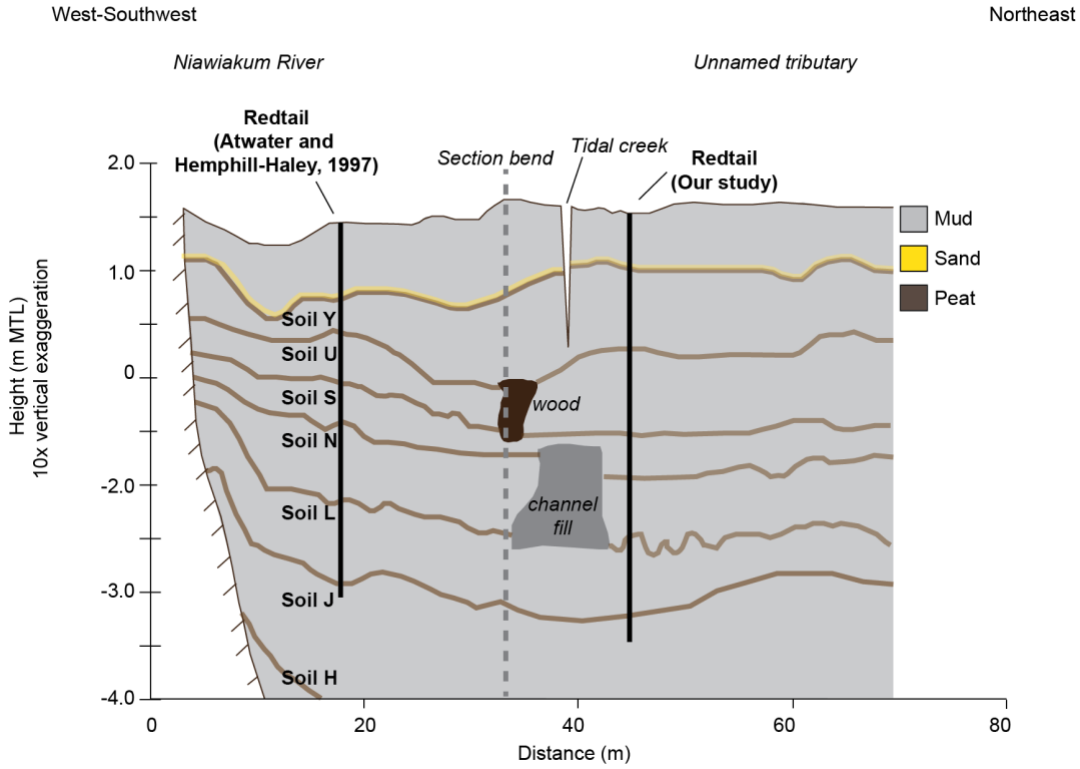

Figure 2: Stratigraphy at Redtail locality (Modified from Atwater and Hemphill-Haley, 1997) showing sampling location of Redtail core of Atwater and Hemphill-Haley (1997) and our study.

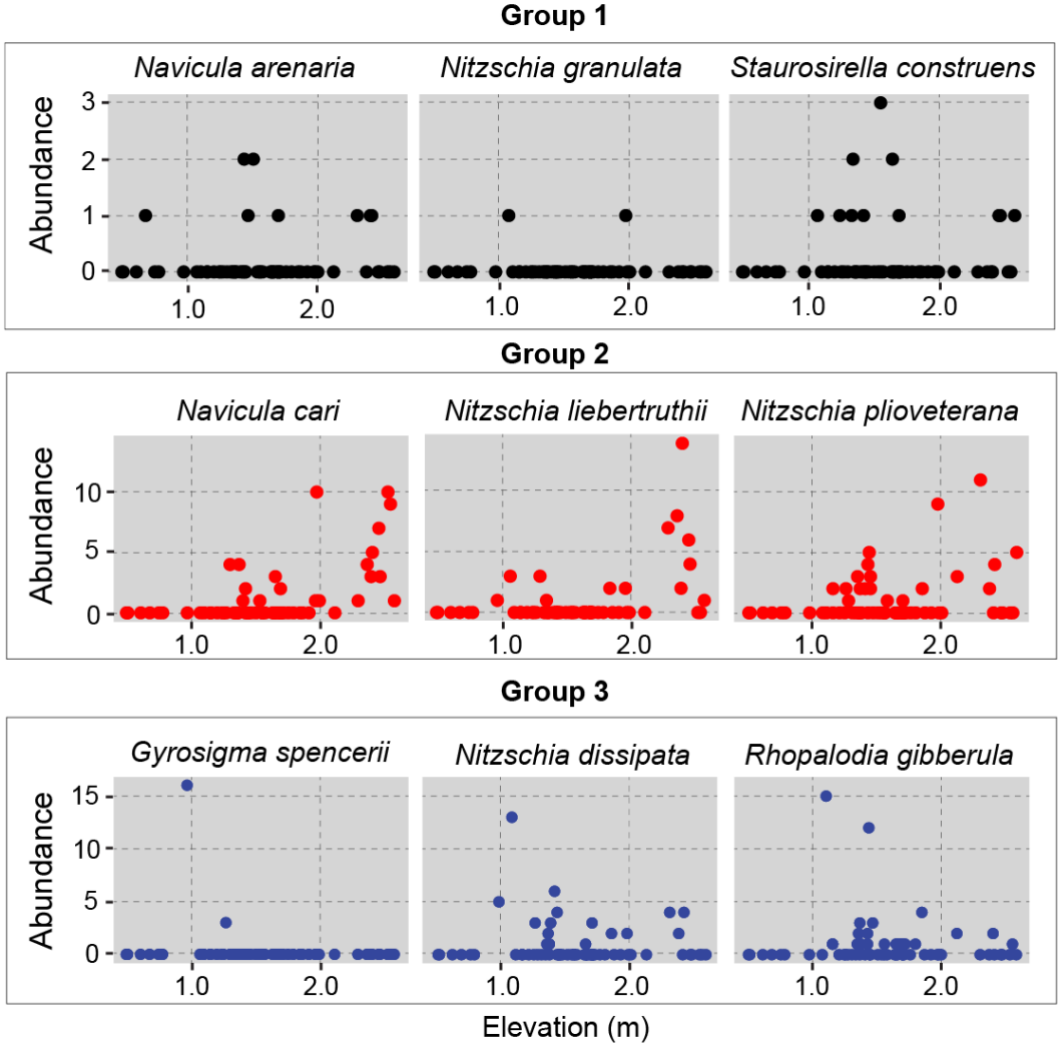

Figure 3: Example of species that have been grouped together (colors indicate groupings) based on exhibiting a similar abundance and distribution with respect to elevation.

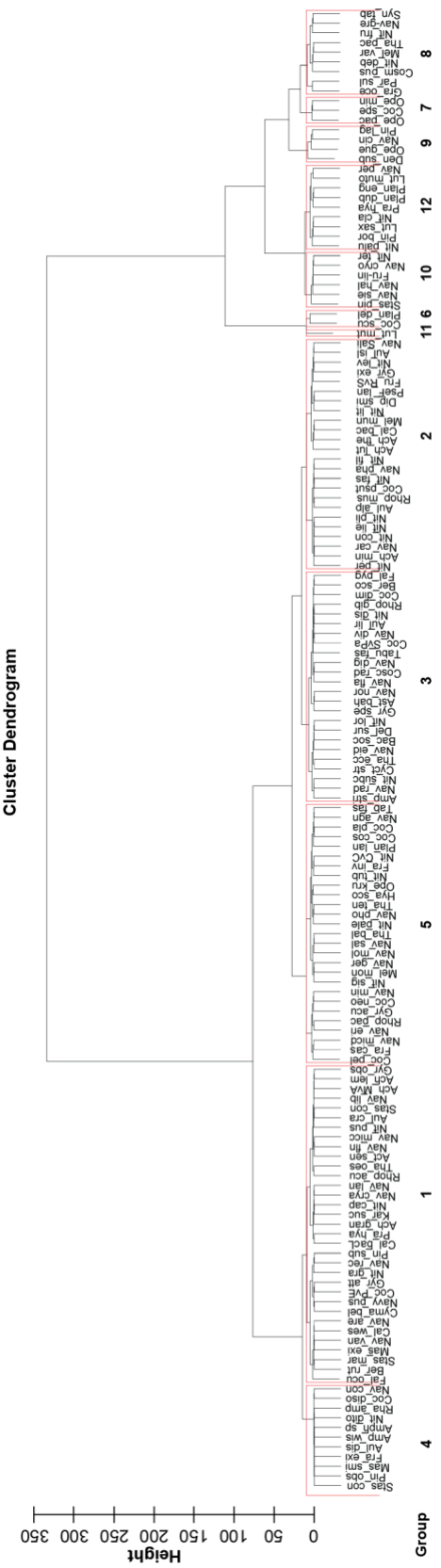

Figure 4: Hierarchical clustering results showing the species groupings (red line).

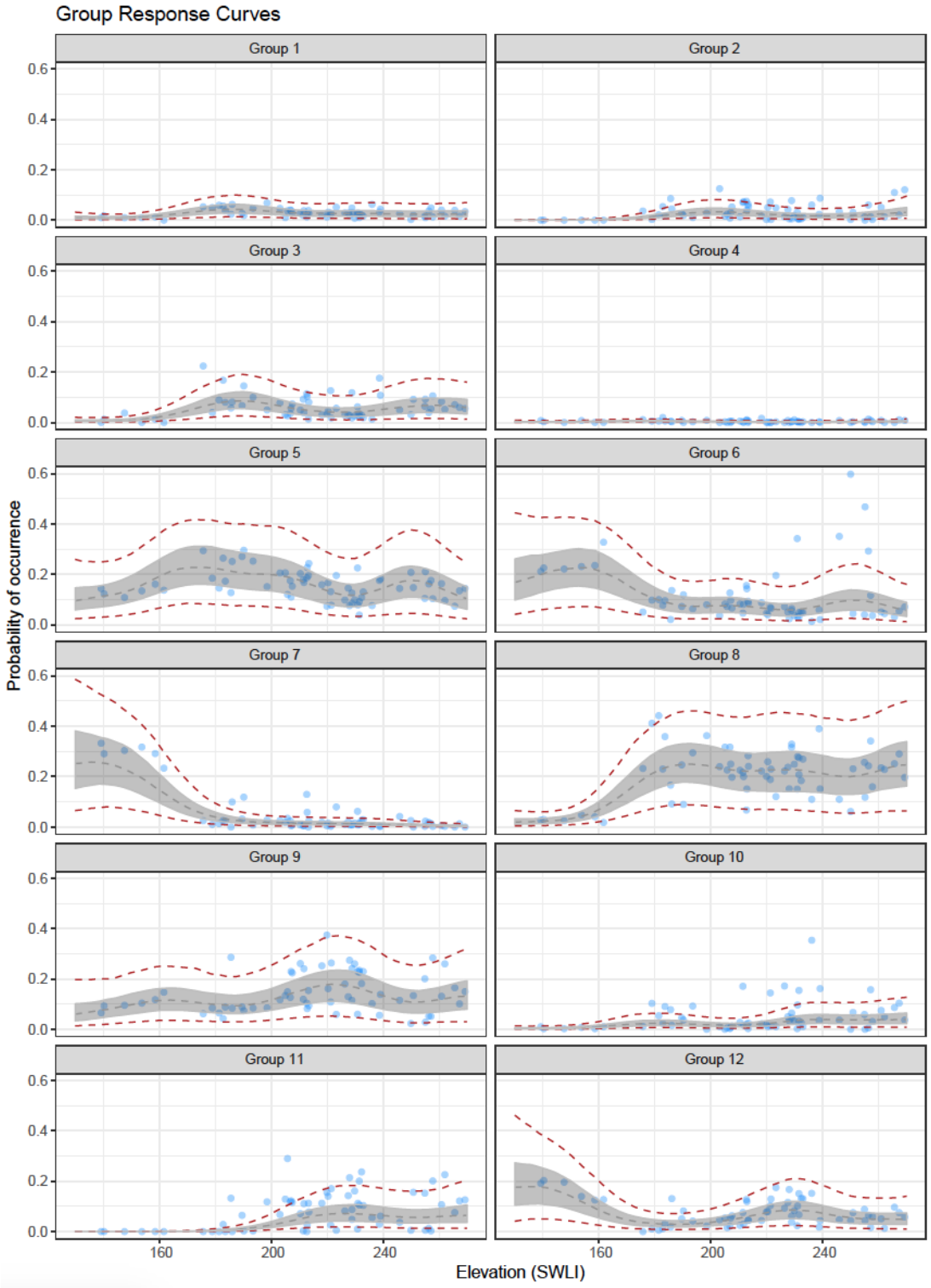

Fig 5: Species optima curves (filed gray curve) of grouped diatoms to elevations estimated from the modern training set of counts using the Bayesian diatom transfer function. The blue circles represent the probabilities of species occurrence based on the count data. The dashed lines represent predicted probabilities with 95% credible intervals.

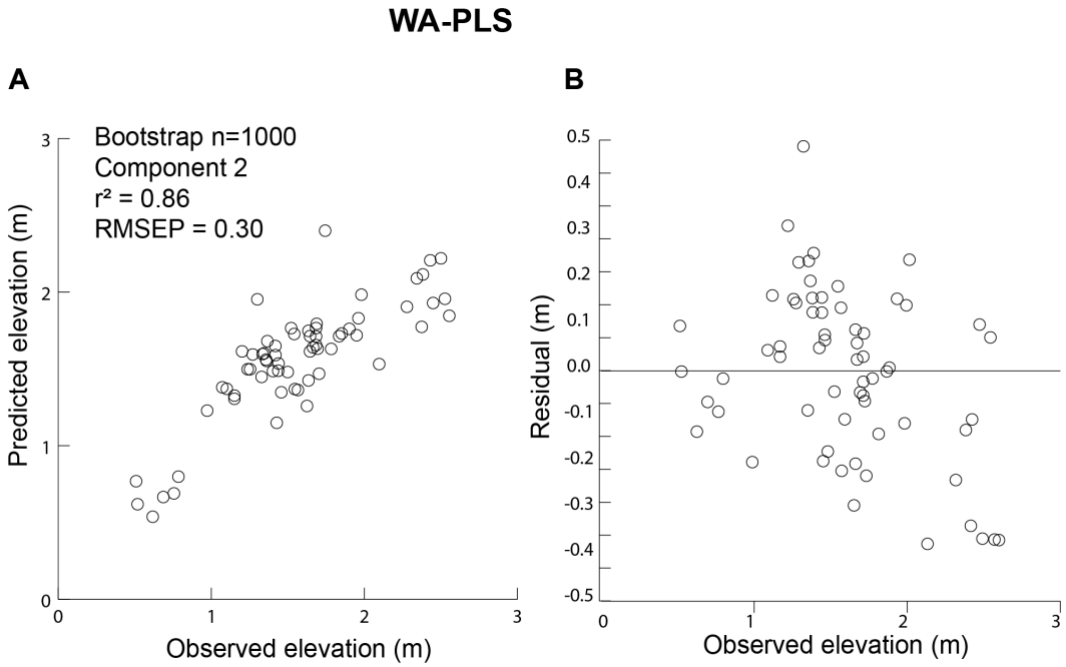

Figure 6: (A) Plot of the WA-PLS predicted versus observed elevation (m MTL) for modern diatom samples in the training set. (B) Plot of WA-PLS residual elevation versus observed elevation for the same surface diatom samples.

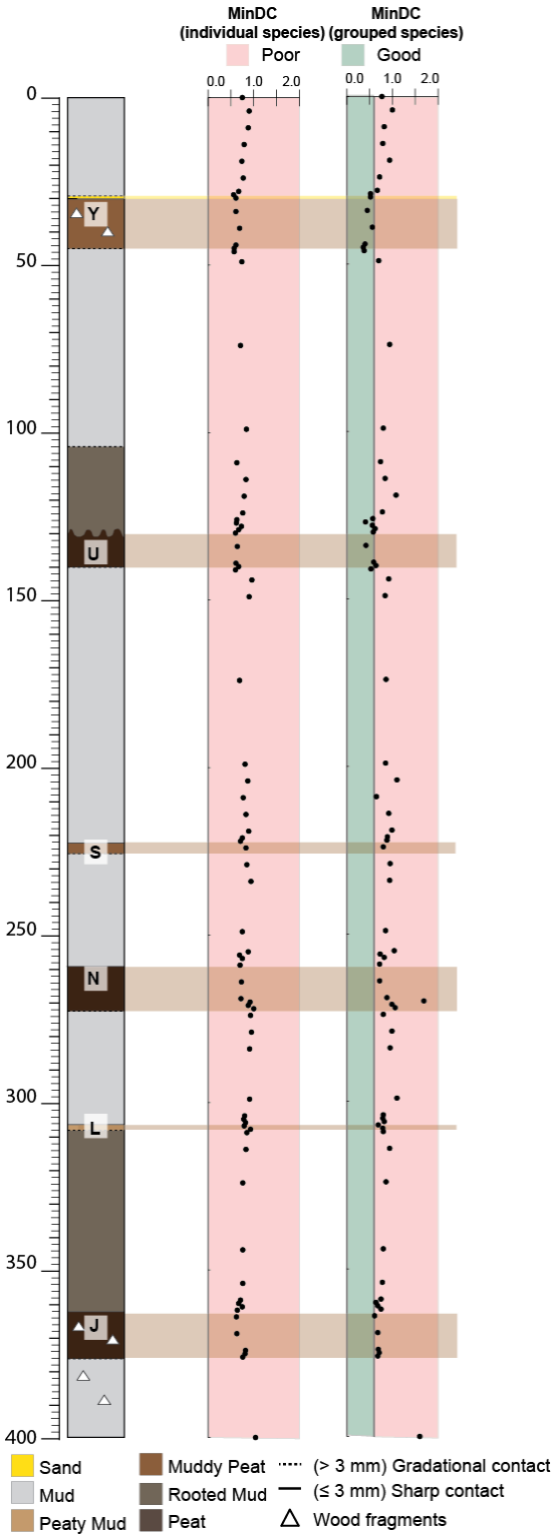

Figure 7: (Right) Stratigraphic section with MAT results indicating a poor (red) or good (green) analogue for individual species and grouped species.

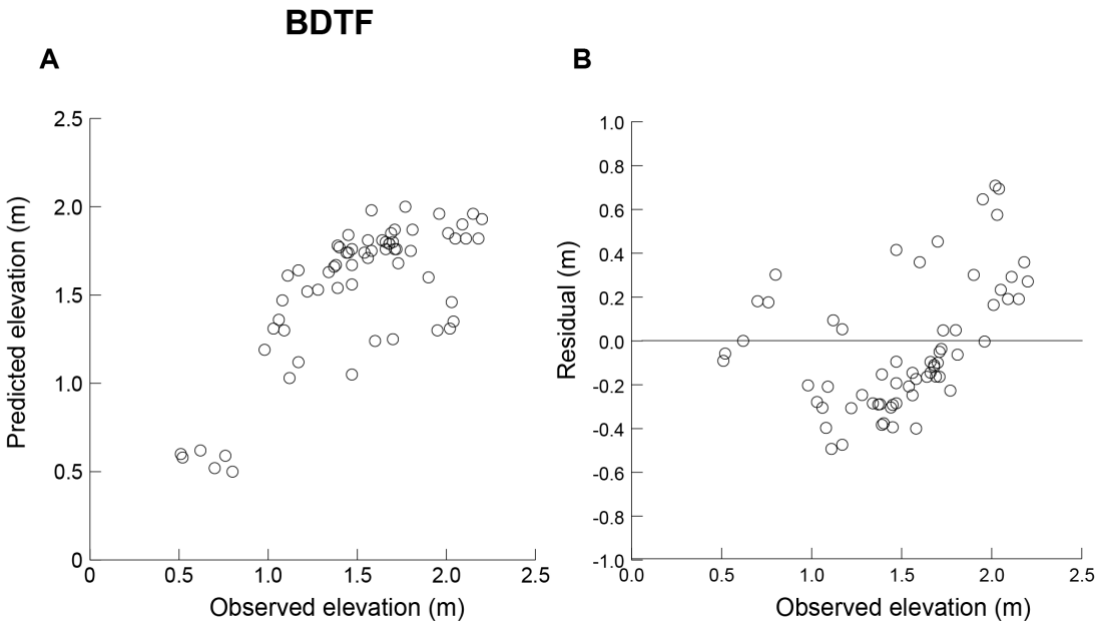

Figure 8: (A) Plot of the BDTF predicted versus observed elevation (m MTL) for modern diatom samples in the training set. (B) Plot of BDTF residual elevation versus observed elevation for the same surface diatom samples.

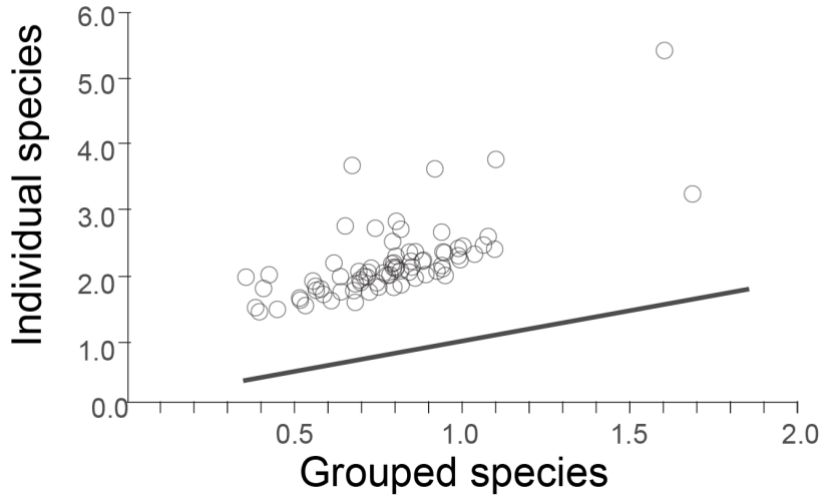

Figure 9: Plot of each minimum distance found by grouping species versus the minimum distance found using all species with 1:1 line (dark gray). All minimum distances from all species produced are larger than the minimum distance using grouped species.

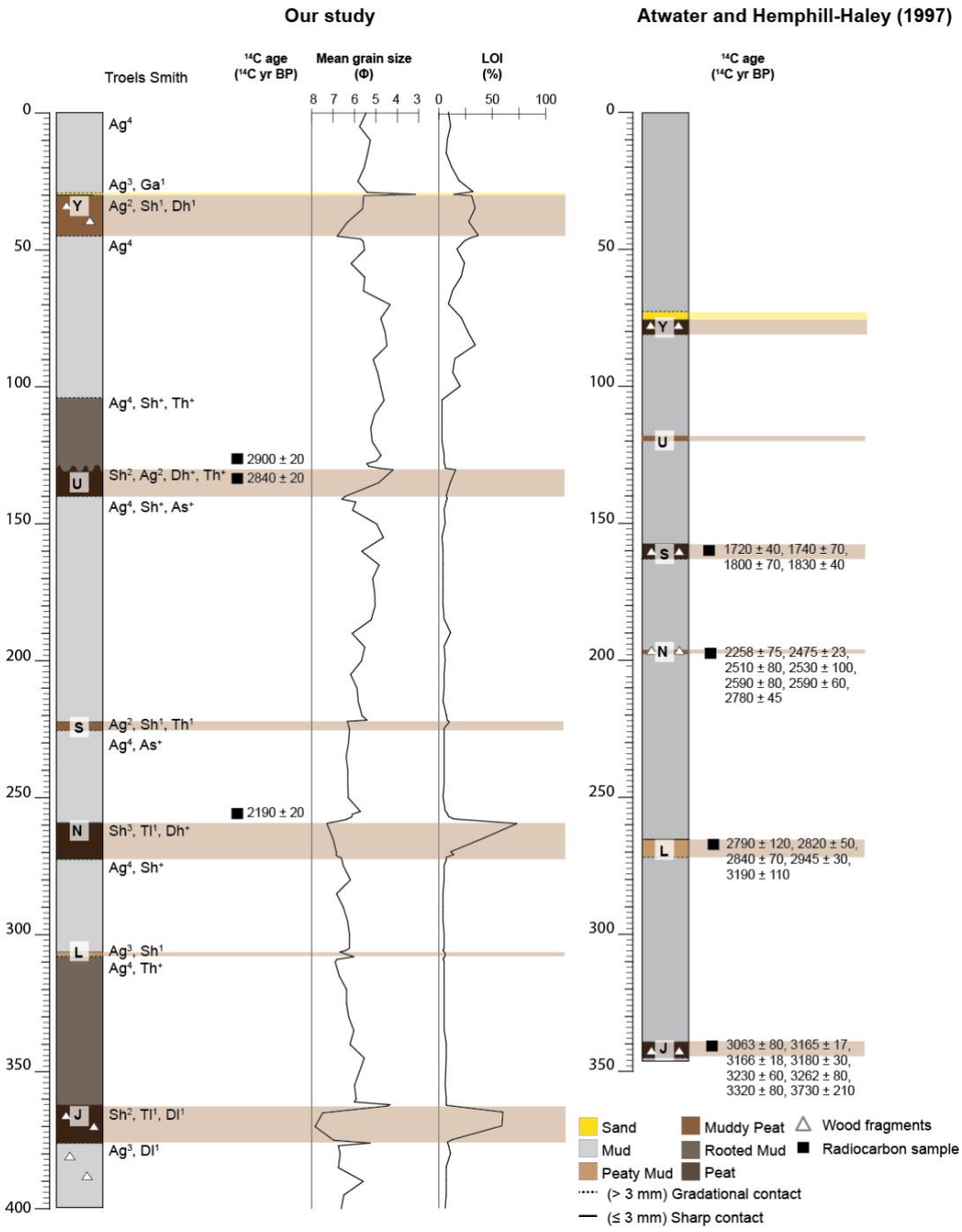

Figure 10: (Right) Stratigraphic section with radiocarbon age, grain size, and LOI data. (Left) Stratigraphic section of Atwater and Hemphill-Haley (1997) with radiocarbon ages.

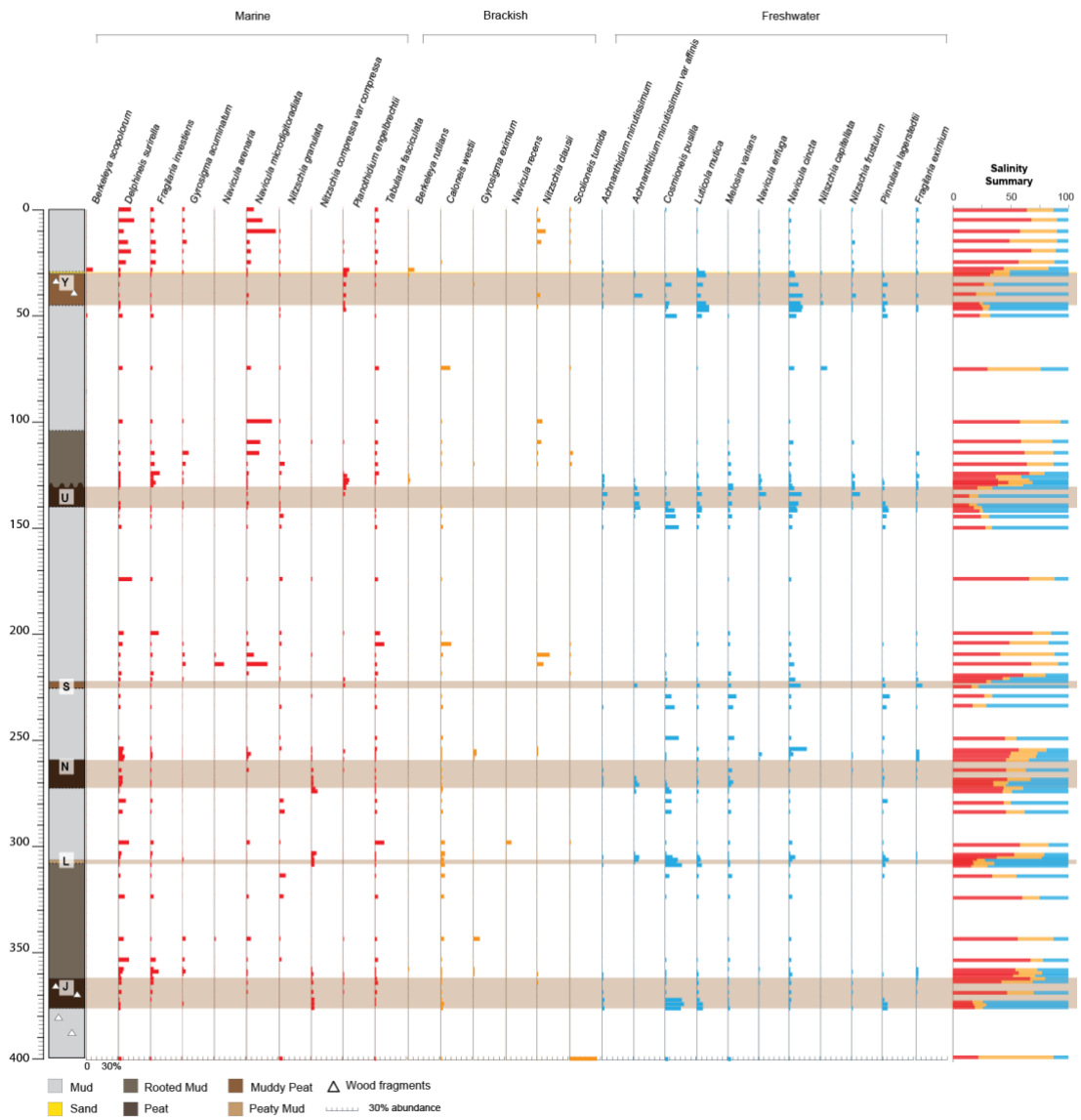

Figure 11: Stratigraphic section with changes in dominant diatom species (> 5% abundance in at least one sample) down core. Species *Paralia sulcata* and *Cocconeis scutellum* are excluded from this figure due to their notable abundance throughout the core.

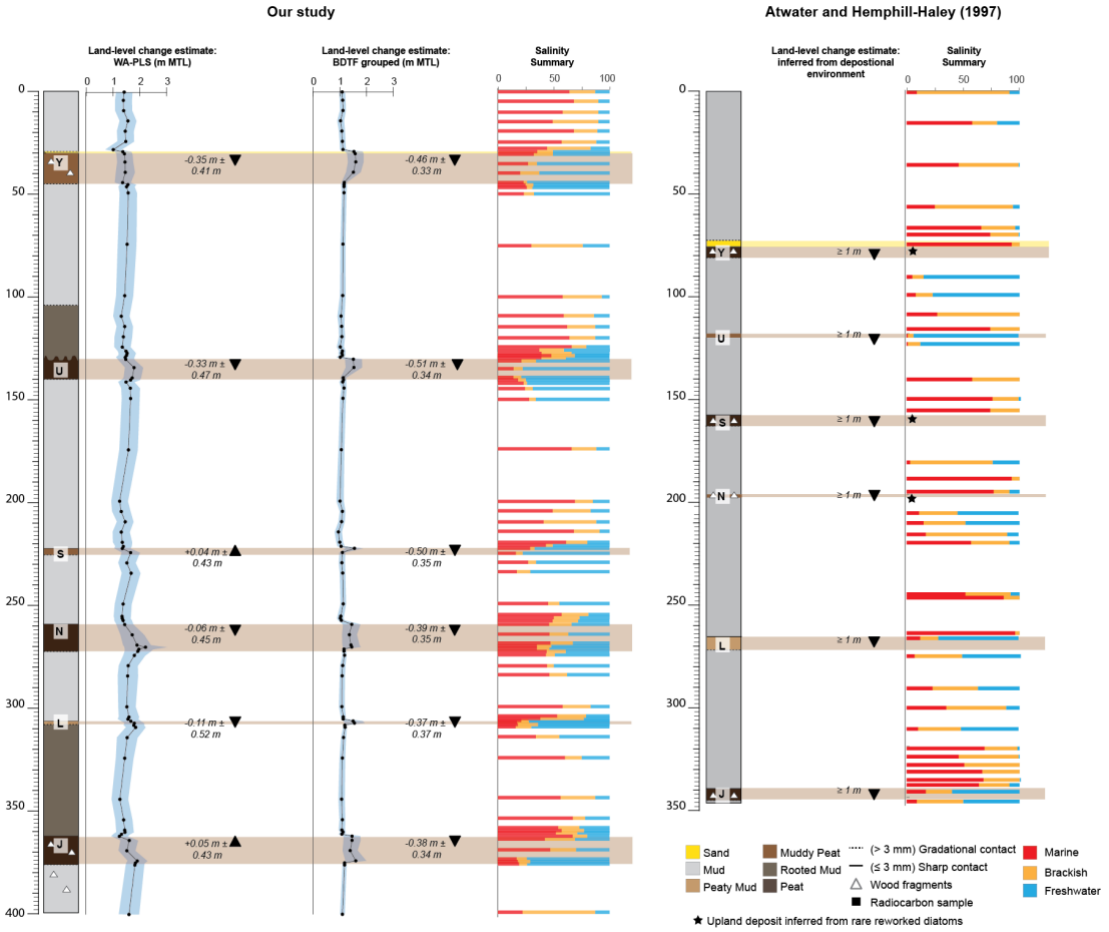

Figure 12: (Right) Stratigraphic section with reconstructed elevation using the WA-PLS transfer function (with 1 σ error) and BDTF transfer function (with 1 σ error). A salinity summary showing the relative proportion of marine, brackish, and freshwater diatoms. (Left) Stratigraphic section of Atwater and Hemphill-Haley (1997) with radiocarbon ages. Estimated land-level change is based on inferred changes in depositional environment from an upland/high marsh to tidal flat. A salinity summary showing the relative proportion of marine, brackish, and freshwater diatoms.

Conclusions

Collectively, these chapters highlight and address challenges with understanding the long-term variability in tropical cyclone intensity and earthquake magnitude. This dissertation explored the development and application of modern analogues as tools to provide more accurate and precise reconstructions of tropical cyclone intensity and earthquake magnitude.

In Chapter 1, Tropical Cyclone (TC) Pam provided a modern analogue to characterize sediments deposited by a land-falling Category 5 tropical cyclone for the first time in the South Pacific. The overwash pumice layers from TC Pam extended farther than the overwash sand at both Manuro and Port Resolution Bay, suggesting they are a closer approximation of inundation distance by a storm surge. The combination of its composition and durability would make pumice uniquely suited for identifying and interpreting paleostorms in the geologic record. The grain-size distributions of the overwash sand at both Manuro and Port Resolution Bay, however, did not differentiate the TC Pam sand from the underlying unit. Rather, sedimentary structures such as coarsening and fining upward sequences and laminations distinguished the TC Pam sediments from the homogeneous underlying layers.

Preservation of tropical cyclone overwash sediments for reconstructing paleo-storm records are dependent on the availability of accommodation space that allows for the aggradation and preservation of sediment in the geologic record (e.g., Liu and Fearn, 1993; Donnelly and Woodruff, 2007; Pilarczyk, et al., 2016). In coastal environments, relative sea-level (RSL) rise creates accommodation space for overwash sediments to accumulate (e.g., Kelsey et al., 2015, Dura et al., 2016). RSL reconstructions from the southeast coast of Australia document a mid-Holocene high stand of 1.5 m higher than

present sea-level (Sloss et al., 2007), which would result in reduced accommodation space for sediment preservation. In Efate and Tanna islands, accommodation space is further limited by coeval RSL fall due gradual uplift from tectonic processes (Collot et al., 1985). Long-term preservation of Tropical Cyclone Pam overwash sediments will likely be site dependent and will favor locations like Port Resolution Bay, where a depression seaward of coastal Lake Eweya provides the necessary accommodation space.

The results of this study provides a vital modern analogue that may help distinguish overwash sediments deposited by paleo-storms or paleo-tsunamis in Vanuatu. Multiple, thin laminations in the TC Pam deposit at Port Resolution Bay are more indicative of storm or flood deposits (e.g., Kortekaas and Dawson, 2007; Switzer and Jones, 2008). However, many other sedimentary features in the TC Pam deposit (e.g., coarsening or fining upward, landward thinning, and sharp, erosive basal contacts) are similar to those of paleo-tsunami deposits (e.g., Morton et al., 2007; Monecke et al., 2008; Hong et al., 2017). For this reason, care must be taken to ensure that overwash deposits in the geologic record satisfy multiple criteria (e.g., sedimentologic features, paleontologic changes, etc.) for tropical cyclone deposition (Shanmugam, 2012).

Of tropical cyclones with known intensity, we validate the application of an inverse sediment transport model in determining maximum flow depth of high-intensity tropical cyclones in tropical environments. This study was the first to do so based solely on empirically derived settling velocities for volcanic sediment. The inverse settling transport (W08) model was applied at Port Resolution Bay using the measured settling velocities of the coarsest sediment. By applying the W08 model to our site at Port Resolution Bay, we were able to reconstruct the calculated flow depth value of 1.51 m

within ~11%. Future paleotempestology studies can apply the inverse sediment transport model to determine pre-historic tropical cyclone intensity.

Chapter 2 characterized the modern distribution of diatom zones and their environmental variables (elevation, grain-size, total organic carbon, porewater salinity, and nutrient concentrations) across intertidal environments in Willapa Bay, WA and considered its application in sea-level reconstructions. This study was the first of its kind in Washington state to measure the sampling elevation of diatoms in relation to the tidal range at more than one site. Hierarchical clustering and ordination of individual and combined (regional) transects identified varying floral zones with driven by different environmental variables. Vertical zonation of diatom assemblages at two sites showed a distinct separation of the tidal flat, low marsh, and high marsh environments driven by elevation whereas a third site displayed a relatively high abundance of marine, brackish, and freshwater species across the intertidal with zonation driven by salinity. The regional training set identified four floral zones with salinity as the major environmental control.

Results show that no one environmental variable consistently defines diatom assemblage distribution in intertidal zones because diatoms exhibit a complex relationship with environmental variables. In spite of overlapping tidal environments and elevation, site-specific variability among dominant diatom assemblages exist. Differences in dominant species between transects and the widespread distribution of species across more than one intertidal zone suggest diatom preference for particular environments are indiscrete and oftentimes transitional across a large range of the intertidal zone (e.g., McIntire, 1978). Differences in dominant species between transects and the widespread distribution of species across more than one intertidal zone

suggest the application of diatoms in RSL reconstructions may be limited due to the high spatial variability of assemblage distribution in intertidal environments that can lead to a no matching analogue problem with fossil diatoms.

In the Pacific Northwest of North America, diatoms have been applied to estimate RSL rise from earthquakes because they are abundant in fresh, brackish, and marine environments (e.g., Shennan et al., 1996; Atwater and Hemphill-Haley, 1997). Using an empirically derived relationship between diatoms and tidal inundation, diatom-based transfer functions can be used to provide quantitative estimates of RSL rise from earthquakes with sample-specific errors (e.g., Sawai et al., 2004; Hamilton and Shennan, 2005) that reflect a more rapid response time than other microfossil-based proxies, such as foraminifera (Horton et al., 2017). However, the high spatial variability exhibited by the modern diatom assemblages in Willapa Bay suggest that in the absence of a large training set that covers a broad range of environments across intertidal zones, alternative methods must be sought to address the no matching analogue problem.

Finally, Chapter 3 assessed the limitations of developing and applying a diatom-based transfer function at the Cascadia subduction zone of the Pacific Northwest where a no matching analogue problem has previously resulted in unreliable estimates of coseismic subsidence from great earthquakes (Nelson et al., 2008). Without instrumental or historical observations of Cascadia subduction zone earthquakes, microfossils (e.g., diatoms) preserved within intertidal stratigraphic sequences are the only means to reconstruct site-specific coastal subsidence estimates (e.g., Wang et al., 2013). Although diatom-based transfer functions have been shown to successfully reconstruct relative sea-level from megathrust earthquakes (e.g., Hamilton and Shennan 2005;

Sawai et al., 2004), the lack of modern analogues in Cascadia limits the applicability of traditional transfer function methods.

The application of an established transfer function (weighted-averaging partial least squares) to a stratigraphic sequence of six, mud-over-peat contacts inferred to record coseismic subsidence found that all fossil samples had poor modern analogues. To address the no matching analogue problem, a novel method was developed to group species based on similarities in abundance and distribution across elevation. The grouped species resulted in an improvement of matching analogues by 21%. A Bayesian diatom transfer function (BDTF) was developed to integrate the grouped species and prior information (lithology) to improve the precision of reconstructed coseismic subsidence. The BDTF was applied to the same fossil samples from the six, mud-over peat contacts.

All but one of the good analogues were found in the upper 1.5 m of the sediment core, which spans the two uppermost mud-over-peat contacts. The results suggest the BDTF produced reliable estimates of subsidence from the 1700 CE earthquake (0.46 m ± 0.33 m) and the mud-over-peat contact of Soil U (0.51 m ± 0.34 m). In contrast, fossil samples from Soil S, N, L, and J and the overlying mud/rooted mud resulted in a poor analogue match with the mud/rooted mud units displaying a greater dissimilarity than the wetland soils. The greater number of poor analogues below 1.5 m in the sediment core suggests the modern intertidal environment from the training set does not capture the range of paleoenvironmental conditions that existed in Willapa Bay from ~1400 to 3500 yrs CE.

Future work will include the collection of additional modern samples that will address the lack of modern analogues from older events. Dominant fossil diatoms in the poor

analogue samples below 1.50 m depth are marine (e.g., *Berkeleya scopolorum, Mastogloia smithii*, and *Nitzschia granulata*) and brackish (e.g., *Caloneis westii*, *Gyrosigma eximium*, and *Scolioneis tumida*) species. These species have been observed in the low marsh and tidal flat environments of Willapa Bay (Hemphill-Haley, 1995a), but were not captured in the modern training set (Chapter 2). Modern samples targeting lower elevations in the tidal flat and subtidal environments will allow the BDTF to predict lower elevations than it is currently able to do so (0.50 m MTL). Furthermore, the application of the BDTF to a simulated marsh subsidence experiment will assess the accuracy of the transfer function in reconstructing subsidence.

This dissertation illustrates the challenges and breakthroughs in developing a quantitative method for estimating the intensity and magnitude of pre-historic tropical cyclones and earthquakes. Using modern day observations, proxies can be developed to better understand coastal hazards related to relative sea-level rise. Additional modern analogues are needed to validate and improve upon these quantitative proxies so that more accurate and precise estimates of prehistoric tropical cyclone intensity and earthquake magnitude are possible.

References

Atwater, B. F., and Hemphill-Haley, E., 1997, Recurrence intervals for great earthquakes of the past 3,500 years at northeastern Willapa Bay, Washington: USGPO; Information Services [distributor], 2330-7102.

Collot, J.Y., Daniel, J., Burne, R.V., 1985. Recent tectonics associated with the subduction/collision of the d'Entrecasteaux zone in the Central New Hebrides. Tectonophysics, 112, 325-356.

Donnelly, J.P., Woodruff, J.D., 2007. Intense hurricane activity over the past 5,000 years controlled by El Niño and the West African monsoon. Nature 447, 465–468.

Dura, T., Engelhart, S.E., Vacchi, M., Horton, B.P., Kopp, R.E., Peltier, W.R., Bradley, S., 2016. The role of Holocene relative sea-level change in preserving records of subduction zone earthquakes. Curr. Clim. Chang. Rep. 2 (3), 86-100.

Hamilton, S., and Shennan, I., 2005. Late Holocene relative sea-level changes and the earthquake deformation cycle around upper Cook Inlet, Alaska. Quaternary Science Reviews, 24(12-13), 1479-1498.

Hong, I., Dura, T., Ely, L.L., Horton, B.P., Nelson, A.R., Cisternas, M., Nikitina, D., Wesson, R.L., 2017. 27, 39-51.

Horton, B. P., Milker, Y., Dura, T., Wang, K., Bridgeland, W. T., Brophy, L. S., Ewald, M., Khan, N., Engelhart, S. E., Nelson, A. R., and Witter, R. C., 2017, Microfossil measures of rapid sea-level rise: Timing of response of two microfossil groups to a sudden tidal-flooding experiment in Cascadia: Geology, v. 45, no. 6, p. 535-538.

Kelsey, H.M., Engelhart, S.E., Pilarczyk, J.E., Horton, B.P., Rubin, C.M., Daryono, m.R>, Ismail, N., Hawkes, A.D., Bernhardt, C.E., Cahill, N., 2015. Accommodation space, relative sea level, and the archiving of paleo-earthquakes along subduction zones. Geology 43 (8), 675-678.

Kortekaas, S., Dawson, A.G., 2007. Distinguishing tsunami and storm deposits: an example from Martinhal, SW Portugal. Sedimentary Geology 200, 208–221.

Liu, K., Fearn, M.L., 1993. Lake-sediment record of late Holocene hurricane activities from coastal Alabama. Geology 21, 793–796.

McIntire, C. D., 1978. The distribution of estuarine diatoms along environmental gradients: a canonical correlation: Estuarine and Coastal Marine Science, v. 6, no. 5, p. 447-457.

Monecke, K., Finger, W., Klarer, D., Kongko, W., McAdoo, B.G., Moore, A.L., Sudrajat, S.U., 2008. Nature, 455, 1232-1234.

Morton, R.A., Gelfenbaum, G., Jaffe, B.E., 2007. Physical criteria for distinguishing sandy tsunami and storm deposits using modern examples. Sedimentary Geology, 200, 184-207.

Nelson, A. R., Sawai, Y., Jennings, A. E., Bradley, L.-A., Gerson, L., Sherrod, B. L., Sabean, J., Horton, B. P. (2008). Great-earthquake paleogeodesy and tsunamis of the past 2000 years at Alsea Bay, central Oregon coast, USA. Quaternary Science Reviews, 27(7-8), 747-768.

Pilarczyk, J.E., Horton, B.P., Soria, J.L.A., Switzer, A.D., Siringan, F., Fritz, H.M., Khan, N.S., Ildefonso, S., Doctor, A.A., Garcia, M.L., 2016. Micropaleontology of the 2013 Typhoon Haiyan overwash sediments from the Leyte Gulf, Philippines. Sedimentary Geology 339, 104-114.

Sloss, C.R., Murray-Wallace, C.V., Jones, B.G., 2007. Holocene sea-level change on the southeast coast of Australia: a review. The Holocene 17, 999-1014.

Sawai, Y., Horton, B. P., & Nagumo, T., 2004. The development of a diatom-based transfer function along the Pacific coast of eastern Hokkaido, northern Japan—an aid in paleoseismic studies of the Kuril subduction zone. Quaternary Science Reviews, 23(23-24), 2467-2483.

Shanmugam, G., 2012. Process-sedimentological challenges in distinguishing paleo-tsunami deposits. Nat. Hazards 63, 5-30.

Shennan, I., Long, A. J., Rutherford, M. M., Green, F. M., Innes, J. B., Lloyd, J. M., Zong, Y., and Walker, K. J., 1996, Tidal marsh stratigraphy, sea-level change and large earthquakes: a 5000 year record in washington, U.S.A: Quaternary Science Reviews, v. 15, no. 10, p. 1023-1059.

Sherrod, B., 1999, Gradient analysis of diatom assemblages in a Puget Sound salt marsh: can such assemblages be used for quantitative paleoecological reconstructions?: Palaeogeography, Palaeoclimatology, Palaeoecology, v. 149, no. 1-4, p. 213-226.

Switzer, A.D., Jones, B.G., 2008. Large-scale washover sedimentation in a freshwater lagoon from the southeast Australian coast: sea-level change, tsunami or exceptionally large storm? The Holocene 18, 787–803.

Wang, P.L., Engelhart, S.E., Wang, K., Hawkes, A.D., Horton, B.P., Nelson, A.R., Witter, R.C., 2013. Heterogeneous rupture in the great Cascadia earthquake of 1700 inferred from coastal subsidence estimates. Journal of Geophysical Research 118, 2460-2473.